Mayer, L., Pisias, N., Janecek, T., et al., 1992
Proceedings of the Ocean Drilling Program, Initial Reports, Vol. 138

11. SITE 846[1]

Shipboard Scientific Party[2]

HOLE 846A

Date occupied: 21 May 1991

Date departed: 21 May 1991

Time on hole: 7 hr, 12 min

Position: 3° 5.696′S, 90° 49.078′W

Bottom felt (rig floor; m, drill-pipe measurement): 3307.3

Distance between rig floor and sea level (m): 11.70

Water depth (drill-pipe measurement from sea level, m): 3295.6

Total depth (rig floor; m): 3314.5

Penetration (m): 7.2

Number of cores (including cores with no recovery): 1

Total length of cored section (m): 7.2

Total core recovered (m): 7.2

Core recovery (%): 100.3

Oldest sediment cored:

Depth (mbsf): 7.2
Nature: nannofossil foraminifer diatom ooze
Earliest age: Pleistocene

HOLE 846B

Date occupied: 21 May 1991

Date departed: 24 May 1991

Time on hole: 2 days, 13 hr, 8 min

Position: 3° 5.696′S, 90° 49.078′W

Bottom felt (rig floor; m, drill-pipe measurement): 3307.5

Distance between rig floor and sea level (m): 11.7

Water depth (drill-pipe measurement from sea level, m): 3295.8

Total depth (rig floor; m): 3729.9

Penetration (m): 422.4

Number of cores (including cores with no recovery): 45

Total length of cored section (m): 422.4

Total core recovered (m): 373.4

Core recovery (%): 88.4

Oldest sediment cored:

Depth (mbsf): 420.0
Nature: metalliferous sediment
Earliest age: early Miocene

Basement:

Depth (mbsf): 422.4
Nature: basalt

[1] Mayer, L., Pisias, N., Janecek, T., et al., 1992. *Proc. ODP, Init. Repts.,* 138: College Station, TX (Ocean Drilling Program).

[2] Shipboard Scientific Party is as given in the list of participants preceding the contents.

HOLE 846C

Date occupied: 24 May 1991

Date departed: 25 May 1991

Time on hole: 20 hr, 19 min

Position: 3° 5.796′S, 90° 49.086′W

Bottom felt (rig floor; m, drill-pipe measurement): 3307.5

Distance between rig floor and sea level (m): 11.7

Water depth (drill-pipe measurement from sea level, m): 3295.8

Total depth (rig floor; m): 3500.0

Penetration (m): 192.5

Number of cores (including cores with no recovery): 20

Total length of cored section (m): 190.0

Total core recovered (m): 193.1

Core recovery (%): 101.6

Oldest sediment cored:

Depth (mbsf): 192.5
Nature: radiolarian diatom nannofossil ooze
Earliest age: late Miocene

HOLE 846D

Date occupied: 25 May 1991

Date departed: 26 May 1991

Time on hole: 1 day, 3 hr, 15 min

Position: 3° 5.802′S, 90° 49.074′W

Bottom felt (rig floor; m, drill-pipe measurement): 3307.5

Distance between rig floor and sea level (m): 11.7

Water depth (drill-pipe measurement from sea level, m): 3295.8

Total depth (rig floor; m): 3556.9

Penetration (m): 249.4

Number of cores (including cores with no recovery): 26

Total length of cored section (m): 245.4

Total core recovered (m): 247.85

Core recovery (%): 101.0

Oldest sediment cored:

Depth (mbsf): 249.4
Nature: nannofossil ooze
Earliest age: late Miocene

Principal results: Site 846 (EEQ-4), the southern most site of Leg 138's eastern transect, is located approximately 300 km due south of the Galapagos Islands. It is situated within the region of interaction between the South Equatorial Current (SEC) and the Peru Current. Drilling at this site was designed to examine the detailed history of the Peru Current, its interaction (or lack thereof) with the SEC, and the linkages between the history of these currents and global climatic change.

Four holes were drilled at the site (Table 1). Hole 846A was a single APC mudline core dedicated to whole-round geochemical and physical property measurements. Hole 846B was APC-cored to 206.5 mbsf, where excessive overpull (140,000 lb) necessitated a switch to the XCB-coring system. Hole 846B was continued with the XCB to basement at 422.4 mbsf, with 1.5 m of basalt recovered from the last core. The APC section was repeated in Holes 846C (to 192.5 mbsf) and 846D (to 163.3 mbsf) to ensure complete recovery of the section. Real-time analysis of continuous GRAPE, susceptibility, and color reflectance measurements showed that, after triple coring, there are no gaps in sediment recovery in this interval. In Hole 846D, three XCB cores were collected in an interval previously sampled by APC to examine the relative disturbance caused by each coring system. Initial analyses indicate that while the XCB causes slightly more disturbance than the APC, the quality of the material returned is excellent and well suited for high-resolution paleoceanographic studies. Hole 846D was continued to a final depth of 249.4 mbsf.

The sedimentary sequence can be divided into two lithologic units. Unit I (0–317 mbsf; middle Miocene to Pleistocene) alternates between carbonate (mostly nannofossil) ooze and siliceous (both diatom and radiolalarian) ooze. Unit II (317.0–419.2 mbsf; upper Miocene to middle Miocene) is composed mostly of nannofossil ooze. The upper portion of Unit II has minor siliceous constituents but contains several cherty intervals; the lower part is a nannofossil chalk with foraminifers; siliceous microfossils are virtually absent. A thin sequence of metal-liferous sediments lies immediately above basaltic basement.

The continuous sedimentary section spans the time interval from the Quaternary to the lower Miocene with a 300-m thick, expanded sequence from the Pleistocene through the upper half of the Miocene. Sedimentation rates during this interval were in excess of 40 m/m.y. The lower half of the sequence is more condensed with the upper to lower Miocene represented by approximately 120 m of section. A marked change in sedimentation rate occurs at approximately 7.1 Ma with the interval spanning the middle/late Miocene boundary accumulating at approximately 12 m/m.y. The base of the sequence is assigned to the lower Miocene calcareous nannofossil Zone CN3, with an approximate age of 16.5 Ma.

Biostratigraphic age control was provided by all four of the chief planktonic microfossil groups, although their abundances and state of preservation are quite variable throughout. Radiolarians and diatoms are abundant from the upper Miocene to the Pleistocene; in the middle Miocene they begin to show signs of dissolution and in the lower middle Miocene and lower Miocene they are absent. Calcareous nan-nofossils are generally abundant and well-preserved throughout the section with the exception of the lowermost upper Miocene, where they are rare and poorly preserved. Planktonic foraminifers are common in the Pleistocene and Pliocene but their abundance and preservation deteriorates down section.

The paleomagnetic signal at Site 846 was weak, and it was impossible to reliably determine direction. A weak and "soft" remanence was observed, but will have to await shore-based work for evaluation. The susceptibility record, while of low amplitude, may be correlative from hole-to-hole.

Three logging runs were conducted in Hole 846B using the standard lithostratigraphic string, geochemical string, and the formation microscanner. Logs are of excellent quality and provide an important cross-check against both continuous and discrete laboratory physical property measurements. Both the logs and the laboratory measurements show much fine-scale cyclicity. The ability to correlate even these high-frequency changes between laboratory and log results increases our confidence in both sets of measurements. Logging units, defined by changes in the shape of the logs, correlate extremely well with the independently determined lithologic units.

Interstitial-water sampling shows the influence of diagenesis, recrystallization, and basalt alteration on the sediments of Site 846. A mildly reducing environment is indicated by profiles of alkalinity, sulfate, ammonia, and the smell of H_2S. Calcium, silica, and strontium profiles indicate ongoing recrystallization, most pronounced in the Miocene. The alteration of basement rocks is shown in the profiles of magnesium, calcium, potassium, lithium, and strontium, and the first appearance of chert is dramatically indicated by a decrease in interstitial silica.

Table 1. Summary of coring operations at Site 846.

Core no.	Date (May 1991)	Time (UTC)	Depth (mbsf)	Length cored (m)	Length recovered (m)	Recovery (%)
138-846A						
1H	21	2330	0–7.2	7.2	7.22	100.0
Coring totals				7.2	7.22	100.0
138-846B						
1H	22	0005	0–7.0	7.0	7.05	101.0
2H	22	0130	7.0–16.5	9.5	9.89	104.0
3H	22	0220	16.5–26.0	9.5	9.67	102.0
4H	22	0355	26.0–35.5	9.5	10.06	105.9
5H	22	0445	35.5–45.0	9.5	10.04	105.7
6H	22	0540	45.0–54.5	9.5	8.94	94.1
7H	22	0625	54.5–64.0	9.5	9.76	103.0
8H	22	0715	64.0–73.5	9.5	9.96	105.0
9H	22	0800	73.5–83.0	9.5	9.57	101.0
10H	22	0850	83.0–92.5	9.5	10.23	107.7
11H	22	0935	92.5–102.0	9.5	9.76	103.0
12H	22	1020	102.0–111.5	9.5	9.80	103.0
13H	22	1105	111.5–121.0	9.5	10.15	106.8
14H	22	1155	121.0–130.5	9.5	9.78	103.0
15H	22	1240	130.5–140.0	9.5	10.12	106.5
16H	22	1330	140.0–149.5	9.5	9.82	103.0
17H	22	1415	149.5–159.0	9.5	10.15	106.8
18H	22	1500	159.0–168.5	9.5	10.17	107.0
19H	22	1550	168.5–178.0	9.5	10.15	106.8
20H	22	1635	178.0–187.5	9.5	9.85	103.0
21H	22	1720	187.5–197.0	9.5	10.18	107.1
22H	22	1835	197.0–206.5	9.5	10.10	106.3
23X	22	1935	206.5–216.2	9.7	9.76	100.0
24X	22	2025	216.2–225.9	9.7	9.58	98.7
25X	22	2110	225.9–235.6	9.7	6.42	66.2
26X	22	2155	235.6–245.2	9.6	0.01	0.1
27X	22	2240	245.2–254.9	9.7	8.36	86.2
28X	22	2330	254.9–264.2	9.3	9.97	107.0
29X	23	0015	264.2–273.9	9.7	9.54	98.3
30X	23	0055	273.9–283.5	9.6	9.85	102.0
31X	23	0140	283.5–293.1	9.6	9.84	102.0
32X	23	0230	293.1–302.8	9.7	9.28	95.7
33X	23	0315	302.8–312.4	9.6	9.88	103.0
34X	23	0400	312.4–322.0	9.6	9.89	103.0
35X	23	0450	322.0–331.7	9.7	9.72	100.0
36X	23	0530	331.7–341.3	9.6	9.83	102.0
37X	23	0615	341.3–351.0	9.7	3.71	38.2
38X	23	0705	351.0–360.6	9.6	9.20	95.8
39X	23	0800	360.6–370.3	9.7	0.00	0.0
40X	23	0855	370.3–379.9	9.6	7.89	82.2
41X	23	0945	379.9–389.6	9.7	7.21	74.3
42X	23	1045	389.6–399.2	9.6	1.36	14.1
43X	23	1140	399.2–408.9	9.7	0.21	2.2
44X	23	1250	408.9–418.6	9.7	5.24	54.0
45X	23	1435	418.6–422.4	3.8	1.49	39.2
Coring totals				422.6	373.44	88.4
138-846C-						
1H	24	1530	2.5–12.0	9.5	9.70	102.0
2H	24	1630	12.0–21.5	9.5	9.84	103.0
3H	24	1730	21.5–31.0	9.5	9.95	105.0
4H	24	1820	31.0–40.5	9.5	10.09	106.2
5H	24	1915	40.5–50.0	9.5	10.19	107.2
6H	24	2005	50.0–59.5	9.5	8.64	90.9
7H	24	2050	59.5–69.0	9.5	10.21	107.5
8H	24	2145	69.0–78.5	9.5	9.36	98.5
9H	24	2235	78.5–88.0	9.5	9.13	96.1
10H	24	2325	88.0–97.5	9.5	9.95	105.0
11H	25	0020	97.5–107.0	9.5	9.24	97.2
12H	25	0110	107.0–116.5	9.5	9.52	100.0
13H	25	0155	116.5–126.0	9.5	9.75	102.0
14H	25	0245	126.0–135.5	9.5	9.17	96.5
15H	25	0330	135.5–145.0	9.5	9.72	102.0
16H	25	0415	145.0–154.5	9.5	9.74	102.0
17H	25	0500	154.5–164.0	9.5	9.72	102.0
18H	25	0545	164.0–173.5	9.5	9.34	98.3
19H	25	0630	173.5–183.0	9.5	9.84	103.0
20H	25	0725	183.0–192.5	9.5	10.00	105.2
Coring totals				190.0	193.10	101.6
138-846D-						
1H	25	0935	4.0–13.5	9.5	9.29	97.8
2H	25	1015	13.5–23.0	9.5	8.11	85.3
3H	25	1055	23.0–32.5	9.5	9.93	104.0
4H	25	1155	32.5–42.0	9.5	10.19	107.2
5H	25	1235	42.0–51.5	9.5	10.10	106.3
6H	25	1330	51.5–58.8	7.3	9.88	135.0
7H	25	1410	58.8–68.3	9.5	9.90	104.0
8H	25	1455	68.3–77.8	9.5	9.98	105.0
9H	25	1545	77.8–87.3	9.5	10.22	107.6
10H	25	1635	87.3–96.8	9.5	10.10	106.3
11H	25	1720	96.8–106.3	9.5	9.46	99.6
12H	25	1810	106.3–115.8	9.5	9.61	101.0
13H	25	1855	115.8–125.3	9.5	10.09	106.2
14H	25	1940	125.3–134.8	9.5	9.01	94.8
15H	25	2025	134.8–144.3	9.5	10.10	106.3
16H	25	2110	144.3–153.8	9.5	10.01	105.3
17H	25	2155	153.8–163.3	9.5	9.81	103.0
18X	25	2255	163.3–172.8	9.5	4.65	48.9
19X	25	2345	172.8–182.3	9.5	9.64	101.0
20X	25	0030	181.8–191.4	9.6	9.79	102.0
21X	25	0115	191.4–201.1	9.7	9.81	101.0
22X	25	0200	201.1–210.7	9.6	9.64	100.0
23X	25	0240	210.7–220.4	9.7	9.46	97.5
24X	25	0325	220.4–230.1	9.7	9.66	99.6
25X	25	0410	230.1–239.8	9.7	9.76	100.0
26X	25	0500	239.8–249.4	9.6	9.65	100.0
Coring totals				245.9	247.85	100.8

While this site was "Leadsville" for paleomagnetism data, the combination of complete recovery, well-defined biostratigraphy, multiple, continuous high-resolution laboratory records (GRAPE, *P*-wave velocity, susceptibility, and color), and an excellent suite of logs ensure that Site 846 will be a "platinum mine" for high-resolution paleoclimate and paleoceanographic studies.

BACKGROUND AND SCIENTIFIC OBJECTIVES

Site 846, the southernmost site of the eastern Leg 138 transect, is located approximately 300 km due south of the Galapagos Islands. It is situated within the region of interaction between the South Equatorial Current (SEC) and the Peru Current and was designed to examine the detailed history of this eastern boundary current and its linkage (or lack thereof) with the SEC (Fig. 1).

Site 846 is located on the southern limb of the Carnegie Ridge on crust formed at the Galapagos Spreading Center (Hey, 1977). The absolute backtrack of these sites is constrained by the Pacific-Nazca pole of rotation, which can be referenced to the Pacific absolute pole via the Hawaiian and other Pacific trends and by the Galapagos hot-spot trace. The calculated backtrack path for Site 846 implies that the site has remained near its present latitude for most of its history and thus the site should serve as important reference for the history of equatorial circulation (Fig. 2).

The primary objective of drilling at Site 846 was to obtain a detailed, high-resolution record of the history of the Peru Current and eastern part of the South Equatorial Current extending well into the Miocene.

Seismic and SeaBeam bathymetric data collected during the site survey cruise (*Thomas Washington* Venture 1 cruise; see Mayer et al., this volume) reveal that the surficial topography in the general area of Site 846 is relatively flat with less than 25 m of relief (Fig. 3). At the western edge of the survey area is a north-south oriented feature that has approximately 150 m of relief and which may be the continuation of the Galapagos Island Fracture Zone inferred by Hey et al. (1977) and shown in Figure 2 north of Site 846 and the Galapagos Islands. This feature was not surveyed with SeaBeam on the original site survey cruise but was mapped by the *JOIDES Resolution* during the transit from Site 845 to Site 846. Associated with this boundary we observed a sharp offset in the amplitude of the marine magnetic anomaly pattern.

The seismic record in the vicinity of Site 846 shows 0.525 s (two-way traveltime) representing 420 m of acoustically well-laminated sediments (Fig. 4).

OPERATIONS

Site 846

Our original operations plan after leaving Site 845 was for drilling proposed Site EEQ-3. To pick up two multishot cameras and batteries for the cameras, the operations plan was changed to drill proposed Site EEQ-4 first. This change would allow the ship to pass directly by Baltra, in the Galapagos Islands, while on its way to Site EEQ-4 and to rendezvous with a small boat carrying the necessary supplies. The *JOIDES Resolution* arrived at the rendezvous point near Baltra at 1320 hr (all times in this section are reported in local time, L, where local time = Universal Time Coordinated, UTC minus 6 hr; all times in Table 1 are in UTC), 20 May, after sailing 650 nmi from Site 845 at an average speed of 10.3 kt. Two multishot cameras, AA batteries for the cameras, mail, and an electronic thermometer were off-loaded from the *Moby Dick*, and the *JOIDES Resolution* continued on its transit to proposed Site EEQ-4.

The transit from Baltra to Site EEQ-4 traversed 177 nmi at an average speed of 10.1 kt. Upon arrival at the initial survey way point at 0700L 21 May, a short seismic survey was conducted over the site. At 0948L 21 May, a beacon was released and the vessel returned to the site location. By 1030L 21 May, thrusters and hydrophones were lowered and the ship was on location. The depth to seafloor, based upon the precision depth recorder (PDR), was 3310.4 mbrf.

Hole 846A

Core 138-846A-1H was retrieved at 1730L 21 May and from it was recovered 7.22 m of sediment to establish the depth of the mud line at 3307.3 mbrf (see Table 1 for a summary of coring statistics). This core was taken for physical property and geochemical whole-round samples and constituted the entire coring at Hole 846A.

Hole 846B

The second mud-line core at this site (Core 138-846B-1H) was retrieved at 1805L 21 May and from it we recovered 7.05 m of sediment. The drill-pipe measurement of the mud-line depth was 3307.5 mbrf. Cores 138-846B-1H through -21H were retrieved successfully over the interval from 0 to 197.0 mbsf, and all APC cores, beginning with Core 138-846B-4H, were oriented. The core barrel became stuck upon retrieval of Core 138-846B-22H (197.0–206.5 mbsf) but was successfully retrieved after washing 2 m over the barrel and applying 140,000 lb of overpull. The average recovery for this APC-cored interval was 104.2%.

At 1300L 22 May, coring resumed with the XCB-coring system and Cores 138-846B-23X through -44X (206.5–418.6 mbsf) were retrieved successfully, when coring continued toward basement. Basement was reached at 420 mbsf, and total depth was reached at 422.4 mbsf (Core 138-846B-45X). This last core was advanced 3.8 m and from it was recovered 1.5 m of basalt. The average recovery for the entire XCB sequence was 73.3%. Below 341.3 mbsf (Core 138-846B-36X), core recovery was poor (44%), most likely the result of chert stringers interbedded with nannofossil chalk and metalliferous sediments. As depth objectives for this hole had been reached after Core 138-846B-45X, coring ceased and preparations for logging began.

Logging Operations—Hole 846B

After sweeping the hole with mud, the pipe was pulled back to the logging depth of 76 mbsf and the hole was logged using the three standard ODP tool strings. A summary of the logging operations is presented in Table 2.

The geophysical string was run first, and the main and repeat passes were made with the heave compensator turned on. The main logging run was from 420.9 to 85.0 mbsf. The section between 420.9 and 335.0 mbsf was logged again to remove a bad wire wrap on the winch near the bottom of the hole.

The geochemical tool string was run next and no problems were encountered while calibrating the GST. The geochemical string also was run with the heave compensator turned on. Data were collected from 419.7 to 75.9 mbsf, and some difficulty was encountered in getting the tool back into the pipe. Thus there is the possibility that activated "hot spots" occur just above 76 mbsf, where the GST passed the same interval several times. Once the tool was in the pipe, logging continued up to the mudline, after which the tool string was brought on deck.

The FMS logging run went smoothly. The hole was logged from 419.1 to 197.8 mbsf on the first pass and from 421.5 to 66.4 mbsf on the second pass. The lower portion of the hole was logged twice to ensure adequate coverage where the hole conditions were optimal for FMS measurements. This interval also had the poorest sediment recovery. No problems were encountered during either pass.

At the conclusion of the logging program, the drill string was pulled out of the hole and the bit cleared the mudline at 0608 hr, 24 May, thereby ending Hole 846B.

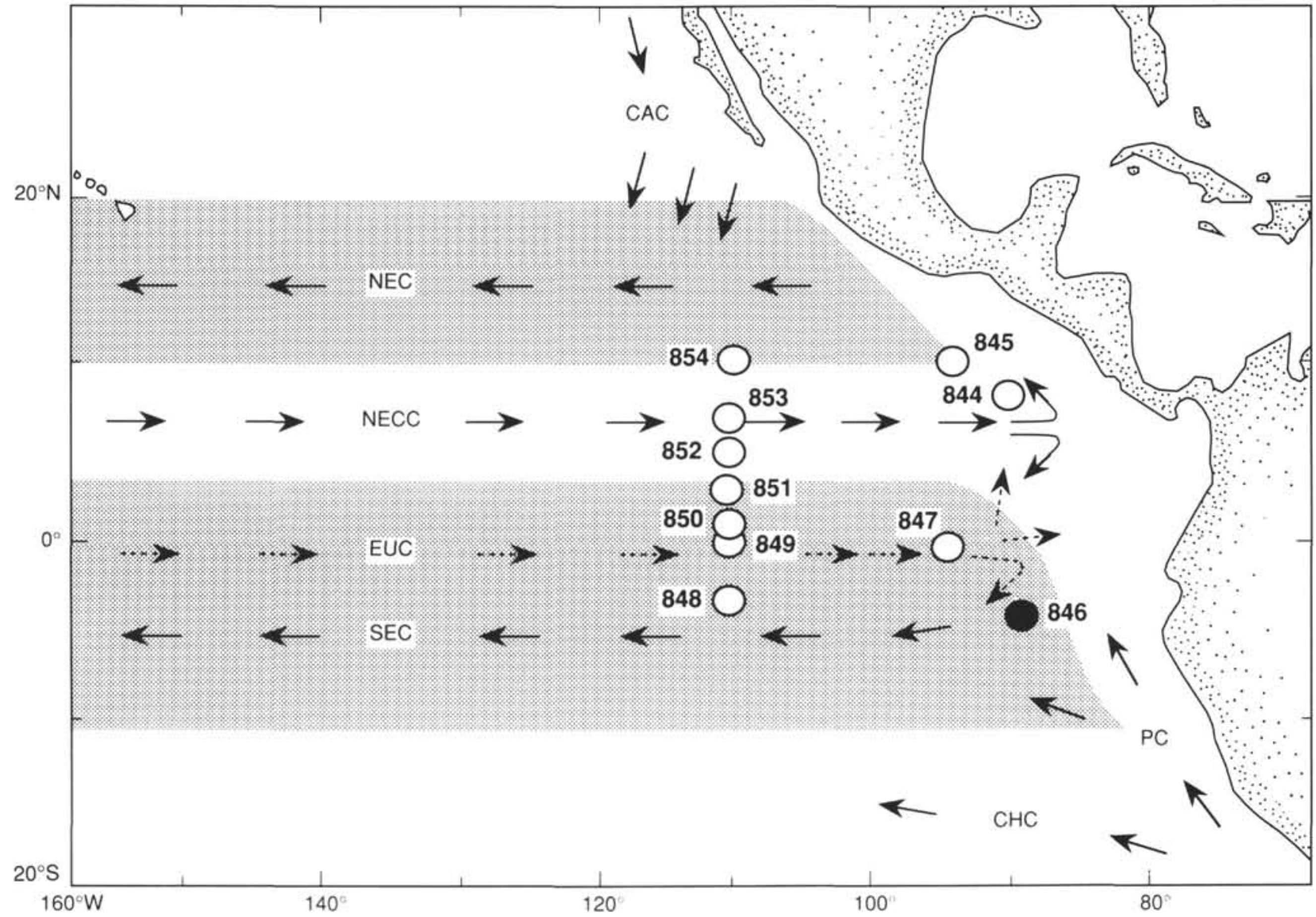

Figure 1. Location of Site 846 and other Leg 138 sites and generalized circulation system of the eastern equatorial Pacific Ocean. Surface current shown as solid arrows; subsurface current as dashed arrows. CAC = California Current; NEC = North Equatorial Current; NECC = North Equatorial Countercurrent; EUC = Equatorial Undercurrent; SEC = South Equatorial Current; PC = Peru Current; and CHC = Chile Current. Shaded areas illustrate general latitudinal extent of the SEC and NEC.

Hole 846C

The vessel was offset 20 m south and at 0930 hr, 24 May, Hole 846C was spudded and washed down to 2.5 mbsf where Core 138-846C-1H was taken. The first three core barrels (Core 138-846C-1H through -3H; 2.5–31.0 mbsf) required significant overpull and jarring before the inner barrel could be released from the outer core barrel. The inner shear pin/landing shoulder sub was replaced after the third core and mud was circulated to flush any debris that may have fouled the landing saver sub. There were no more problems with the core barrels getting stuck.

Cores 138-846C-4H through -20H were taken successfully over the interval from 31.0 to 192.5 mbsf. All cores after Core 138-846C-3H were oriented. To ensure that significant overpull was not encountered during Hole 846C drilling operations, APC-coring was terminated at Core 138-846C-20H. The average recovery for the hole was 101.6%.

Hole 846D

The pipe was pulled just above the mudline at 0227 hr, 25 May, and the ship was offset 20 m west. The bit was washed down 4 m, and APC coring was resumed at 0335 hr with Core 138-846D-1H (4.0–13.5 mbsf) and continued without any problems to Core 138-846D-17H (163.3 mbsf). Core 138-846D-6H was advanced only 7.3 m to achieve a better overlap of the sedimentary record with the previous holes on this site. All piston cores after Core 138-846D-3H were oriented. The APC coring program ended after Core 138-846D-17H, well before refusal depth. Drilling operations were switched over to the XCB system at this point to obtain several XCB cores over the same depth interval as APC cores in the previous hole. This comparison hopefully will provide insight into coring disturbances associated with each coring system.

Cores 138-846B-18X through -26X were taken successfully, and drilling operations ended when the depth objective for this hole was reached after Core 138-846C-26X. The average recovery for the XCB portion of the hole was 95.3%.

The pipe was tripped out of the hole after Core 138-846D-26X was retrieved, and the bit was on deck at 0528 hr, 26 May, ending Hole 846D. After the hydrophones and thrusters were retracted and the rig floor secured, the *JOIDES Resolution* was underway toward proposed Site EEQ-3 at 0545 hr, 26 May.

LITHOSTRATIGRAPHY

Introduction

The sediments at Site 846 are composed primarily of nannofossil and diatom oozes of Pleistocene to middle Miocene age (Fig. 5). Drilling of four holes recovered a complete sedimentary section

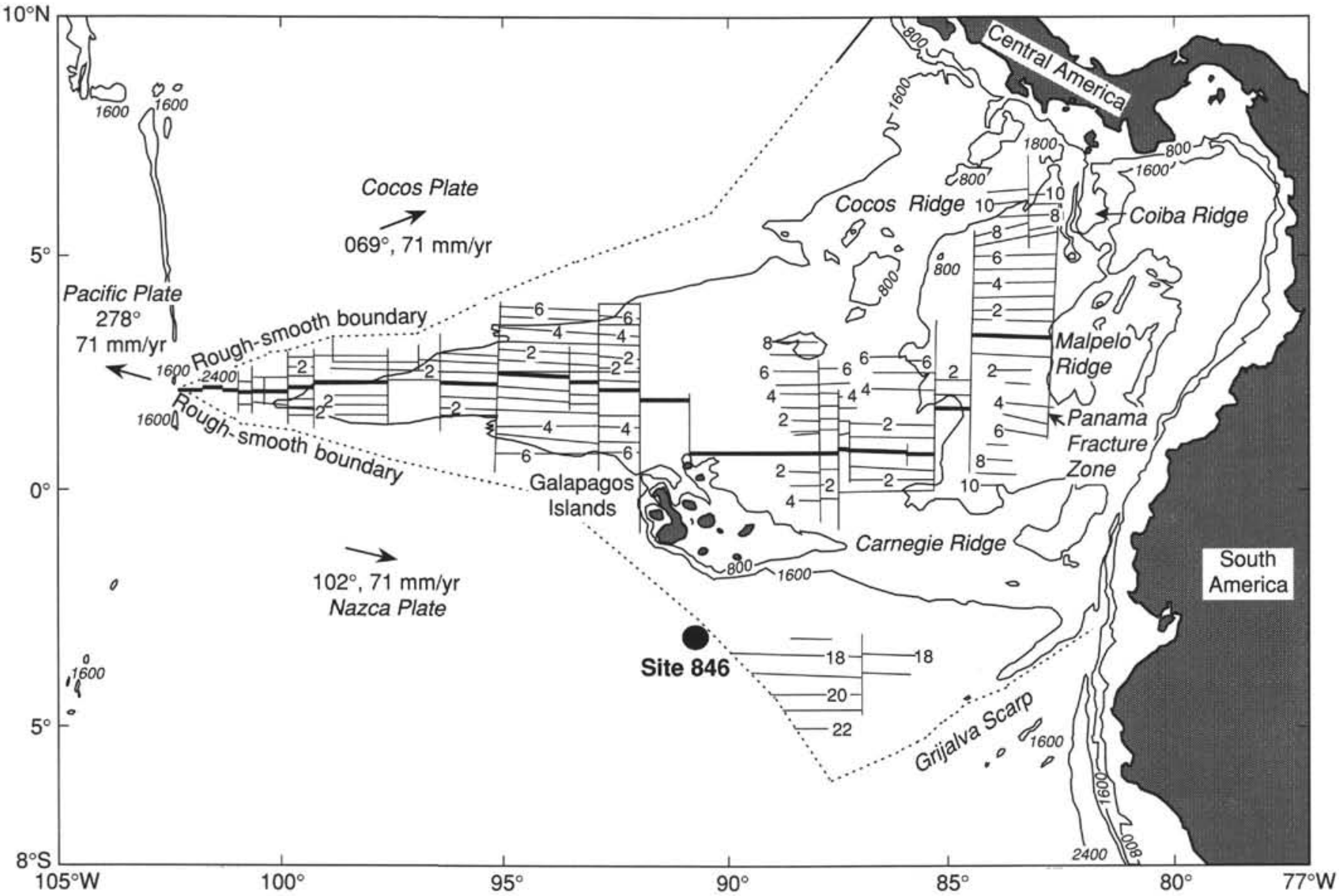

Figure 2. Tectonic setting and basement ages for the eastern equatorial Pacific Ocean (from Hey, 1977). Location of Site 846 is shown.

above the deepest APC core (206.5 mbsf). At one hole, 846B, drilling continued to basalt basement, which is overlain by a thin sequence of metalliferous sediment.

We divided the Site 846 sediments into two lithostratigraphic units primarily using visual core descriptions, smear-slides analyses (Fig. 6), $\%CaCO_3$ measurements, continuously-measured lithologic parameters including GRAPE bulk density, and digital color reflectance spectroscopy (Fig. 7). These data were augmented by a few X-ray diffraction and X-ray fluorescence measurements, to characterize nonbiogenic sediments. Logging data were used to constrain the ooze-chalk transition. The continuously measured parameters were used for fine-scale correlation between holes, especially in the APC cores (see Sedimentation Rates section, this chapter). For Site 846, the color reflectance data (Fig. 8) were particularly useful in defining units, as they recorded information similar to visual descriptions but at greater resolution (intervals ranging from 4–8 cm) than can be recorded in visual descriptions or smear-slide analyses.

The description of units is intended as a guide to the average character of the sediments. A large amount of high-frequency (meter-scale) variability exists in the sediments at Site 846; thus, the choice of boundaries between large-scale units and subunits inevitably simplifies complex patterns. The sediments from Site 846 form two lithologic units (Fig. 5). Unit I is variable and alternates between carbonate (mostly nannofossil) ooze and siliceous (both diatom and radiolarian) ooze. Its calcium carbonate content ranges from 0% to 90%. Unit II is less variable, and is composed mainly of nannofossil ooze and chalk. The upper section of Unit II contains up to 20% diatoms, while the lower section is essentially barren of biogenic silica (generally less than 5%, and usually <1%) in the recovered sediments.

A thin sequence of metalliferous sediments, included in Unit II, was recovered immediately above basalt basement.

Description of Units

Unit I

Intervals:
- Core 138-846A-1H (bottom not reached)
- Cores 138-846B-1H through -34X-4, 110 cm
- Cores 138-846C-1H through -20H (bottom not reached)
- Cores 138-846D-1H through -26X (bottom not reached)

Depth: 0–317.0 mbsf in Hole 846B
Age: Pleistocene to middle Miocene (about 0–10.6 Ma)

Unit I contains interbedded nannofossil ooze, diatom nannofossil ooze, nannofossil diatom ooze, and clayey radiolarian diatom ooze. We divided Unit I into two subunits. Subunit IA is Pleistocene to late Miocene in age (0 to about 7.0 Ma) and varies between dominant nannofossil diatom ooze and subordinate diatom nannofossil ooze or nannofossil ooze. Subunit IB, of late to middle Miocene age (ca. 7.0–10.6 Ma) is highly siliceous and is dominated by diatom and radiolarian oozes, with minor interbedded nannofossil ooze.

Subunit IA

Intervals:
- Core 138-846A-1H (bottom not reached)
- Cores 138-846B-1H through -28X-6, 30 cm
- Cores 138-846C-1H through -20H (bottom not reached)

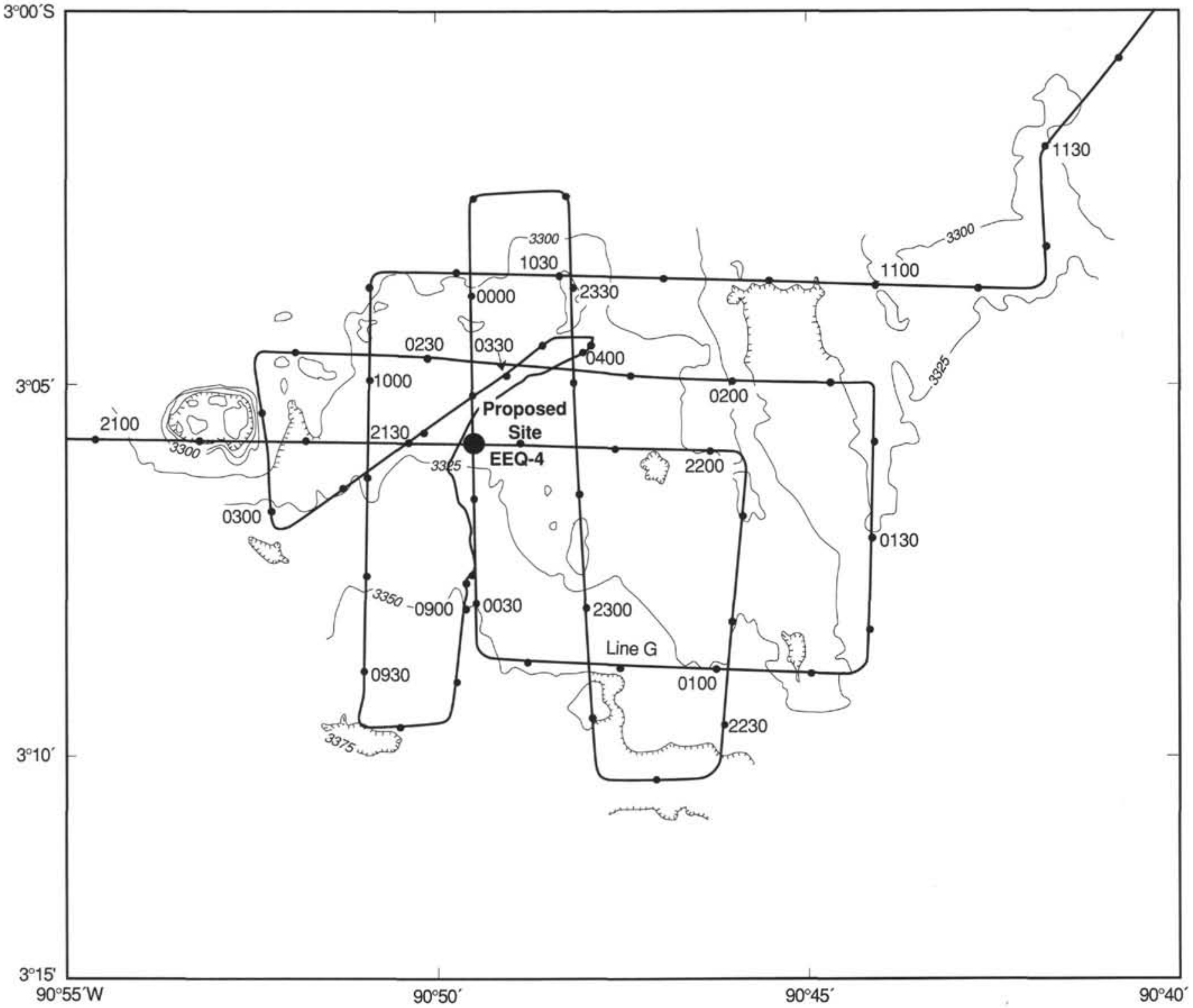

Figure 3. SeaBeam map hand-contoured from navigation-adjusted SeaBeam contour maps collected on board the *Thomas Washington* during the Venture 1 cruise, September 1989. Proposed Site EEQ-4 is shown.

Cores 138-846D-1H through -26X (bottom not reached)
Depth: 0–262.7 mbsf (Hole 846B)
Age: Pleistocene to late Miocene (about 0–7.0 Ma)

Subunit IA contains 262.7 m of compositionally banded sediment composed of varying proportions of diatoms, radiolarians, nannofossils, and foraminifers, with minor amounts of clay. The lithologies encountered include nannofossil foraminifer diatom ooze, foraminifer diatom nannofossil ooze, and nannofossil ooze, although diatom nannofossil ooze is most common. The top 52.5 m (Cores 1–6 in all holes) are dominated by light greenish to bluish-gray (5GY 7/1 to 5Y 6/1) foraminifer diatom nannofossil oozes (~50% nannofossils, 20% diatoms, 20% foraminifers), but contain frequent bands of olive-colored diatom ooze (up to 50% diatoms). Color reflectance values are generally high, but variable, from about 30% to 70% in the visible bands. Calcium carbonate content is also variable and ranges from 25% to 80%.

From 52.5 to 80 mbsf (Cores 6–9 in Holes 846B, 846C, and 846D), diatom ooze is dominant, although nannofossil ooze continues to be present as interbeds (10%–40%). Clay is more abundant here than in the top 52.5 m (up to 30%). The nonbiogenic sediment fraction is dominated by smectite, plagioclase, quartz, and barite. The sediments are darker, with typical colors of olive gray to dark olive (5Y 6/2 to 5Y 3/2), and low color reflectance values, typically 20% to 30% in the visible bands.

Between 80 and 200 mbsf (Cores 9–22 in Holes 846B, 846C, and 846D), the lithology of Subunit IA again is highly variable and ranges from nannofossil ooze to diatom ooze, although nannofossil ooze (50%–80% nannofossils) with foraminifers and diatoms is most abundant. Calcium carbonate content varies widely, from 15% to 90% (see "Organic Geochemistry" section, this chapter). Visible reflectance is similarly variable, from 25% to 85%, and the color ranges from light gray to dark olive (5Y 7/2).

Diatoms decrease to less than 5% abundance from 200 to 245 mbsf (Cores 22X–25X in Hole 846B and Cores 22H–26X in Hole 846D). Here, the sediment is nannofossil ooze or foraminifer nannofossil ooze, with clay content of up to 20%. The plagioclase content of the nonbiogenic fraction of the sediment is much lower than in the upper 200 m (absent in some samples). The colors are generally light gray

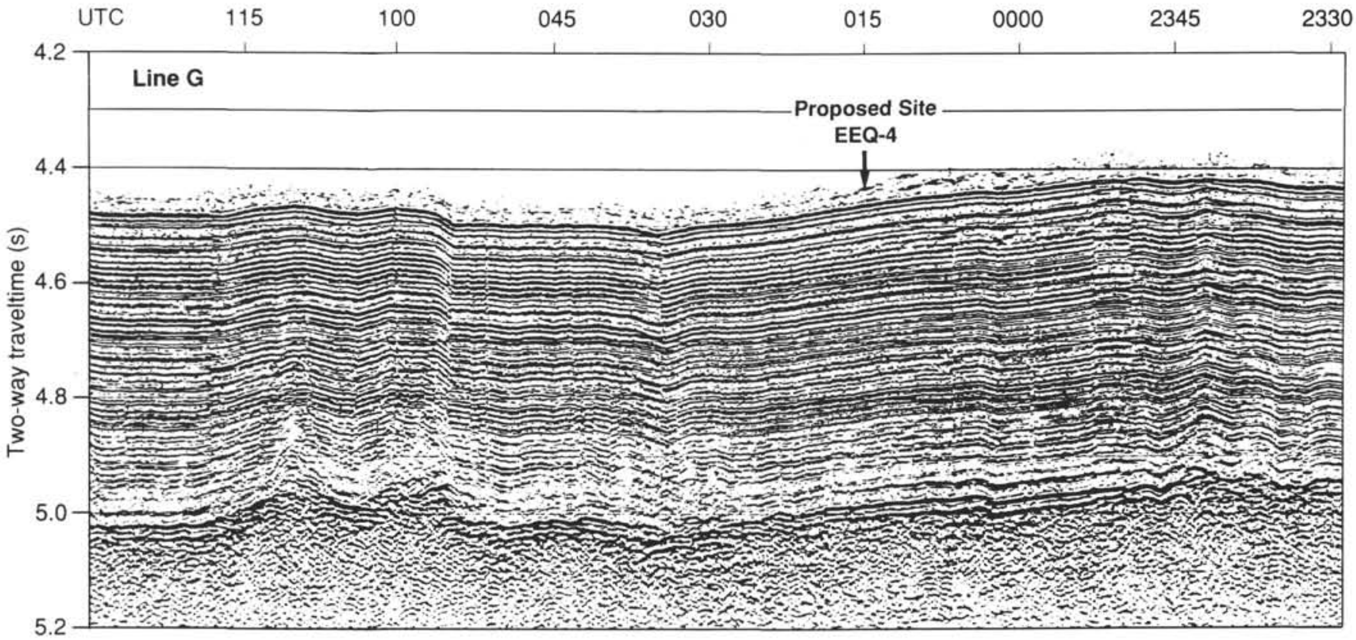

Figure 4. Seismic Line G. 80-in.^{3} water-gun record collected during the *Thomas Washington* cruise Venture 1. Proposed site EEQ-4 is shown.

Table 2. Summary of logging operations at Site 846.

Day (May 1991)	Time (L)	Cumulative hours	Base of string (mbsf)	Comments
23	8:35	0.0		Last core on deck.
23	11:00	2.4		Start rig up.
23	12:20	3.8		Geophys.tool rigged up (NGT/SDT/HLDT/DIT/TLT); RIH
23	13:18	4.7	0.0	pause at mud line.
23	13:27	4.9	135.3	Start downlog, heave compensator on.
23	13:50	5.3	420.9	Stopped downlog; at TD.
23	14:08	5.5	420.9	At TD, start main log up (NGT/SDT/HLDT/DIT/TLT).
23	15:20	6.8	85.0	Stop up log, go back to TD for repeat section.
23	15:32	6.9	420.9	Start repeat up log at TD.
23	15:50	7.2	335.0	End repeat section; close calipers and POOH.
23	16:45	8.2		Geophys. tool string at well head.
23	18:35	10.0		RIH w/ Geochem String (NGT/ACT/GST/TLT).
23	20:00	11.4	417.2	near TD; turn heave comp on; calibrate while moving up slowly.
23	20:11	11.6	419.7	Start main log w/ Geochem String from TD.
23	22:05	13.5	75.9	Stop main log to turn heave compensator off.
23	22:24	13.8	63.1	Enter pipe after some difficulty.
23	22:44	14.1	0.0	Stop main log; POOH.
23	23:50	15.2		Geochem. string at wellhead.
24	0:55	16.3		RIH w/ FMS string (NGT/GPIT/FMS/TLT).
24	2:25	17.8	419.1	At TD, start FMS repeat log; heave compensator on.
24	2:55	18.3	197.8	Stop repeat log; drop back to TD for main log.
24	3:07	18.5	421.5	Start main FMS log at TD.
24	3:53	19.3	66.4	Stop main FMS log.
24	4:02	19.4		POOH FMS string; some trouble getting into pipe.
24	5:12	20.6		FMS string at wellhead.
24	5:40	21.1		Rigged down from logging.

to light greenish gray (5Y 7/1 to 5GY 7/1) in this interval, and visible reflectance is moderate to high, ranging from 35% to 70%. A coring gap in Hole 846B, between 235.6 and 245.2 mbsf (Core 138-846B-26X), was recovered in Cores 138-846D-25X and -26X. The sediment in this interval is nannofossil ooze, similar to that of the surrounding material in both holes. The base of Subunit IA is the first occurrence of clayey radiolarian diatom ooze, in Section 138-846B-28X-6, 30 cm.

Subunit IB

Intervals:
Cores 138-846B-28X-6, 30 cm, through -34X-4, 110 cm
Depth: 262.7–317.0 mbsf, Hole 846B
Age: late to middle Miocene (about 7.0–10.6 Ma)

Subunit IB contains 54.3 m of distinctive radiolarian-rich sediment (up to 30% radiolarians), including clayey radiolarian diatom ooze, radiolarian diatom nannofossil ooze, and diatom nannofossil ooze with radiolarians. From 262.7–290 mbsf (Cores 138-846B-28X to -31X), the sediment is mainly a clayey radiolarian diatom ooze and ranges from gray to dark olive (5Y 6/2 to 5Y 4/1). Pale light-gray bands within this subunit are radiolarian diatom nannofossil ooze.

Below 290 mbsf (Cores 138-846B-31X to -34X), the sediment is highly siliceous diatom ooze, with concentrations of radiolarians up to 30%. The interval from 290 to 313 mbsf becomes progressively darker and ranges from olive to black (5Y 4/3 to 5Y 2.5/1). This zone has carbonate contents of less than 30%, and low visible reflection of 10%–30%. Below 313 mbsf, the nannofossil content increases rapidly. The base of Subunit IB is the first

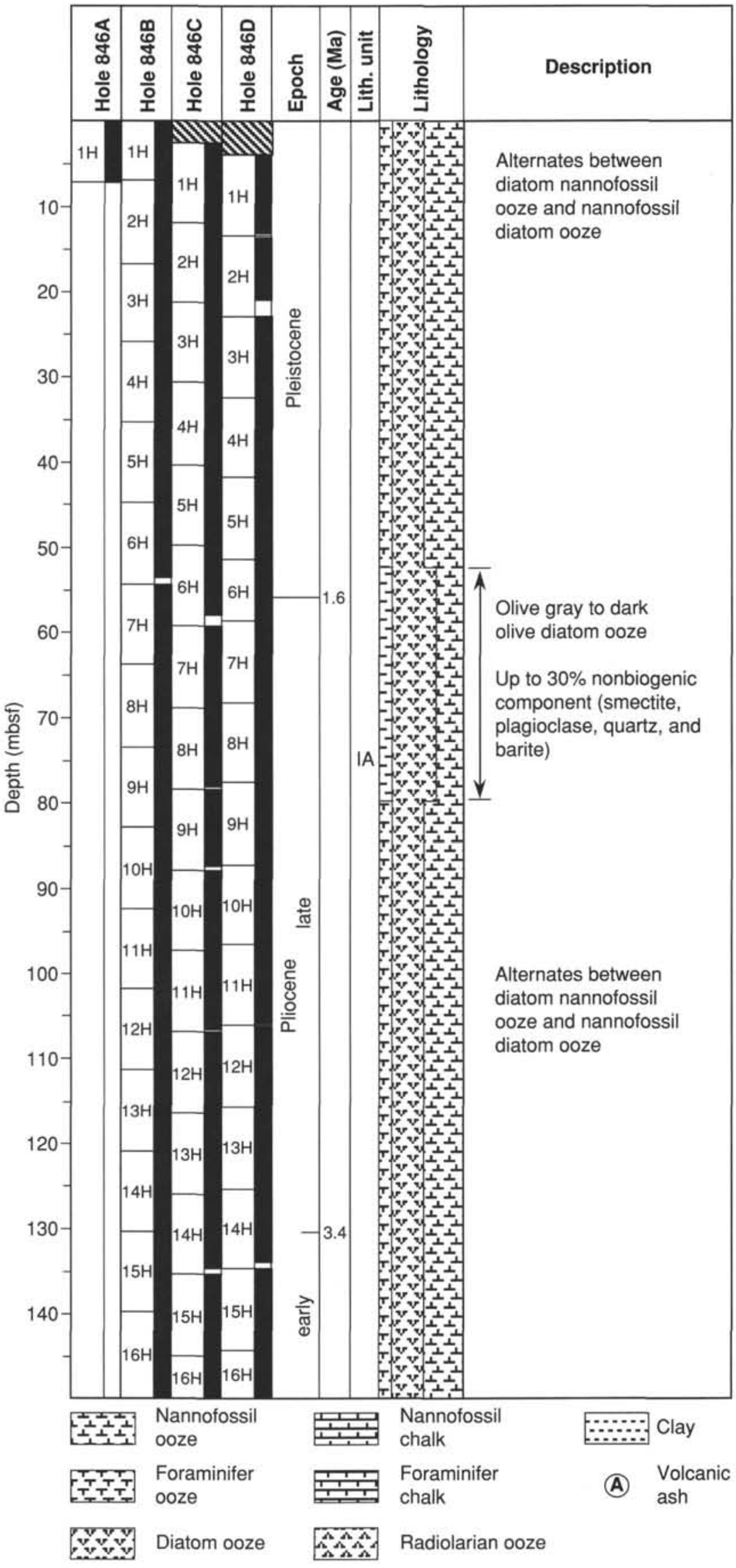

Figure 5. Lithostratigraphic summary of Site 846.

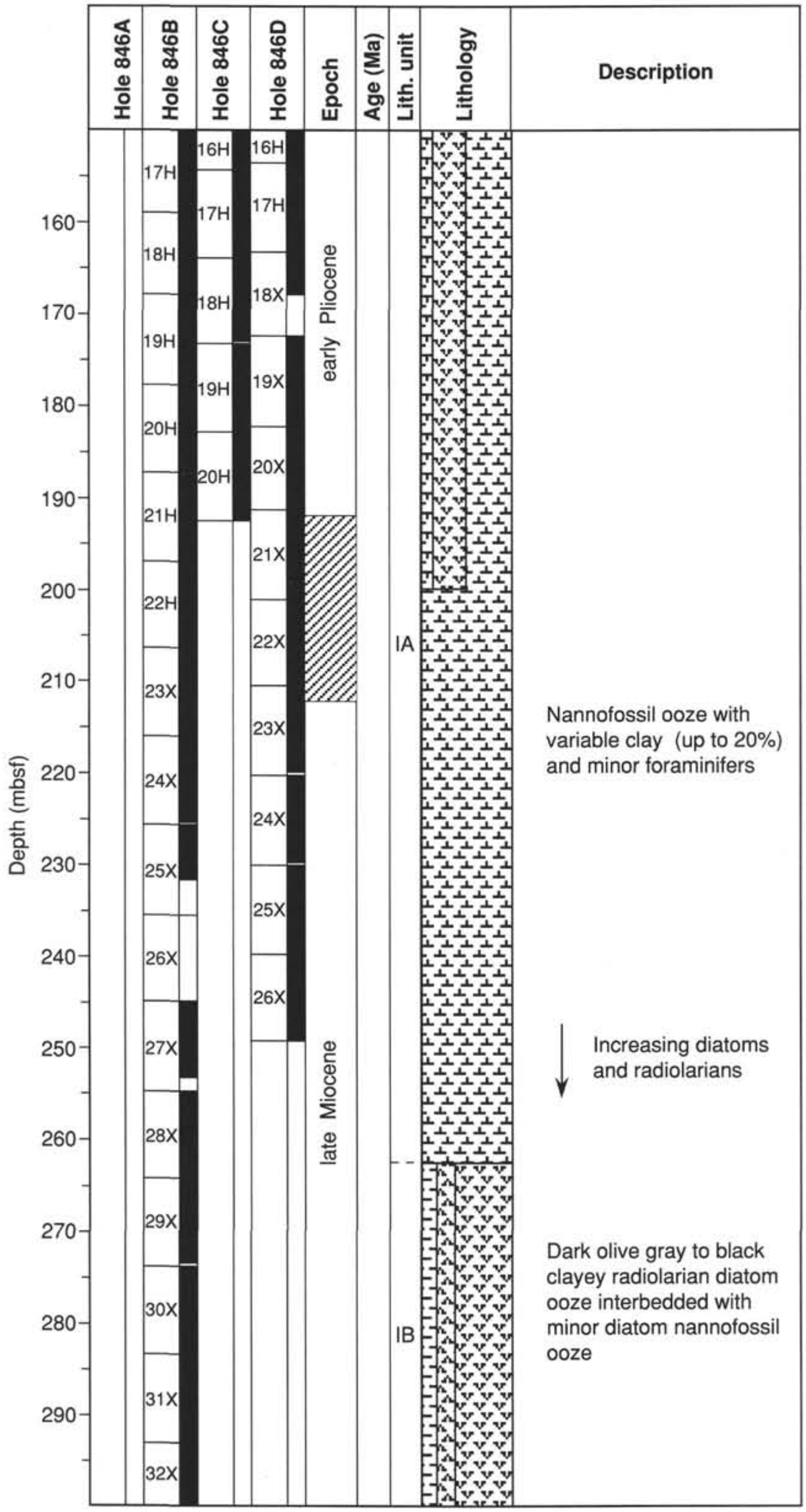

Figure 5 (continued).

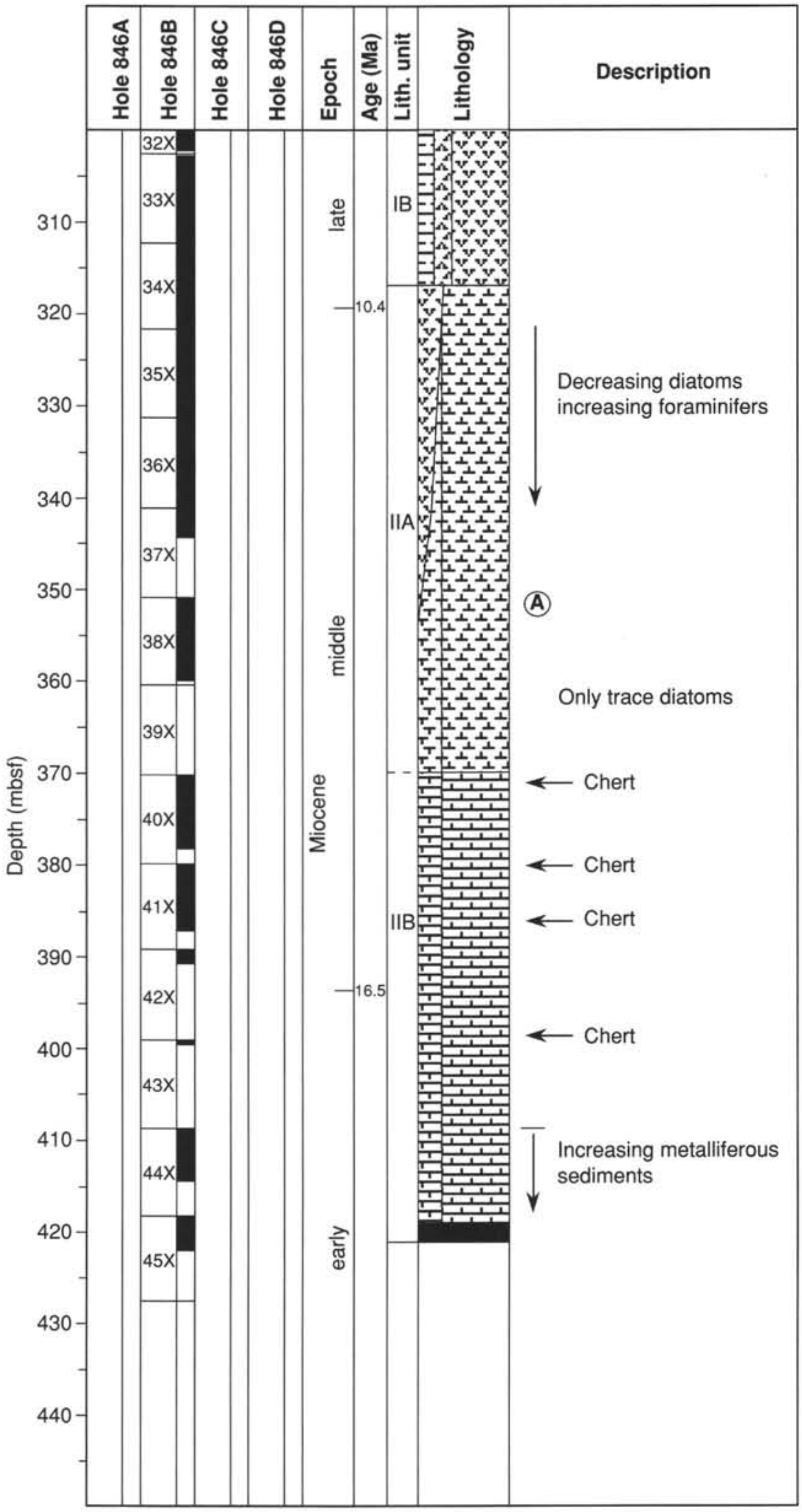

Figure 5 (continued).

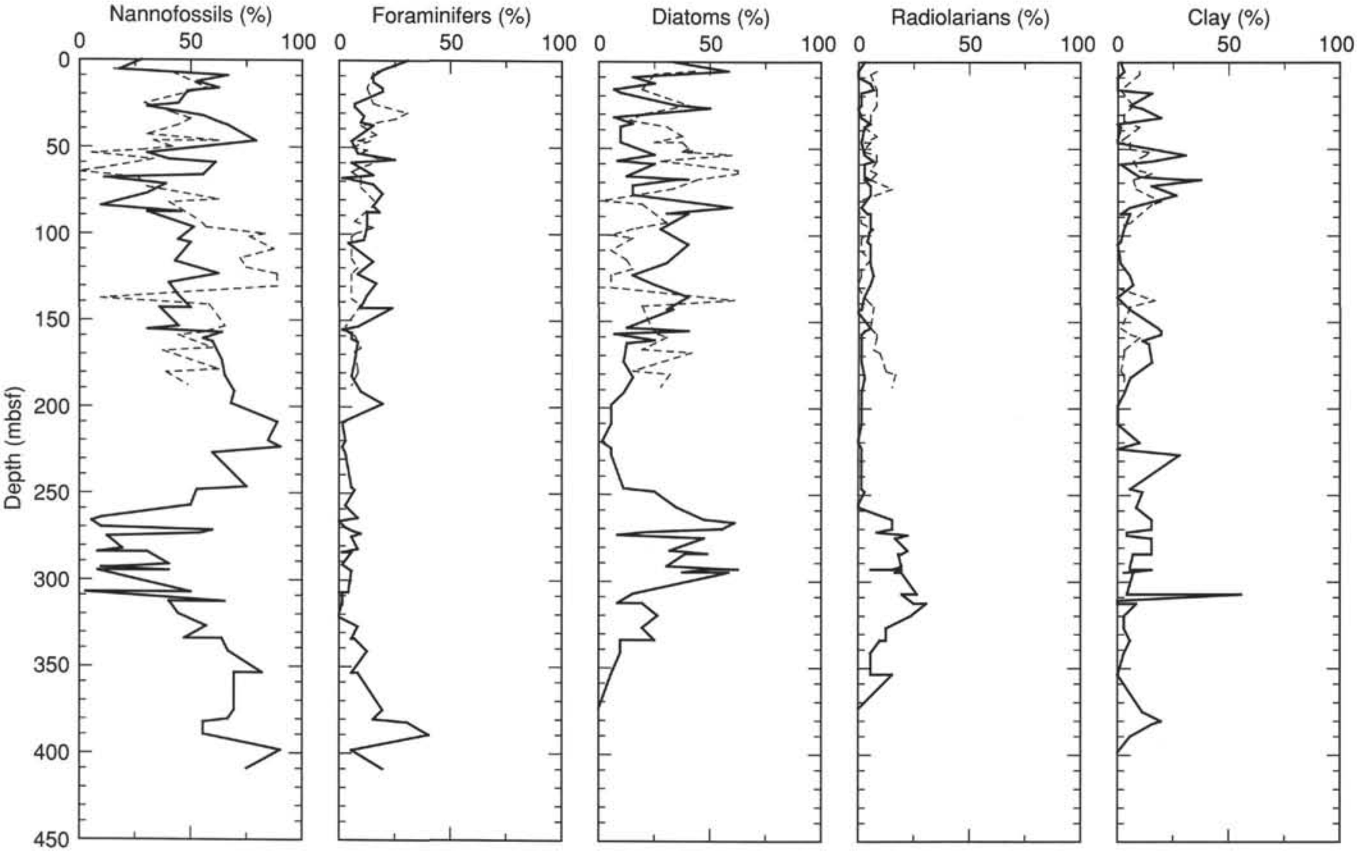

Figure 6. Summary of major component smear-slide data from Holes 846B (solid line) and 846C (dashed).

consistent occurrence of nannofossil ooze, in Section 138-846B-34X-4, 110 cm.

Unit II

Intervals:
Cores 138-846B-34X-4, 110 cm, through -45X-1, 63 cm
Depth: 317.0–419.2 mbsf, Hole 846B
Age: late Miocene to middle Miocene (about 10.6–16.5 Ma)

Unit II is composed mostly of nannofossil ooze. The upper portion (Subunit IIA) contains less than 20% biogenic silica (mostly diatoms). The lower part (Subunit IIB) is characterized by nannofossil chalk with foraminifers, with less than 5% of siliceous microfossils, but contains several cherty intervals. A thin sequence of metalliferous sediments occurs at the base of Subunit IIB, immediately above basalt basement.

Subunit IIA

Intervals:
Cores 138-846B-34X-4, 110 cm, through -40X-1, 20 cm
Depth: 317.0–370.5 mbsf, Hole 846B
Age: middle Miocene (about 10.6–14.1 Ma)

Subunit IIA is composed of nannofossil ooze and contains minor amounts of biogenic silica. Its top is marked by a rapid change from dark greenish gray (5GY 4/1) radiolarian diatom nannofossil ooze (in Subunit IB) to light greenish gray (5GY 7/1) nannofossil ooze with radiolarians and diatoms. This subunit has much higher average visible reflectance (30%–70%) and higher calcium carbonate content (60%–80%) than Subunit IB. The nannofossil and foraminifer content increases, and the radiolarian and diatom content decreases, downward. Carbonate nodules were recovered in Cores 138-846B-39X and -40X. The base of Subunit IIA is located at the base of a layer of chert nodules in Section 138-846B-40X-1, 20 cm. Below this point, biogenic silica is rare (generally less than 5% but usually < 1%).

Subunit IIB

Intervals:
Cores 138-846B-40X-1, 20 cm, through -45X-1, 63 cm
Depth: 370.5–419.2 mbsf, Hole 846B
Age: middle Miocene (14.1–16.5 Ma)

Subunit IIB contains 38.4 m of clayey foraminifer nannofossil chalk and foraminifer nannofossil chalk, with virtually no biogenic silica except for chert recovered in Cores 138-846B-41X and -43X. Recovery in this section was less than 50%. It is likely that more chert layers exist than were recovered, as suggested by the FMS log (see "Downhole Measurements" section, this chapter). Calcareous nannofossils dominate the sediment (usually >70% of the sediment), but foraminifers constitute between 10% and 50% of the total material. The ooze/chalk transition is gradual, but based on sonic velocity data it occurs at approximately 370 mbsf (in Core 138-846B-40X). Sonic velocity increases significantly between 350 and 380 mbsf in the geophysical logging string data. This boundary is probably the result of compaction processes, but coincides with the lithologic change of loss of biogenic silica and formation of chert.

Near its base, from 408.9 to 419.2 mbsf in Cores 138-846B-44X and -45X, Subunit IIB contains thin sequences of very light reddish-brown (5YR 6/4) metalliferous foraminifer nannofossil ooze. Lighter intervals in these sediments are buff colored. The nonbiogenic frac-

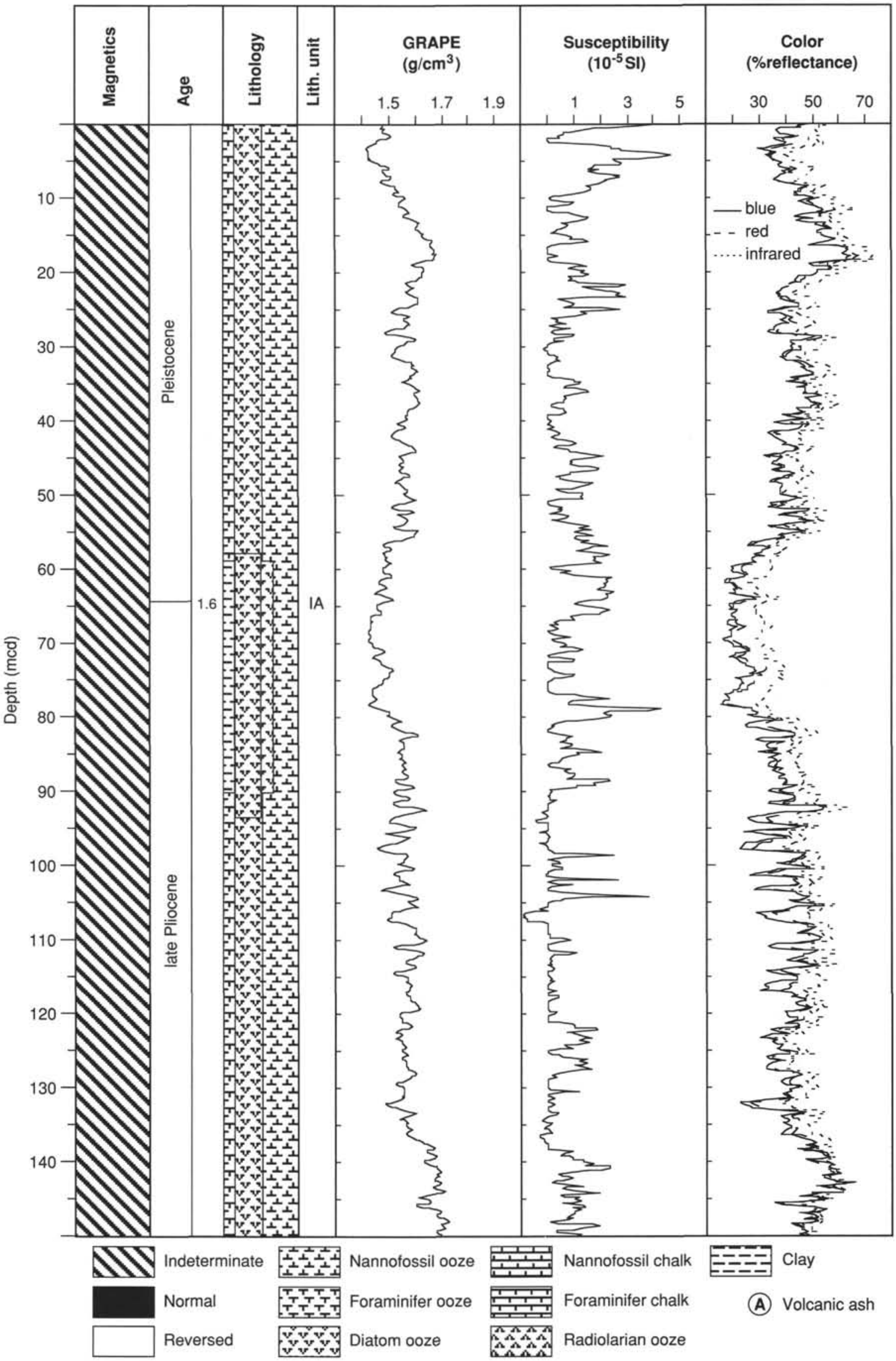

Figure 7. Composite summary of magnetics, age, graphic lithology, GRAPE, magnetic susceptibility, and color reflectance data for Site 846. Composite data consist of sections spliced together from the multiple holes drilled at the site. Data are shown plotted vs. meters composite depth (mcd), the new depth scale used when composite sections were constructed. The GRAPE, susceptibility, and color reflectance data have been smoothed using a 20-point Gaussian filter.

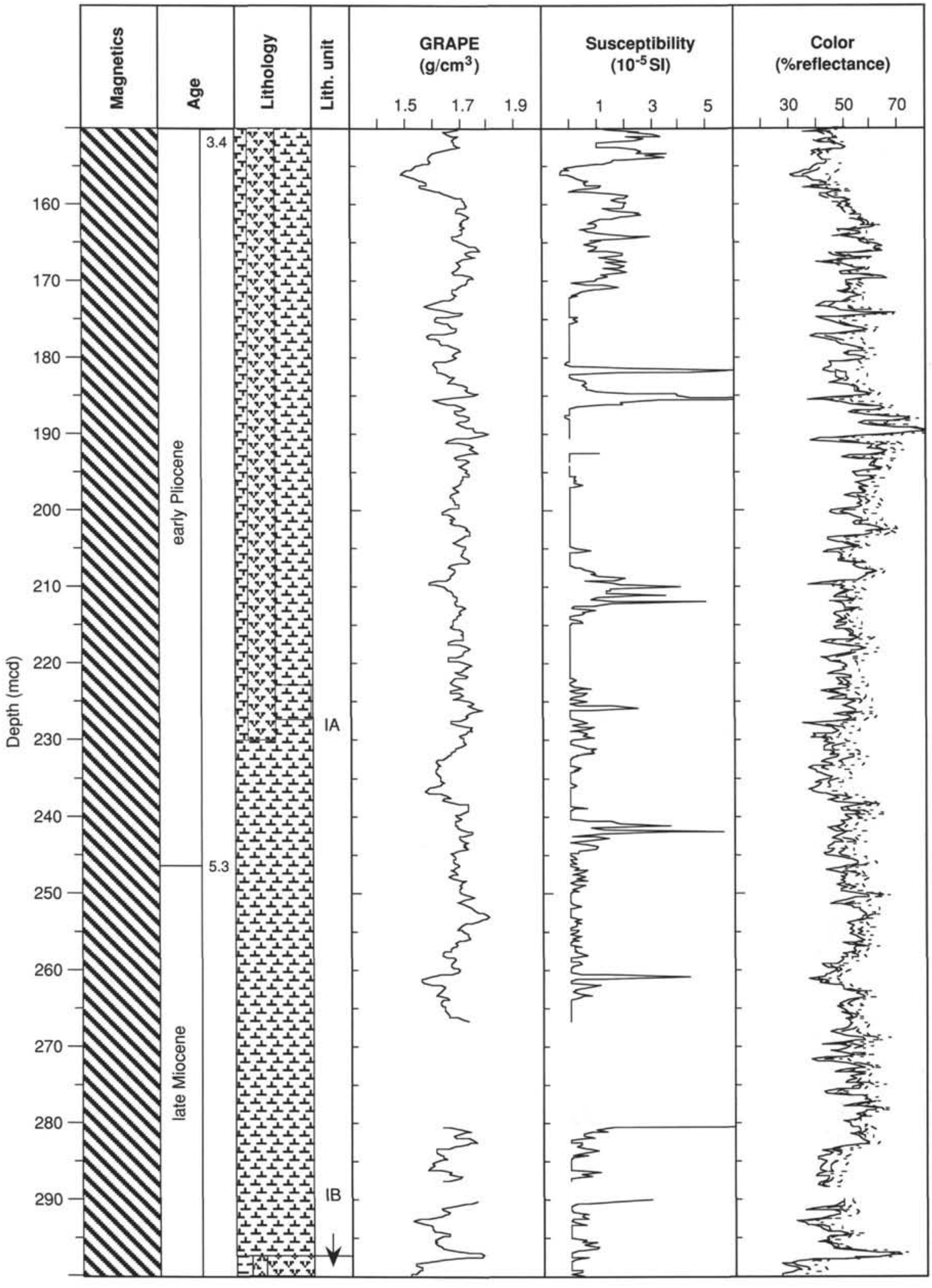

Figure 7 (continued).

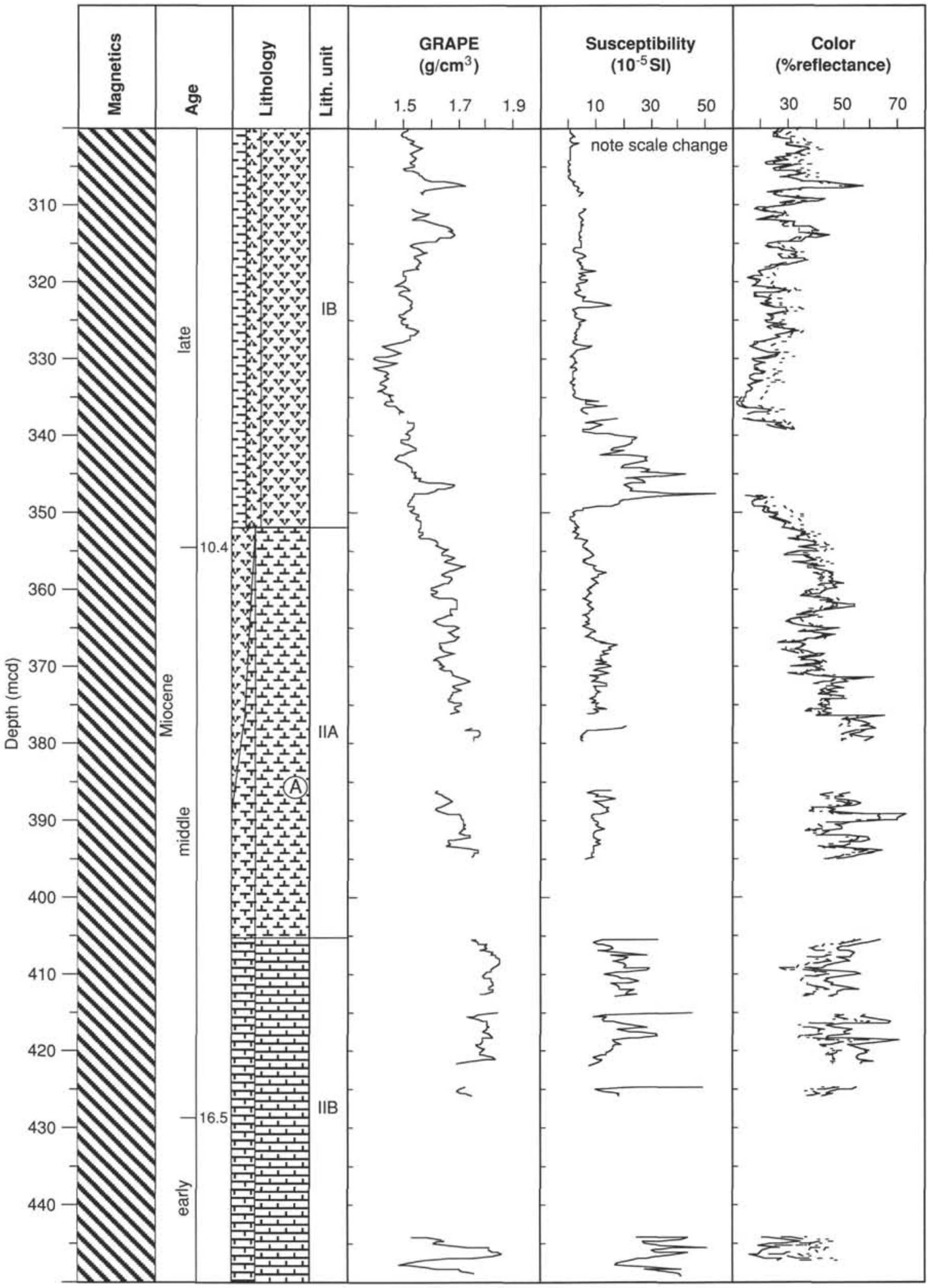

Figure 7 (continued).

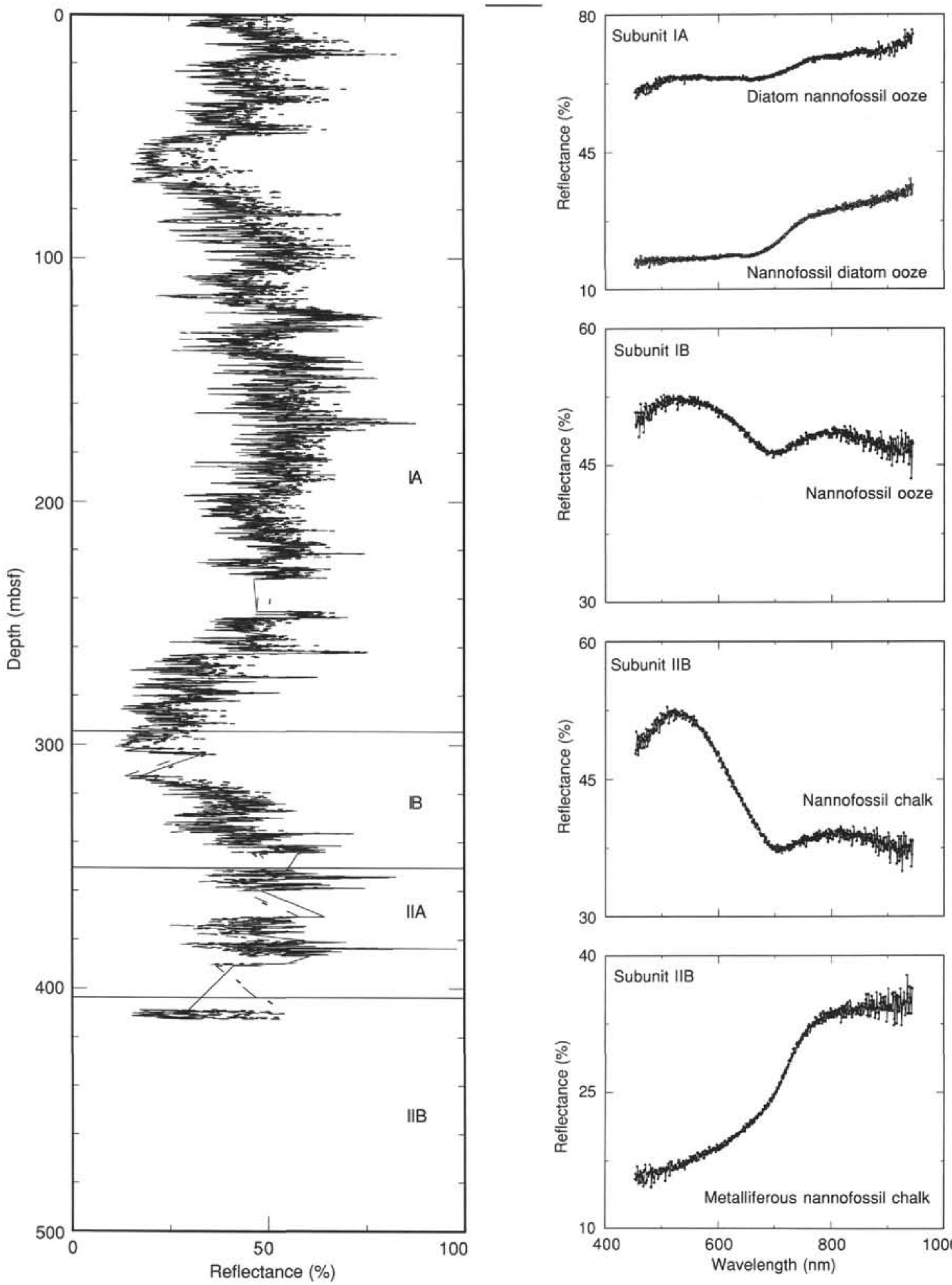

Figure 8. Summary of variations in color in Hole 846B. Downcore variations (left) are shown in three channels (blue, solid line; red, dashed line; near-infrared, dotted line). Examples of reflectance spectra characteristic of the major lithologic divisions are shown at right. Lithologic units shown in downcore plot.

tion of the sediment is rich in iron and contains hematite. There is one graded bed of fine-grained plagioclase sand within this interval. Metalliferous sediments occur above basaltic breccia in interval at Section 138-846B-45X-1, 0–63 cm. Below 419.2 mbsf, 1.5 m of basaltic breccia and basalt was recovered.

Color Reflectance Spectroscopy

The color reflectance spectroscopy data proved useful for characterizing lithologic variations on scales ranging from hundreds of meters to less than 1 m. Color reflectance in Hole 846B is summarized in Figure 8. Total reflectance averages about 50%, but varies widely. Relatively low reflectance was found in Subunit IA, from 48 to 70 mbsf, and in Subunit IB, from 265.2 to 317 mbsf. Both of these zones correspond to intervals of high biogenic silica content (up to 50% in smear slides, Fig. 6). The low-reflectance zones correspond to high porosity, low GRAPE density, and high water contents (see Physical Properties section, this chapter), which is typical in diatom- and radiolarian-rich lithologies.

Each lithology at this site has a distinct reflectance spectrum. Examples of the major sediment types are illustrated in Figure 8. In the top ~ 140 m of Unit I, the dark and light bands display similarly shaped spectra, with higher reflectance in the near-infrared bands than in the visible bands, but at very different average values. The nannofossil-diatom ooze layers yield lower (darker) reflectance values than the diatom nannofossil ooze layers. In Unit II, the spectra are quite different from those of the diatom-rich Unit I. Nannofossil ooze in Subunit IIA is more reflective in the visible bands than in the near- infrared. Maximum reflectance is from 500- to 600-nm wavelengths (roughly green to yellow). Minimum reflectance occurs near 700 nm (red). In Unit IIB, the nannofossil chalk accentuates the difference between visible and near-infrared reflection because of its low infrared reflectance. Biogenic silica is rare in the chalk. The metalliferous sediments above basalt basement have low reflectance in the shorter (blue) relative to the longer wavelengths (red and infrared). Near- infrared reflectance in these oxide-rich sediments (about 30% to 40%) is similar to that of the overlying nannofossil chalk and ooze at this site.

Decimeter- to Meter-Scale Variability

All of the lithologic units at Site 846 vary in composition and color on the scale of 0.1–10 m, but this scale of variability is difficult to capture on barrel sheets or in unit descriptions. Color banding on the decimeter to meter scale is illustrated in core photographs (Fig. 9, Sample 138-846B-6H-1, 30–150 cm). Although banding on this scale is apparent, details are commonly obscured by bioturbation. Digital color analyses plotted next to this core photograph demonstrate the types of signal detected by digital color reflectance. The banding is captured well, but the fine-scale details such as burrows are not seen, due to the 2-cm spot size detected by the reflectance spectrometer.

To illustrate variability on the scale of meters, color reflectance data is shown for 30 m of Hole 846B, from 25 to 55 mbsf, in Figure 10. This example, which shows strong variability on scales of 1–10 m, is typical of sediments throughout Site 846. Initial biostratigraphy suggests that this plot spans about 0.8 m.y., from roughly 0.7 to 1.5 Ma, and that sedimentation rates average 40 m/m.y. If this sedimentation rate is correct, then variations of 1–10 m wavelength would fall in the range of "Milankovitch" variations, from tens to hundreds of thousands of years.

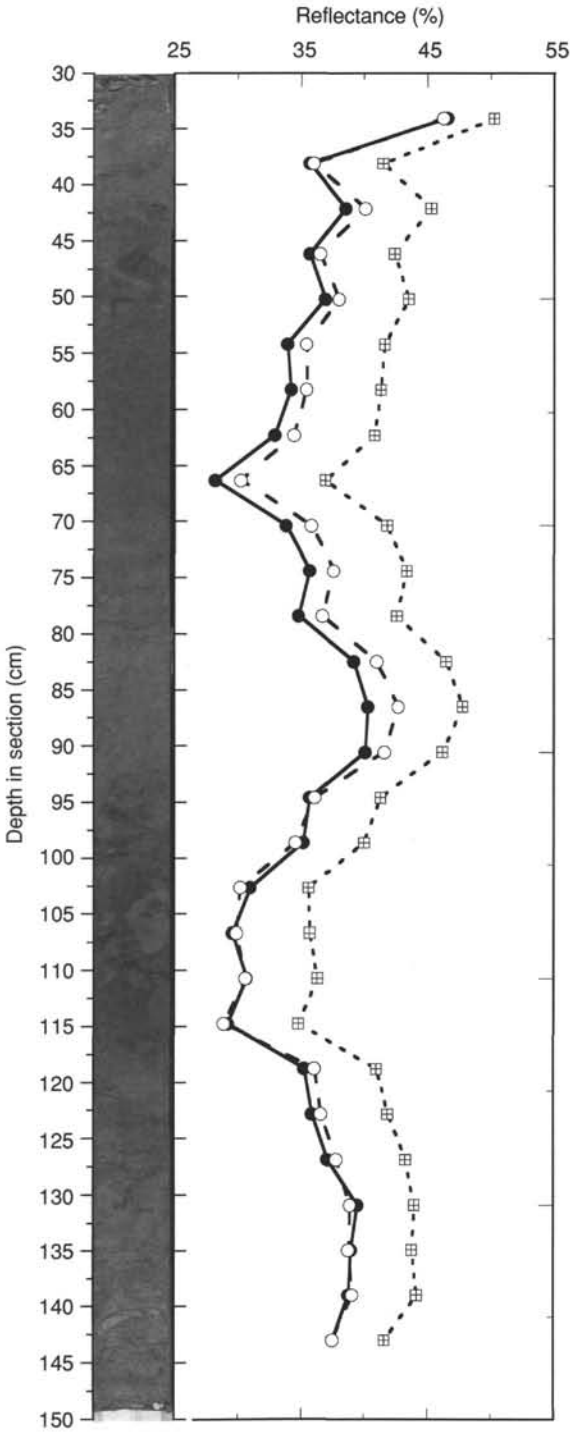

Figure 9. Variations in color (on a decimeter-scale) are shown in Section 138-846C-6H-1 at 30–150 cm. Percentage of reflectance data are shown for three bands. The 450–500 nm band (blue) has solid dots and line. The 650–700 nm (red) band has a dashed line and open circles. The 850–900 nm band has a dotted line and open squares. Light-to-dark banding is present visually in the section photograph (at right).

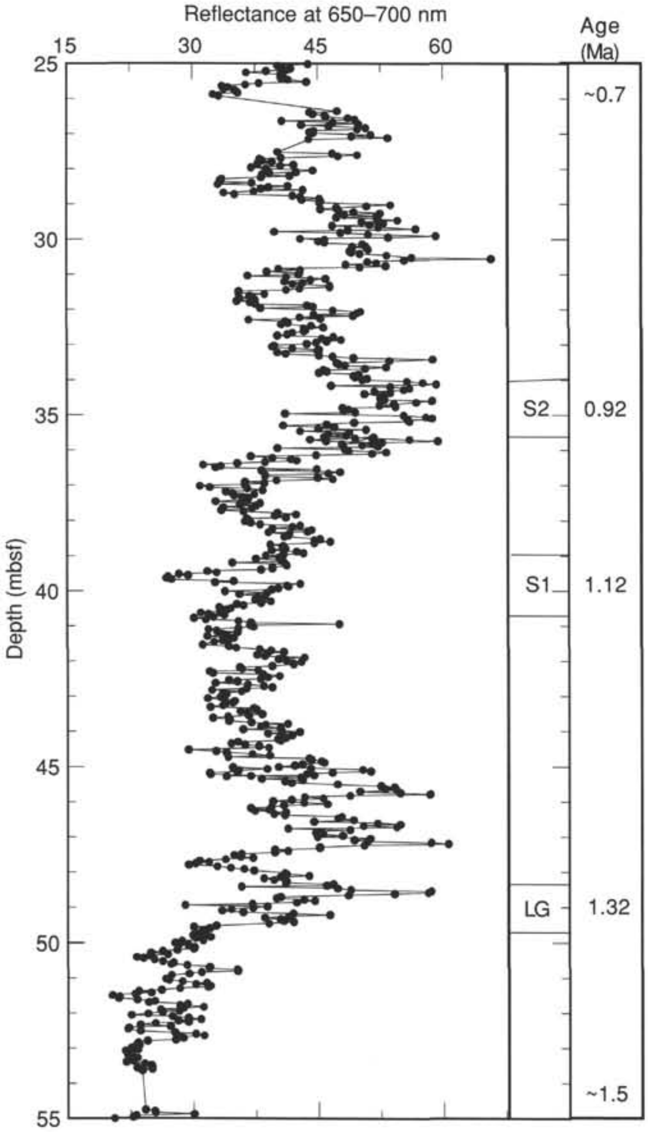

Figure 10. The downcore profile of the 650–700 nm (red) percentage of reflectance from 25 to 30 mbsf in Hole 846B demonstrates strong variability on a scale of meters. Biostratigraphic datums and ages are given on the right (see Biostratigraphy section, this chapter).

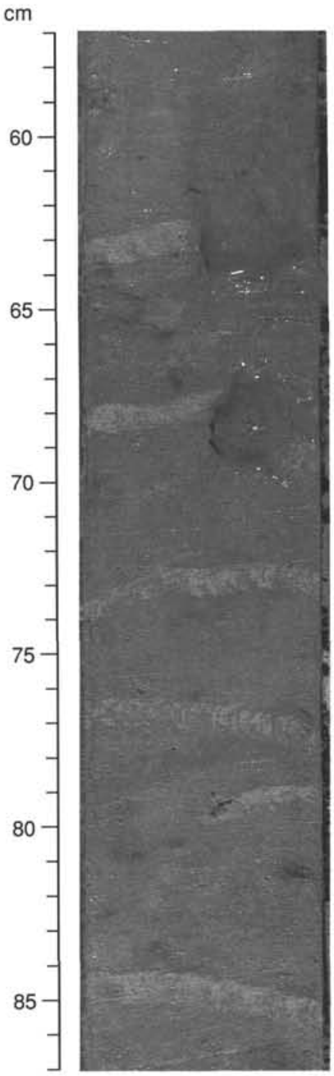

Figure 11. A stack of *Zoophycos* burrows, two of which have been cut by open burrows in Section 138-846D-1H-2 at 57–87 cm.

Trace Fossils

Bioturbation is common to abundant throughout the sediments recovered at Site 846. Some of the specific trace-fossil abundances are difficult to assess, however, particularly below Core 19 in Holes 846B, 846C, and 846D (about 180 mbsf) as a result of the poor quality of wire-cut core surfaces.

Within Subunit IA, three records of trace fossils were made separately for Holes 846B, 836C, and 846D. These three records are remarkably consistent and are particularly useful in highlighting the lateral persistence of burrowing at specific horizons. The intensity of bioturbation is generally high throughout the sediment column, but there is considerable variation in detail. Other than the upper 1 m, the top 10 m of each hole are highly bioturbated. Burrowing is slightly less intense between 10–30 mbsf but is intense once again from 40–50 mbsf. From around 50 to 150 mbsf in the alternating nannofossil ooze and diatom ooze sequences, bioturbation is generally intense in the paler nannofossil-rich lithologies and light to moderate within the darker olive color, diatom-rich layers.

Open burrows are present within the top 15 m of sediment. They are typically between 1–2 cm in diameter and truncate *Zoophycos* burrows (Fig. 11). Large vertical burrows, commonly surrounded by diagenetic halos, occur between 10–40 mbsf and are particularly common between 15–25 mbsf. These are up to 2.5 cm wide and up to 1.2 m long in some core sections (Fig. 12). These large burrows usually cut across other trace fossils, but in one case a solid burrow truncates the diagenetic halo of a large burrow (Fig. 13). There is an occasional association between the large burrows and open burrows (Fig. 14), suggesting that the same animal may be responsible for both.

Burrow fills may be either coarser or finer than the surrounding sediment. Lithologic differences between burrow fill and the surrounding material require that some sediment redistribution is occurring. In most cases, the redistribution is probably on the scale of centimeters to decimeters, but with the large vertical burrows, movement of material on the decimeters to meter scale is possible.

Solid burrows, *Planolites,* and less-common rind burrows appear throughout Subunit IA. *Skolithos* is present and locally common. *Zoophycos* burrows, typically 0.5–1.0 cm broad, are abundant to around 50 mbsf (Fig. 11). Diagenetic haloes are common and cross cut each other (Fig. 15). Below this, *Zoophycos* is common, particularly in, or adjacent to the darker, more diatom-rich layers, down to

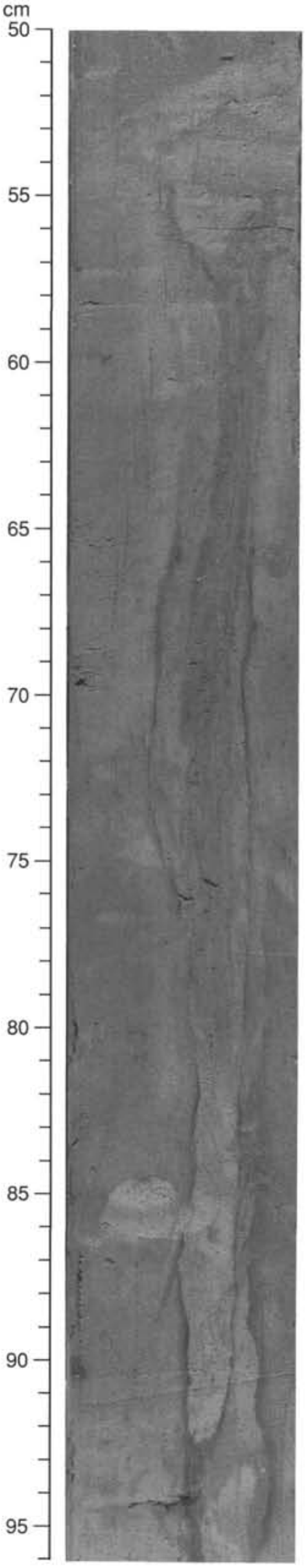

Figure 12. Large vertical burrow having a diagenetic halo in Section 138-846B-3H-1 at 50–96 cm.

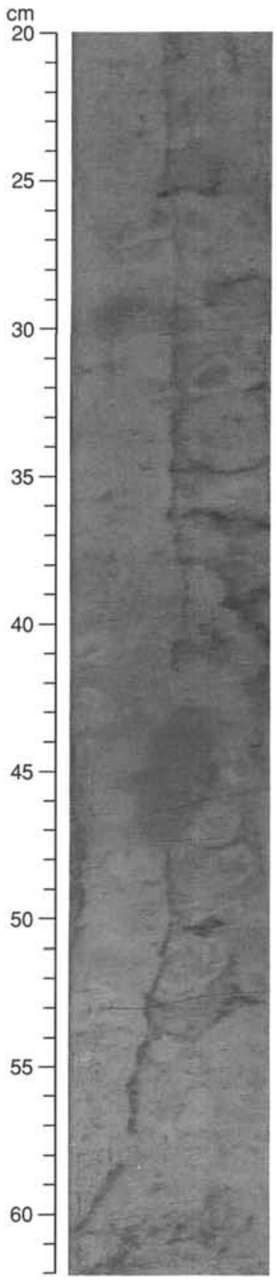

Figure 13. The halo around a vertical burrow cut by a solid burrow at Section 138-846D-4H-5 at 20–62 cm.

around 130 mbsf, below which it is observed more rarely. Significantly, *Zoophycos* often was observed where the intensity of burrowing is low, such as within the darker, diatom-rich layers. *Chondrites* is present to abundant and sometimes pervasive (Fig. 16), such as in Cores 138-846B-15H, 16H; -846C-15H, -16H, -17H, -19H, -20H; -846D-15H and 19H. *Chondrites* was often observed within solid burrows or *Planolites*.

In Subunit IA from 190 to 263 mbsf, recognition of trace fossils was hampered by the poor core surfaces. In some intervals, burrow mottling is pervasive, but few specific trace fossils are regularly identified. Between 200 and 260 mbsf, solid burrows and *Planolites* are common, and a thin (<3 mm) *Zoophycos* form is present. From 260 to 295 mbsf, solid burrows, *Planolites*, and *Chondrites* are common, and *Zoophycos* is rare.

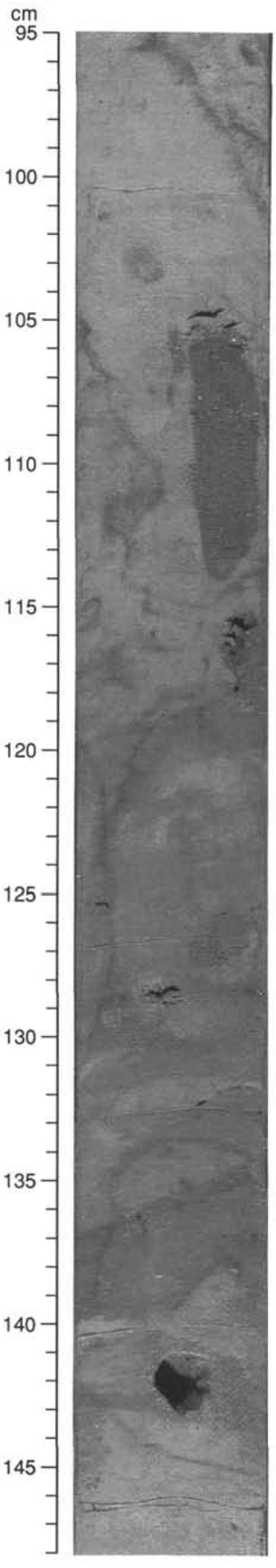

Figure 14. A large burrow associated with an open burrow in Section 138-846D-1H-4 at 95–148 cm.

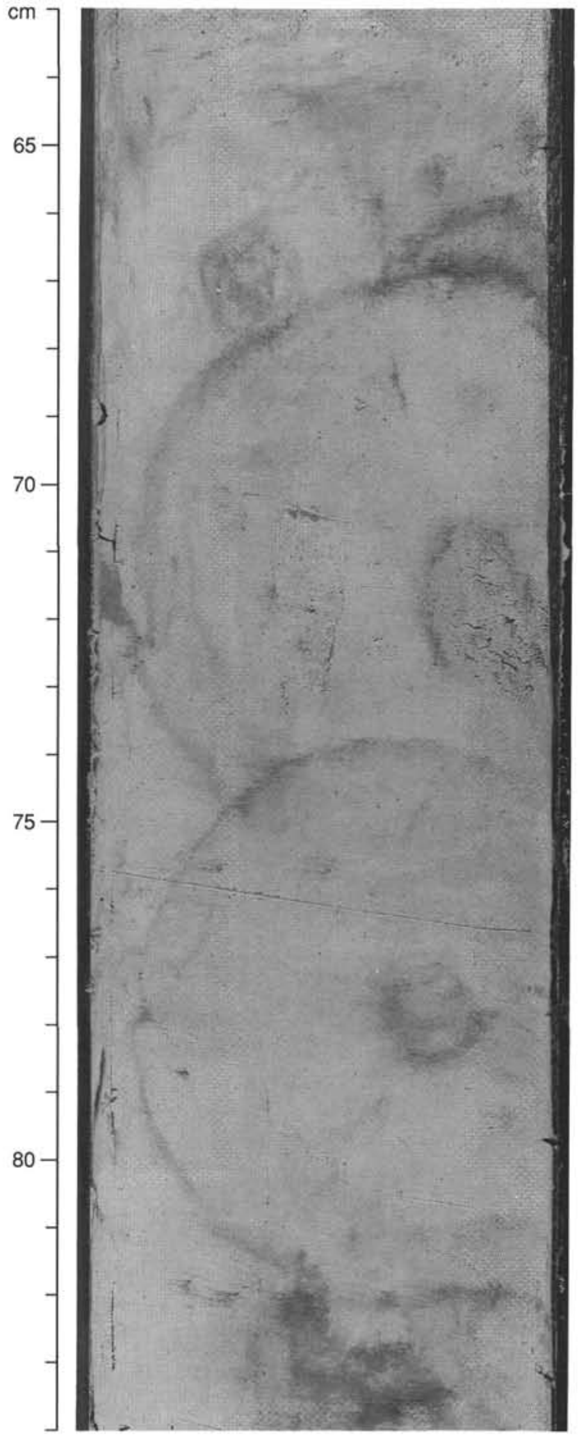

Figure 15. Solid burrows with truncating halos in Section 138-846B-15H-2 at 63–84 cm.

Burrowing in Subunit IB was most readily identified when it was associated with color contrast between alternating paler carbonate and darker siliceous layers (Fig. 17) and by variegation and mottling in the most siliceous-rich intervals. Solid burrows and *Planolites* are abundant throughout. *Chondrites* is abundant in Cores 138-846B-28X through-31X, but was not recognized below this. *Zoophycos* and

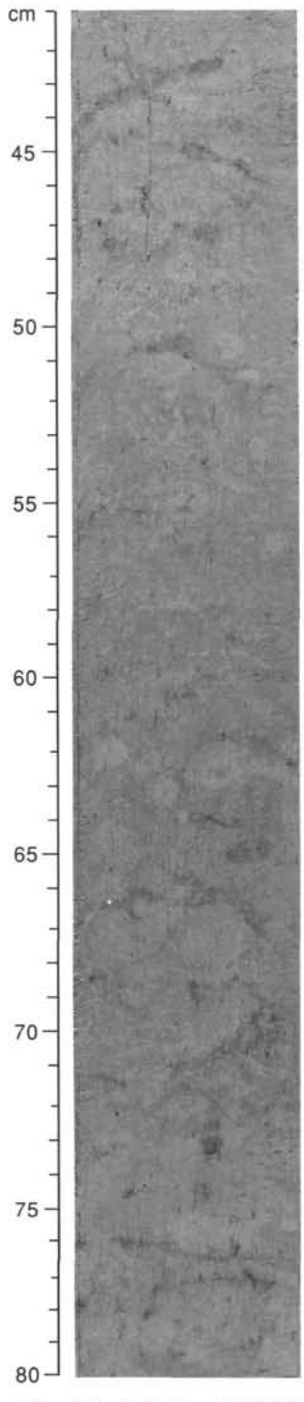

Figure 16. Pervasive *Chondrites* in Section 138-846C-19H-6 at 41–80 cm.

Skolithos were observed seldom. The surfaces of Cores 138-846B-32X through -34X are indistinct, although both solid burrows and *Planolites* were recognized. Few halos around burrows were identified in this subunit.

Within the nannofossil oozes of Unit II, solid burrows, *Planolites, and Chondrites* are common. A much thinner (about 3 mm) variety of *Zoophycos* and *Skolithos* was more rarely observed.

Despite the varying quality of the core surfaces for description at Site 846, patterns in the occurrence of trace fossils are apparent.

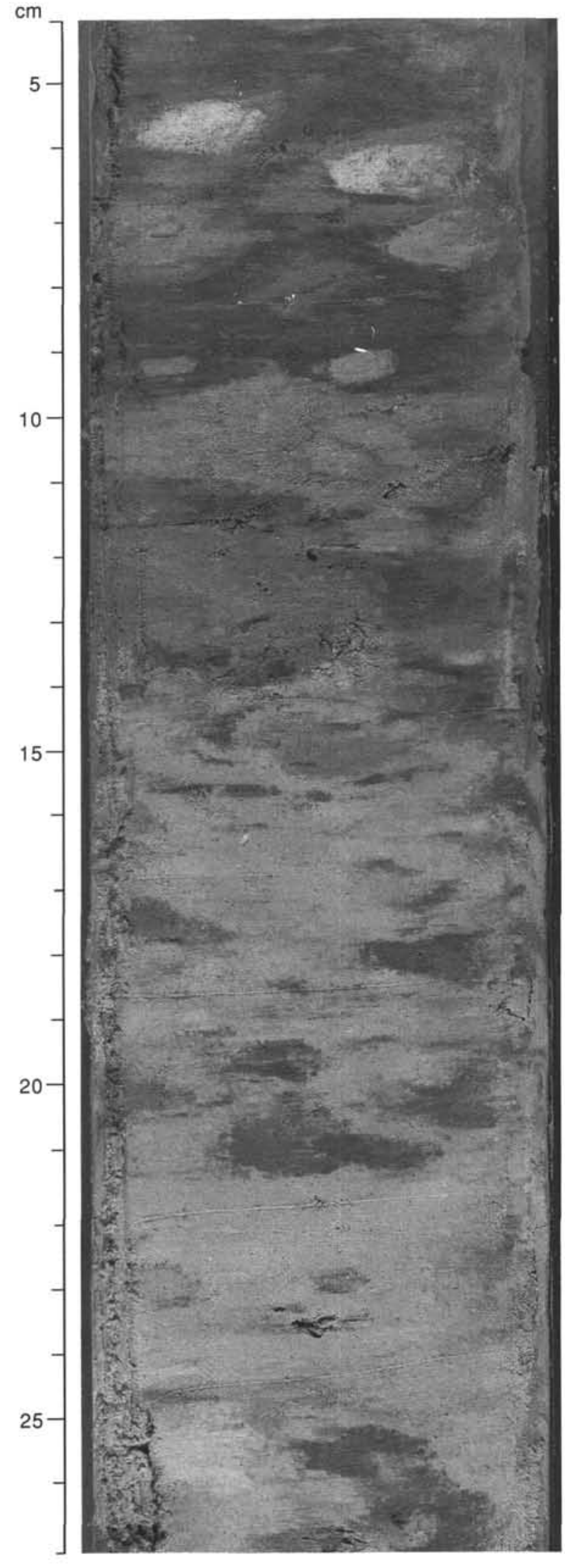

Figure 17. Highly bioturbated contact between a darker (more siliceous) and paler (more carbonate-rich) interval in Subunit IIB in Section 138-846B-29X-4 at 4–27 cm.

Zoophycos appears most strongly associated with diatom-rich intervals and its greatest relative abundance is in the most organic-carbon-rich upper part of the sediment column (See "Organic Geochemistry" section, this chapter). *Chondrites* appears most strongly developed within the carbonate-rich units and is seldom seen in association with *Zoophycos*.

Diagenetic Features

Evidence for diagenesis of organic carbon, biogenic opal, and calcium carbonate is common at Site 846. Most of the sediment column has experienced sulfate-reduction zone organic diagenesis. Disseminated pyrite, pyritized burrows, and pyrite-rich dark-gray color bands and "Liesegang" structures are common (Fig. 15). When opened, the cores degassed hydrogen sulfide and methane (see Organic Geochemistry section, this chapter).

The most obvious evidence for silica diagenesis is the presence of chert nodules in intervals at 138-846B-40X-1, 0–20 cm, -41X-1, 0–5 cm, and 130 cm, and -43X-1, 0–5 cm. Below the first of these chert zones, biogenic silica is consistently less than 5% of the recovered sediment. Diatoms and radiolarians usually are present only in trace quantities, and show signs of dissolution. It is possible that additional chert layers exist in Subunit IIB, below 370.5 mbsf, but recovery was low. Pore-water geochemistry demonstrates anomalously low dissolved silica below 370 mbsf, consistent with mobilization and reprecipitation of silica as chert in this interval.

The presence of chalk below 370 mbsf is not accompanied by strong evidence for recrystallization. Chalk first appears at the same depth as the loss of biogenic silica. It is unknown at present whether the depth of the nannofossil ooze to chalk transition at this site is in part controlled by the opal abundance, or if this association is fortuitous. Pore-water data does suggest significant carbonate dissolution, however, as strontium values are elevated. Highest strontium values occur between 150 and 250 mbsf (see Inorganic Geochemistry section, this chapter).

Summary of Lithology

Calcium carbonate is present throughout most of the sedimentary column, but its abundance is highly variable on the scale of meters. At an average sedimentation rate of 40 m/m.y., this corresponds to timescales of tens to hundreds of thousands of years, within the range of Milankovitch variability. Clay input is low relative to biogenic fluxes at this site. The dominant sediment component at Site 846 alternates between biogenic silica (mostly diatoms) and calcium carbonate (mostly nannofossils). Opaline sediments, dominated by diatom ooze, are more common in the younger part of the sedimentary column (Pleistocene to late Miocene) than in the older material (late Miocene to middle Miocene). Especially high concentrations of diatom ooze occur in the lower Pleistocene to upper Pliocene section (50–80 mbsf), and along with anomalously high concentrations of radiolarians in the late Miocene (262.7–317 mbsf). Minima in opal content (and maxima in calcium carbonate content) occur in the late Miocene (200–262.7 mbsf) and in the early to middle Miocene (317–408.9 mbsf). The low biogenic silica content in this older interval may reflect silica diagenesis and chert formation, rather than lack of input. The lower ~39 m of the sediment column is dominated by nannofossils and has been compacted to chalk. A thin sequence of metalliferous sediment occurs above basalt basement.

BIOSTRATIGRAPHY

The sedimentary sequence recovered from the four holes cored at Site 846 consists of a 420-m-thick interval of Quaternary to lower Miocene sediments. The section includes a continuous 300-m-thick, expanded sequence from the Pleistocene through the upper half of the Miocene (approximate equivalent to the last 7.1 m.y.) above a 120-m-thick more condensed upper to lower Miocene interval. The base of the sedimentary sequence is assigned to the lower Miocene calcareous nannofossil Zone CN3, indicating an age between 16.0 and 18.40 Ma.

Well-preserved radiolarians and diatoms are abundant throughout the Pleistocene, Pliocene, and upper Miocene. In the middle Miocene below Core 846B-32X (302.80 mbsf), diatoms and radiolarians are moderately-well to poorly preserved and show signs of dissolution and reprecipitation. Below Core 846B-38X (360.60 mbsf) the lower middle and lower Miocene sediments are barren of siliceous microfossils. Calcareous nannofossils are generally abundant throughout the section, with good to moderate preservation except in the lowermost upper Miocene (Cores 846B-32X and -33X; 293.10-312.40 mbsf) in which they are rare and poorly preserved. Planktonic foraminifers are common to abundant in the Pleistocene and Pliocene, being moderately-well to poorly preserved. Their preservation deteriorates downward throughout the sedimentary sequence. In the Miocene planktonic foraminifers are rare to common and poorly preserved.

A well-constrained biostratigraphy is provided by the various microfossil groups (Tables 3 to 6, Fig. 18). The expanded Pleistocene through uppermost Miocene sequence, which accumulated at a rate of approximately 45 m/m.y., yielded a detailed record of calcareous nannofossil, radiolarian, and diatom biostratigraphic events. The record of planktonic foraminifer biostratigraphic events is limited because a number of marker species are rare or absent due to poor preservation.

A marked change in sedimentation rate occurs at about 7.1 Ma (283 mbsf in Hole 846B). The interval between about 283 and 312 mbsf (Cores 846B-31X through -33X), which accumulated at an average rate of about 15 m/m.y., spans the middle/upper Miocene boundary. In this interval of very low calcium carbonate content, the abundance and preservation of calcareous plankton significantly decreases, precluding precise zonal assignment. Reworking in this interval was observed in several microfossil groups, and the occurrence of short (of the order of <0.5 m.y.) hiatuses is not excluded, although diatoms show a regular sequence of stratigraphic events. Below this interval the middle Miocene biostratigraphic sequence appears to be continuous and is well constrained by siliceous microfossils and calcareous nannofossils down to Core 846B-38X (360.60 mbsf). Below that level the lowermost middle Miocene and uppermost lower Miocene biostratigraphic sequence is constrained only by calcareous nannofossils.

Epoch boundaries are best approximated in Hole 846B as follows:

Boundary	Hole	Depth (mbsf)	Depths (mcd)	Event
Pleistocene/Pliocene	846B	53.1	59.6	B *Gephyrocapsa oceanica* s.l.
late/early Pliocene	846B	131.1	150.8	T *Reticulofenestra pseudoumbilicus*
Pliocene/Miocene	846B	194.0	220.95	T *Discoaster quinqueramus*
late Miocene/middle	846B	327.29	362.39	T *Craspedodiscus coscinodiscus*
middle/early Miocene	846B	390.39	425.49	T *Helicosphaera ampliaperta*

Note: B = begin, T = terminate.

Planktonic foraminifers allow the identification of paleoceanographic events in the Pleistocene-Pliocene section. In this interval the planktonic foraminifer fauna yields a mixture of warm-water assemblages and cold-water species. The latter have spikes of abundance at various stratigraphic horizons, probably reflecting fluctuations in the influence of the cool-water Peru Current.

Calcareous Nannofossils

Calcareous nannofossils recovered at Site 846 represent a stratigraphic sequence from the upper Pleistocene (Zones CN15 and CN14b of Okada and Bukry, 1980, and Zones NN21 and NN20 of Martini, 1971) through the lower Miocene (Zones CN3 and NN4).

Table 3. Sample and depth constraints of calcareous nannofossil events for Hole 846B.

	Hole 846B			Hole 846C		
Event	Core, section, interval, (cm)	Depth (mbsf)	Depth (mcd)	Core, section, interval (cm)	Depth (mbsf)	Depth (mcd)
T *Pseudoemiliania lacunosa*	2H-CC–3H-1, 42	16.89–16.92	17.49–18.97	2H-CC–3H-CC	12.20–21.84	12.53–21.32
B *Gephyrocapsa* sp. 3	4H-6, 45 -4H-7, 54	33.95–35.34	37.10–38.49	2H-CC–3H-CC	12.20–21.84	12.53–21.32
T >5.5 µm *Gephyrocapsa* spp.	5H-3, 40–5H-4, 40	38.90–40.40	44.10–45.60			
B >5.5 µm *Gephyrocapsa* spp.	6H-3, 39–6h-4, 39	48.39–49.89	54.89–56.39			
T *Calcidiscus macintyrei*	6H-5, 40–6H-6, 40	51.40–52.90	57.90–59.40			
B *Gephyrocapsa oceanica* s.l.	6H-6, 40–6-CC	52.90–53.94	59.40–60.44	5H-CC–6H-CC	50.69–58.69	54.74–65.50
T *Discoaster brouweri*	8H-3, 43 – 8H-3, 140	67.43–68.40	77.13–78.10	7H-CC–8H-CC	69.71–78.36	76.61–85.96
T *Discoaster surculus*	10H-2, 60–10H-3, 60	85.10–89.60	97.65–102.15			
T *Discoaster tamalis*	12H-2, 60–12H-3, 60	104.10–105.60	118.90–120.4			
T *Reticulofenestra pseudoumbilicus*	14H-CC–15H-1, 60	130.78–131.10	147.93–160.30	13H-CC–14H-CC	126.25–135.17	142.75–153.57
B *Discoaster asymmetricus*	15H-CC–16H-1, 60	140.62–140.60	160.32–160.80			
T *Amaurolithus primus*	17H-1, 50–17H-2, 50	150.00–151.50	171.85–173.35			
B *Ceratolithus rugosus*	19H-3, 40–19H-4, 40	171.90–173.40	195.70–197.20			
B *Ceratolithus acutus*	20H-3, 50– 20H-4, 50	181.50–182.5	207.10–208.1			
T *Discoaster quinqueramus*	1H-4, 50–21H-5, 50	191.50–194.00	218.45–220.95			
B *Amaurolithus primus*	25X-CC–26X-CC	232.12–235.61	260.80–270.70			
B *Discoaser berggreni*	29X-5, 60–29X-6, 60	270.80–272.30	305.90–307.40			
T *Discoaster hamatus*	32X-5, 60–32X-6, 60	299.70–301.20	334.80–336.30			
T *Coccolithus miopelagicus*	33X-4, 60–33X-5, 60	307.90–309.40	343.00–344.50			
B *Discoaster hamatus*	33X-4, 60–33X-5, 60	307.90–309.4	343.00–344.50			
T *Cyclicargolithus floridanus*	38X-5, 46–38X-6, 50	357.46–359.00	392.56–394.10			
T *Sphenolithus heteromorphus*	38X-CC–40X-1, 40	360.20–370.70	395.30–405.80			
B *Reticulofenestra pseudoumbilicus*	40X-3, 100–40X-4, 40	374.30–374.90	409.40–410.00			
T *Helicosphaera ampliaperta*	41X-CC–42X-1, 79	387.11–390.39	422.21–425.49			
B *Discoaster signus*	41X-CC–42X-1, 79	387.11–390.39	422.21–425.49			

Note: T = top; B = bottom.

Table 4. Sample and depth constraints of planktonic foraminifer events in Hole 846B.

	Hole 846B		
Event	Core	Depth (mbsf)	Depth (mcd)
T Globorotalia tosaensis	2H-CC–3H-CC	16.5–26.0	17.49–28.22
T Globorotalia limbata	7H-CC–8H-CC	64.0–73.5	72.56–83.66
T Dentoglobigerina altispira	12H-CC–13H-CC	111.5–121.0	126.60–138.10
T Sphaeroidinellopsis spp.	13H-CC–14H-CC	121.0–130.5	138.10–147.93
sinistral to dextral coiling change in *Pulleniatina*	14H-CC–15H-CC	130.5–140.0	147.93–160.32
B Globorotalia tumida	20H-CC–21H-CC	187.0–197.0	213.45–224.63

Note: T = top; B = bottom.

They are generally abundant throughout the sequence except in the Miocene interval encompassing Cores 138-846B-32X and -33X, in which their abundance has been reduced. Preservation is generally good to moderate. The nannofossil events recognized at Site 846 are reported in Table 3.

The Pleistocene interval includes Cores 138-846B-1H to -6H, 138-846C-1H to -5H, and 138-846D-1H to -6H. In this interval the nannofossils are abundant and well preserved, and the assemblage is characterized by *Pseudoemiliania lacunosa, helicoliths,* and different morphotypes of the genus *Gephyrocapsa.* The moderate etching, which affects some *placoliths,* does not prevent the identification of most of the marker species. The last occurrence of *P. lacunosa* is recorded between Samples 138-846B-2H-CC and -3H-1, 42 cm, 138-846C-2H-CC and -3H-CC, and 138-846D-2H-2, 40 cm, and -2H-2, 120 cm.

Other biostratigraphically useful lower Pleistocene events include: the first occurrence of *Gephyrocapsa* sp.3, the last and the first occurrences of *Gephyrocapsa* spp. larger than 5.5 µm in size, the last occurrence of *Calcidiscus macintyrei,* and the first occurrence of *Gephyrocapsa oceanica* s.l., (Rio et al., in press). The latter event, which approximates the Pleistocene/Pliocene boundary (Rio et al., in press), occurs between Samples 138-846B-6H-6, 40 cm, and -6H-CC, between 138-846C-5H-CC and -6H-CC, and between 138-846D-6H-2, 150 cm, and -6H-3, 50 cm.

The Pliocene section corresponds to Cores 138-846B-7H through -21H, 138-846C-6H through -20H, and 138-846D-6H through -20H. Nannofossil assemblages consist mainly of reticulofenestrids, helicoliths, sphenoliths, ceratolithids, and discoasterids. Throughout the Pliocene and the upper Miocene intervals discoasterids vary in abundance, fluctuating from assemblages with abundant and diversified discoasterids to assemblages almost void of discoasterid species. Most of the Pliocene datums, however, were recognized (see Table 3). The exception is the last occurrence of *Discoaster pentaradiatus,* a species that has a rare and sporadic occurrence throughout this interval. The last occurrence of *Discoaster quinqueramus* (top of Zone CN9 and NN11) occurs between Samples 138-846B-21H-4, 50 cm, and -21H-5, 50 cm. *Discoaster quinqueramus* and other Miocene discoasterids, such as *Discoaster berggreni, Discoaster neohamatus,* and *Discoaster hamatus,* also are scattered and are absent in some intervals, making the recognition of their first or last occurrences difficult.

In the Miocene interval, some placoliths are slightly dissolved, while discoasterids have moderate overgrowths. The assemblages are characterized by the presence of helicoliths, sphenoliths, placoliths, mainly *Reticulofenestra* spp. and *Coccolithus* spp., ceratolithids in the upper Miocene, and discoasterids in the middle Miocene. The first occurrence of *Amaurolithus* spp., marking the CN9a/CN9b zonal boundary, was placed between Samples 138-846B-25X-CC and -26X-CC, and in Section 138-846D-26X, 120 cm. The CN8/CN9a (NN10/NN11) zonal boundary is placed at the first occurrence of *D. berggreni* in Section 138-846B-29X-5, 60 cm.

The interval from Sections 138-846B-32X-6, 60 cm, through -33X-4, 60 cm, is placed in Zone CN7 (NN9), which corresponds to the range of *D. hamatus.* The last occurrence of *Coccolithus miopelagicus,* which approximates the upper boundary of Zone CN6 (NN8), occurs in Section 138-846B-33X-5, 60 cm. The event that corresponds to the lower boundary of this zone, the first occurrence of *Catinaster coalitus,* was not clearly identified here because of the scarcity of this species. Only rare scattered specimens allow tentative placement of Cores 138-846B-33X and -34X in Zone CN6 (NN8).

The assemblage that characterizes Zone CN5 (NN7–NN6) was found in the interval from Cores 138-846B-35X through -38X. In this interval discoasterids are represented by six-ray forms, such as *Discoaster bollii, Discoaster musicus,* and rare *Discoaster brouweri. Discoaster kugleri* is present in Core 138-846B-37X, but does not have a continuous or consistent occurrence. *Cyclicargolithus floridanus* last occurs in Section 138-846B-38X-6, 50 cm. The last occurrence of *Sphenolithus heteromorphus* (top of Zones CN4 and NN5) was recorded in Section 138-846B-40X-1, 40 cm, placing the interval from Section 138-846B-40X-1 at 40 cm, through Sample 138-846B-41X-CC in Zone CN4 (NN5). Near the last occurrence of *S. heteromorphus,* the

Table 5. Sample and depth constraints of radiolarian events for Site 846.

	Hole 846B			Hole 846C			Hole 846D		
Event	Core, section	Depth (mbsf)	Depth (mcd)	Core, section, interval (cm)	Depth (mbsf)	Depth (mcd)	Core, section, interval (cm)	Depth (mbsf)	Depth (mcd)
B *Buccinosphaera invaginata*									
T *Stylatractus universus*	2H-5–2H-CC	14.10–16.39	14.70–17.49						
B *Collosphaera tuberosa*	2H-5–2H-CC	14.10–16.39	14.70–17.49						
T *Lamprocyrtis neoheteroporos*	4H-5–4H-CC	33.10–36.06	36.25–39.21						
T *Anthocyrtidium angulare*	4H-CC–5H-3	36.06–39.60	39.21–44.28	3H-CC–4H-CC	31.45–41.09	34.45–44.29			
T *Theocorythium vetulum*	5H-3–5H-5	39.60–42.60	44.80–47.8				3H-CC–4H-CC	32.93–42.69	34.63–46.29
B *Lamprocyrtis nigriniae*	5H-CC–6H-3	45.54–49.10	50.74–54.74	4H-CC–5H-CC	41.09–50.69				
B *Theocorythium trachelium*	6H-3–6H-5	49.10–52.10	54.74–58.60			44.29–54.74	4H-CC–5H-CC	42.69–52.10	46.29–57.70
B *Pterocorys minythorax*	5H-CC–6H-3	45.54–49.10	54.74–54.74						
B *Anthocyrtidium angulare*	7H-CC–8H-3	64.26–68.10	72.56–77.80	7H-CC–8H-CC	69.71–78.36	76.61–85.96			
T *Pterocanium prismatium*	6H-CC–7H-3	53.94–58.60	60.44–66.90	5H-CC–6H-CC	50.69–58.64	54.74–65.59	5H-CC–6H-CC	52.10–61.38	57.70–66.78
T *Lamprocyrtis heteroporos*	8H-3–8H-5	68.10–71.10	77.80–80.80						
T *Anthocyrtidium jenghisi*	9H-3–9H-5	77.60–80.60	87.75–90.75						
B *Theocalyptra davisiana*	11H-3–11H-5	96.64–99.65	110.14–111.5	9H-CC–10H-CC	87.63–97.65	98.88–111.60			
T *Stichocorys peregrina*	11H-3–11H-5	96.64–99.65	110.14–111.5	9H-CC–10H-CC	87.63–97.65	98.88–111.60			
T *Anthocyrtidium pliocenica*	13H-3–13H-5	115.60–118.65	132.05–135.10						
B *Lamprocyrtis neoheteroporos*	13H-5–13H-CC	118.65–121.65	135.10–138.10						
T *Phormostichoartus fistula*	12H-CC–13H-3	111.80–115.60	126.60–132.05				12H-CC–13H-CC	115.91–125.89	129.41–140.49
T *Lychnodictyum audax*	15H-3–15H-5	134.65–137.65	154.35–157.35						
T *Phormostichoartus doliolum*	16H-3–16H-5	144.15–147.15	164.35–167.35						
T *Didymocyrtis penultima*	15H-CC–16H-3	140.12–144.15	159.85–164.35	14H-CC–15H-CC	135.17–145.22	153.57–163.72	14H-CC–15H-CC	134.31–144.9	151.11–162.90
B *Pterocanium prismatium*	17H-CC–18-3	159.65–163.15	180.93–185.00				16H-CC–17H-CC	154.31–163.61	174.31–184.41
T *Solenosphaera omnitubus*	20H-CC–21-3	187.85–191.65	213.45–218.60				19X-CC–20X-CC	172.80–181.80	205.34–216.89
T *Siphostichartus corona*	20H-CC–21-3	187.85–191.65	213.45–218.60				19X-CC–20X-CC	172.80	205.34–216.89
T *Acrobotrys tritubus*	24X-CC–26X-CC	225.78–235.70	261.18–270.71				23X-CC–24X-CC	220.16–230.06	254.01–263.41
T *Stichocorys johnsoni*	26X-CC–27X-3	235.70–249.30	270.71–284.40						
Stichocorys delmontensis > *S. peregrina*	25X-CC–26X-CC	232.12–235.70	267.22–270.71				25X-CC–26-2	239.86–242.4	273.66–276.20
T *Calocycletta caepa*	25X-CC–26X-CC	232.12–235.70	267.22–270.71				25X-CC–26-2	239.86–242.4	273.66–276.20
B *Solenosphaera omnitubus*	27X-CC–28X-3	253.56–259.00	288.66–294.10						
T *Diartus hughesi*	28X-CC–29X-3	264.87–268.30	299.97–303.40						
B *Acrobotrys tritubus*	28X-CC–29X-3	264.87–268.30	299.97–303.40						
T *Stichocorys wolffii*	3OX-CC–31X-2	283.75–286.10	318.85–321.20						
T *Botryostrobus miralestensis*	30X-5–30X-CC	280.09–283.75							
T *Diartus pettersoni*	30X-5–30X-CC	280.09–283.75	315.19–318.85						
B *Lithopera bacca*	28X-CC–29X-3	264.87–268.30	299.97–303.40						
Diartus pettersoni >*D. hughesi*	3OX-CC–31X-2	283.75–286.10							
B *Diartus hughesi*	3OX-CC–31X-2	283.75–286.10	318.85–321.20						
T *Cyrtocapsella japonica*	32X-CC–33X-3	302.38–306.93	337.48–342.03						
T *Lithopera thornburgi*	33X-CC–34X-3	312.68–316.53	347.78–351.63						
T *Carpocanium cristata*	33X-CC–34X-3	312.68–316.53	347.78–351.63						
T *Lithopera renzae*	36X-3–36X-5	335.84–338.82	366.29–373.92						
T *Cyrtocapsella cornuta*	35X-CC–36X-3	331.72–335.84	366.82–370.94						
B *Diartus pettersoni*	37X-CC–38X-2	345.01–353.55	380.11–388.65						
B *Cyrtocapsella japonica*	36X-CC–37-2	341.53–343.89	376.63–378.99						

Note: T = top; B = bottom.

Table 6. Sample and depth constraints of diatoms events for Site 844.

Event	Hole 846B			Hole 846C			Hole 846D		
	Interval (cm)	Depth (mbsf)	Depth (mbsf)	Interval	Depth (mbsf)	Depth (mcd)	Interval	Depth (mbsf)	Depth (mcd)
T *Nitzschia reinholdii*	3H-2, 70–3H-4, 70	18.70–21.70	20.75–23.75	2H-CC–3H-CC	21.84–31.45	21.37–34.45	2H-CC–3H-CC	21.61–32.93	23.51–34.63
T *Nitzschia fossils*	3H-4, 70–3H-CC	21.70–26.17	23.75–28.22	2H-CC–3H-CC	21.84–31.45	21.37–34.45	3H-CC–4H-CC	32.93–42.69	34.63–46.29
T *Rhizosolenia matuyama*	4H-6, 75–4H-CC	34.25–36.06	37.40–39.21	3H-CC–4H-CC	31.45–41.09	34.45–44.29	4H-CC–5H-CC	42.69–52.10	46.29–57.70
B *Rhizosolenia matuyama*	5H-4, 75–5H-CC	40.75–45.54	45.95–50.74	4H-CC–5H-CC	41.09–50.69	44.29–54.74	5H-CC–6H-CC	52.10–61.38	57.70–66.78
T *Rhizosolenia praebergonii* var *rob.*	6H-CC–7H-2, 75	53.94–56.75	60.44–74.70	6H-CC–7H-CC	58.64–69.71	65.59–76.61	6H-CC–7H-CC	61.38–68.70	66.78–77.10
B *Pseudoeunotia doliolus*	7H-CC–8H-2, 90	64.26–66.40	72.56–76.10	7H-CC–8H-CC	69.71–78.36	76.61–85.96	8H-CC–9H-CC	78.28–88.02	87.68–98.42
T *Thalassiosira convexa* var *convexa*	8H-4, 20–8H-CC	68.70–73.96	75.40–83.66	9H-CC–10H-CC	87.63–97.95	98.88–111.60	10H-CC–11H-CC	97.40–106.26	108.70–118.66
T *Nitzschia jouseae*	10H-CC–11H3, 90	93.23–96.40	105.78–109.9	10H-CC–11H-CC	97.95–106.74	111.60–120.84	11H-CC–12H-CC	106.26–115.91	118.66–129.41
B *Rhizosolenia praebergonii*	12H-4, 90–12H-CC	107.40–111.80	122.20–126.60	10H-CC–12H-CC	97.95–116.52	111.60–132.07	18X-CC–20X-CC	167.95–191.59	190.05–216.89
T *Nitzschia cylindrica*	18H-CC–19H-CC	169.17–178.65	191.02–202.45	17H-CC–18H-CC	164.22–173.34	185.72–196.54	19X-CC–20X-CC	182.44–191.59	205.34–216.89
B *Nitzschia jouseae*	19H-CC–20H-CC	178.65–187.85	202.45–213.45	18H-CC–19H-CC	173.34–183.34	196.54–207.04	21X-CC–22X-CC	201.21–210.74	231.76–241.09
T *Thalassiosira miocenica*	21H-CC–22H-CC	197.68–207.10	224.63–237.55				22X-CC–23X-CC	210.74–220.16	241.09–254.01
T *Nitzschia miocenia*	23X-CC–24X-CC	216.26–225.78	250.26–261.18						
T *Nitzschia miocenia* var *elongata*	23X-CC–24X-CC	216.26–225.78	250.26–261.18				22X-CC–23X-CC	210.74–220.16	241.09–254.01
T *Thalassiosira praeconvexa*	23X-CC–24X-CC	216.26–225.78	250.26–261.18				24X-CC–25X-CC	230.06–239.86	263.41–273.66
B *Thalassiosira miocenica*	25X-4, 70–25X-CC	230.90–232.12	266.00–267.22				24X-CC–25X-CC	230.06–239.86	263.41–273.66
B *Thalassiosira convexa*	25X-4, 70–25X-CC	230.90–232.12	266.00–267.22				25X-CC–26X-CC	239.86–249.45	273.60–283.25
B *Thalassiosira praeconvexa*	25X-CC–26X-CC	232.12–235.61	267.22–270.71						
T *Nitzschia porteri*	27X-1, 75–27X-3, 75	245.95–248.75	281.05–283.85						
B *Nitzschia miocenica*	27X-4, 75–27X-5, 75	250.25–251.75	285.35–286.85						
T *Rosiella palacea*	27X-CC–28X-CC	253.56–264.87	288.66–299.97						
B *Nitzschia cylindrica*	30X-1, 30–30X-2, 30	274.20–275.70	309.30–310.80						
T *Thalassiosira yabei*	30X-1, 30–30X-2, 30	274.20–275.70	309.30–310.80						
T *Denticulopsis hustedtii*	31X-CC–32X-1, 60	293.34–293.70	328.44–328.80						
B *Actinocyclus ellipticus* var *lanc.*	32X-CC–33X-CC	302.38–312.68	337.48–347.78						
T *Craspedodiscus coscinodiscus*	34X-4, 80–34X-CC	317.70–322.29	352.80–357.39						
B *Rossiela paleacea* var *elongata*	34X-4, 80–34X-CC	317.70–322.29	352.80–357.39						
T *Coscinodiscus gigas* var	34X-4, 80–34X-CC	317.70–322.29	352.80–357.39						
T *Actinocyclus ingens*	36X-3, 60–36X-5, 103	335.30–340.70	370.60–375.80						
B *Nitzschia porteri*	36X-5, 103–36X-CC	340.70–341.53	375.80–376.63						
T *Coscinodiscus delicata* var	36X-5, 103–36X-CC	340.70–341.53	375.80–376.63						
B *Coscinodiscus gigas* var	38X-2, 90–38X-5, 41	353.40–357.41	388.50–392.51						
T *Coscinodiscus lewisianus*	38X-1, 90–38X-5, 41	351.90–357.41	387.00–392.51						

Note: T = top; B = bottom; > = evolutionary change.

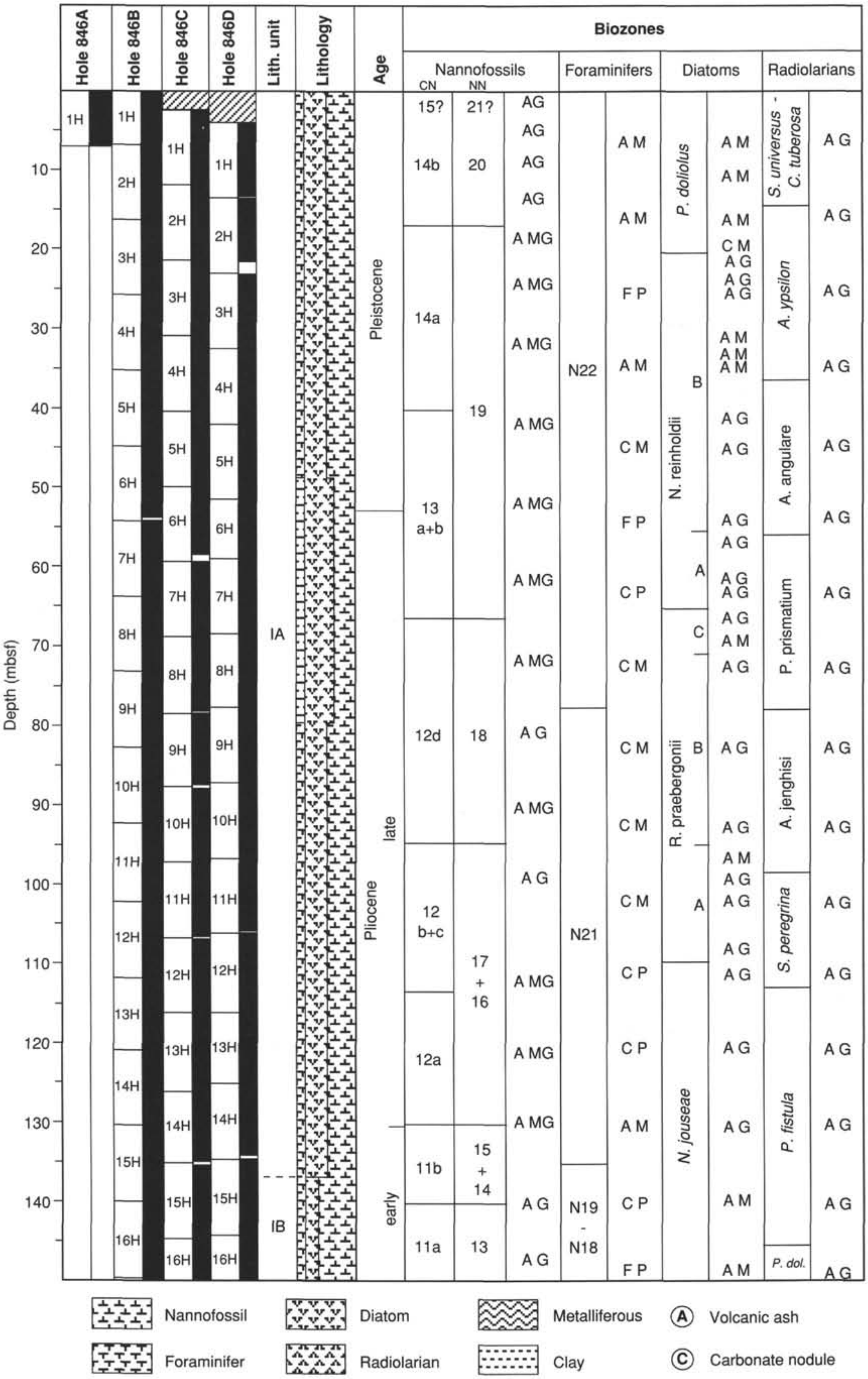

Figure 18. (Caption on next page.)

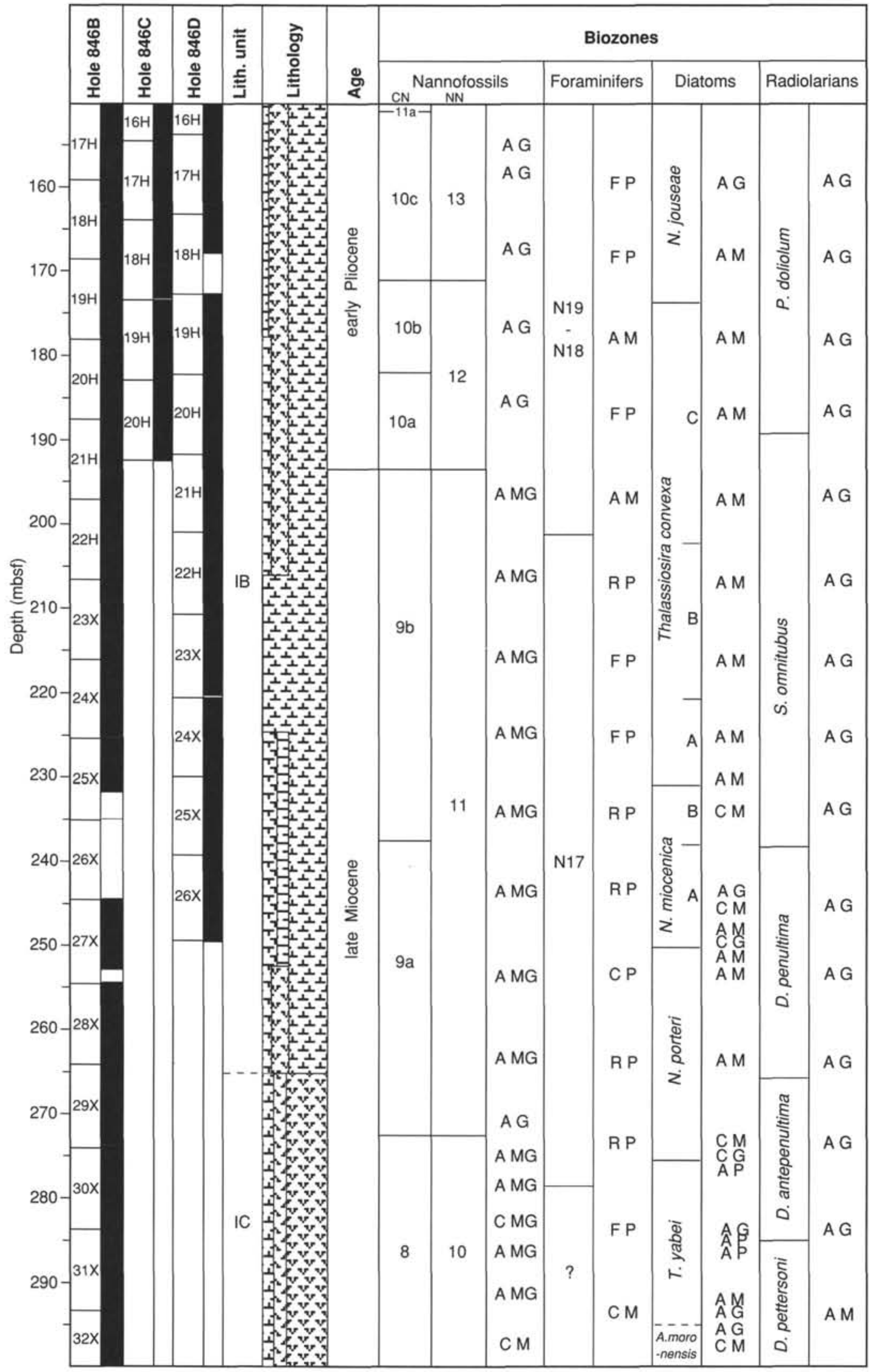

Figure 18 (continued). Biostratigraphic summary for Site 846. Depth is in meters below seafloor (mbsf). Hatched areas represent intervals where zonal assignments could not be made because of rarity or absence of microfossils. Dashed lines represent uncertainty of placement of a zonal boundary. Microfossil abundances are recorded as A = abundant; C = common; F = few; R = rare; B = barren. Microfossil preservation is recorded as G = good; M = moderate; P = poor. This figure is a general overview of biostratigraphic results at Site 846. Data presented in this figure were based on results from Hole 846B. Placement of specific stratigraphic boundaries may differ slightly between Hole 846B and Holes 846C and 846D.

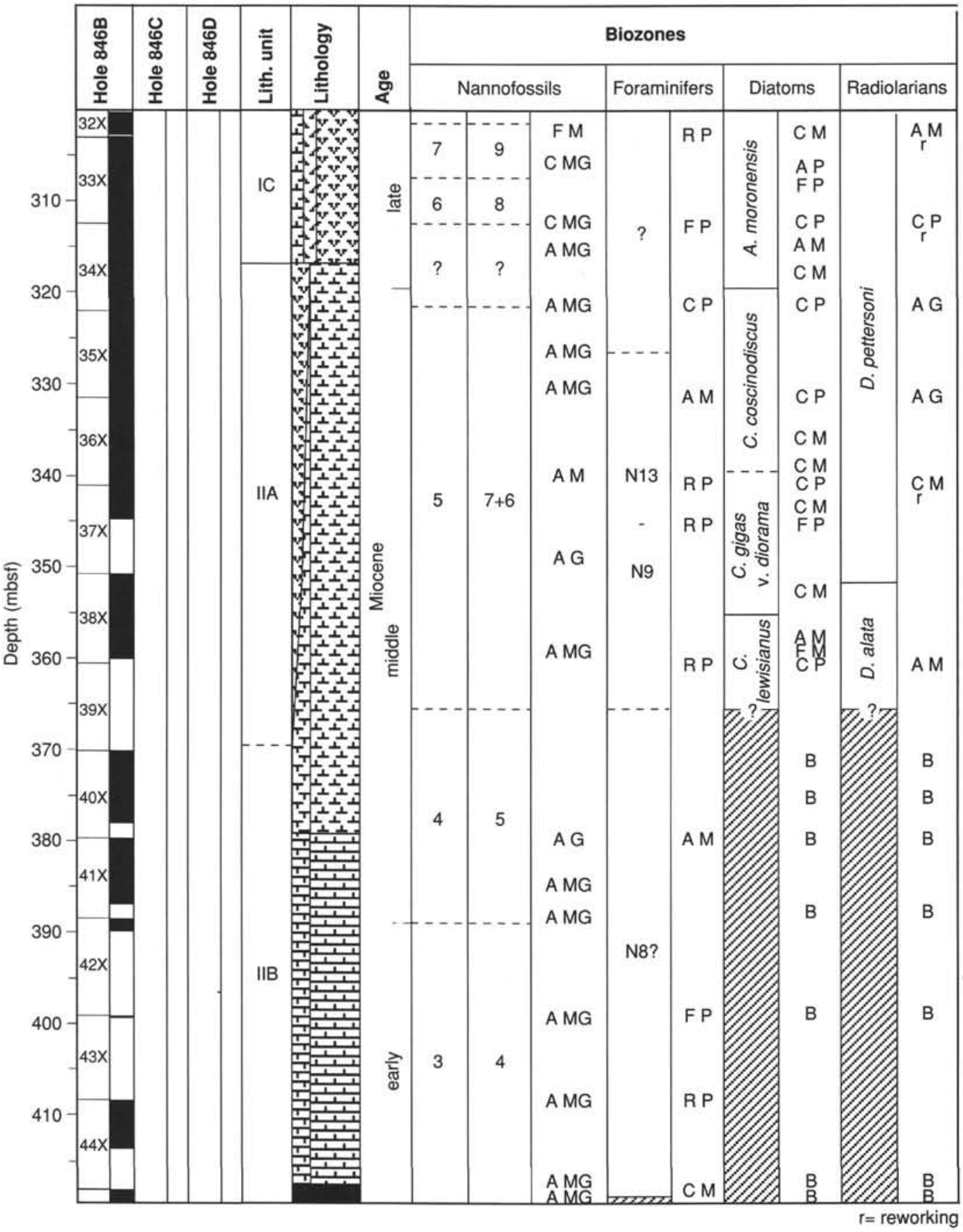

Figure 18 (continued).

first occurrence of *Reticulofenestra pseudoumbilicus* was recorded in Section 138-846B-40X-3 at 100 cm.

The lower Miocene Zone CN3 (NN4) was recognized from Cores 138-846B-42X through -45X. This interval is characterized by the presence of abundant *Sphenolithus heteromorphus, Helicosphaera ampliaperta,* and *Discoaster deflandrei. Discoaster signus* occurs in Cores 138-846B-42X, and -43X, allowing this interval to be assigned to the upper part of Zone CN3 (NN4) (Rio et al., 1990).

Planktonic Foraminifers

Planktonic foraminifers are generally common to abundant in the Pleistocene and Pliocene (Cores 138-846B-1H through -21H), being moderately-well to poorly preserved. Preservation deteriorates downhole. The foraminifer fauna is generally moderately-well preserved from Cores 138-846B-1H through -11H (with intervals of poor preservation in Samples 138-846B-3H-CC, -6H-CC, and -7H-CC), whereas poor preservation dominates from Samples 138-846B-12H-CC through -21H-CC (with intervals of moderate preservation in Samples 138-846B-14H-CC, -19H-CC, and -21H-CC). In the Miocene section (Samples 138-846B-22H-CC through -44X-CC) planktonic fora-minifers are rare to common and poorly preserved.

Throughout the entire sedimentary sequence radiolarians dominate the coarse-fraction residues. Other major coarse-fraction components present throughout most of the sequence are common pyrite, echinoid spines, and sponge spicules, and rare fish teeth. The planktonic foraminifer fauna include a mixture of warm-water assemblages and cooler temperate species. The latter show spikes of abundance in the Pliocene-Pleistocene, probably reflecting variations in the influence of the cool-water Peru Current. The assemblages are largely dominated by members of the *Neogloboquadrina-continuosa-acostaensis-humerosa- dutertrei* group. Other common warm-water species include *Globigerinoides sacculifer, Globigerinoides ruber, Globorotalia tumida* and menardiforms (*Globorotalia menardii* and *Globorotalia limbata*). *Pulleniatina* spp. are rare throughout the Pleistocene and upper Pliocene and exhibit several changes in coiling direction. Temperate-water species include *Globigerina bulloides, Neogloboquadrina pachyderma,* and members of the *Globorotalia inflata-Globorotalia puncticulata* lineage.

Reliable planktonic foraminifer datums identified in the sequence are given in Table 4. The occurrence of common pink *Globigerinoides ruber* in Sample 138-846B-1H-CC indicates that this stratigraphic level is older than 0.125 Ma because these forms are known to last occur throughout the Indo-Pacific at a time equivalent to isotopic stage 5. The rare occurrence of *Globorotalia acostaensis* in Sample 138-846B-3H-CC indicates that this level is older than 0.6 Ma.

Despite the scarcity or absence of a number of the marker species defining Blow's (1969) zones, several boundaries of Blow's zonal scheme were approximated using other species (see Fig. 18). The base of Zone N22 is equated to the last occurrence of *Globorotalia limbata* in Sample 138-846B-8H-CC and the base of Zone N21 is equated to the last occurrence of *Sphaeroidinellopsis* spp. in Sample 138-846B-14H-CC. The base of Zone N18 is marked by the first occurrence of *Globorotalia tumida* in Sample 138-846B-20H-CC. The interval from Samples 138-846B-22H-CC through -29X-CC, which contains *Globorotalia plesiotumida,* is assigned to upper Miocene Zone N17. Below Sample 138-846B-29X-CC, zonal assignments could not be made with certainty. Cores 138-846B-30X through -32X yielded only a rare, poorly preserved planktonic fauna. Rare occurrences of *Sphaeroidinellopsis subdehiscens* were observed down to Sample 138-846B-36X-CC, which indicates an age not older than middle Miocene Zone N13. The co-occurrence of several specimens of *Praeorbulina glomerosa circularis,* however, which indicates a significantly older zonal placement (upper Zones N8 through N9), may result from reworking in the interval. The lower part of the sequence, below Core 138-846B-38X, was tentatively assigned to Zone N8 although the nominate taxon *Praeorbulina sicana* was not found. The planktonic assemblages in this interval are characterized by a small-sized fauna dominated by *Globorotalia mayeri.* Rare species include *Globoquadrina dehiscens, Globoquadrina venezuelana, Globigerinoides subquadratus,* and *Globigerinoides sacculifer. Praeorbulina glomerosa circular* present in the overlying cores, is absent, which suggests placement of in age zone older than upper N8. The absence of *Catpsydrax dissimilis* suggests a placement age younger than N7.

Radiolarians

Radiolarians sampled at Site 846 range in age from the Quaternary (*Collosphaera tuberosa* Zone) to the middle Miocene (*Dorcadospyris alata* Zone). The most recent radiolarian zone (*Buccinosphaera invaginata*) was not identified in any of the holes, and the next two older zones (*Collosphaera tuberosa* and *Stylatractus universus*) could not be differentiated because of the rare and erratic occurrence of *C. tuberosa* in the samples. The oldest material recovered (*D. alata* Zone) is from Sample 138-846B-38X-CC.

The highly expanded Pleistocene-Pliocene section yielded a detailed record of radiolarian events (Table 5). Even zones that are of less than 1 m.y. in duration stretch over more than one core (9.5 m). The radiolarian fauna is abundant and well preserved. As at other sites of the eastern tropical Pacific, it was not possible to accurately define the first appearances of *Amphirhopalum ypsilon* and *Spongaster tetras* because of their rather sporadic occurrence—particularly early in their ranges. The range of *Spongaster berminghami* was also impossible to define because of its rare occurrence. *Spongaster pentas* was not found in the samples studied.

Radiolarians are common to abundant throughout the upper and middle Miocene part of the section, and preservation is generally good. Below Core 138-846B-32X, however, biosiliceous tests show signs of dissolution and reprecipitation. All samples in deeper cores had to be treated with NaOH to break up sediment aggregates. In and below Core 138-846B-40X (in which chert was found) all samples studied were barren of radiolarians.

All the major radiolarian zones of the upper and middle Miocene were identified, as were most of the datums commonly noted by previous studies of the tropical oceans (Table 5). Incomplete recovery of Cores 138-846B-25X and -26X makes the placement of the boundary between the *Didymocyrtis penultima* and *Solenosphaera omnitubus* zones in this hole imprecise. The last occurrence of *Calocycletta caepa* also falls in this recovery gap. Cores 138-846D-25X and -26X, however, fill this gap (see "Sedimentation Rates" section, this chapter) and tie down these datums to within a few meters (Table 5). *Acrobotrys tritubus,* a rare species in most cases, is extremely rare in the samples studied. *Lithopera thornburgi* also appears to be unusually rare at this site. Little confidence should be placed in the noted ranges of either of these species (Table 5). The dissolution of bio-genic silica in the lower part of the section (below Core 138-845B-32X) may have removed some of the more delicate species (e.g., *L. thornburgi*) and added to the difficulty of accurately defining datum levels.

Diatoms

Diatoms are generally present in the Quaternary through middle Miocene sequence recovered from Holes 846A–846D (Table 6). Diatoms are common to abundant in most samples examined, except for samples from Cores 138-846B-40X through -45X, which are barren of diatoms. Preservation of diatoms varies from poor to good in the samples analyzed. The interval from Samples 138-846B-32X through -33X is characterized by poor to moderate preservation.

The Pliocene assemblage is characterized by: *Actinocyclus ellipticus, Azpeitia nodulifer, Hemidiscus cuneiformis, Nitzschia fossilis, Nitzschia jouseae, Nitzschia marina, Nitzschia reinholdii, Pseudoeunotia doliolus, Rhizosolenia bergonii, Rhizosolenia praebergonii, Roperia tesselata, Thalassionema nitzschioides, Thalassionema nitzschioides* var. *parva, Thalassiosira convexa, Thalassiosira oestrupii,* and *Thalassiothrix longissima.*

The Miocene assemblage is characterized by: *Actinocyclus ellipticus, Cestodiscus pulchellus, Coscinodiscus lewisianus, Craspedodiscus coscinodiscus, Crucidenticula nicobarica, Denticulopsis hustedtii, Hemidiscus cuneiformis, Nitzschia cylindrica, Nitzschia miocenica, Rossiella praepaleacea, Thalassionema nitzschioides, Thalassiosira yabei* Group, and *Thalassiothrix longissima.*

One core was recovered from Hole 846A. The occurrence of *P. doliolus* without *N. reinholdii* places this sample in the *P. doliolus* Zone. Sections 138-846B-1H through -3H-2, -846C-1H-CC through -2H-CC, and -846D-1H-CC through -2H-CC also were placed in this zone. Samples 138-846B-3H-6, 70 cm, through -6H-CC, -846C-3H through -6H-CC, and -846D-3H-CC through -5H-CC were assigned to Subzone B of the *N. reinholdii* Zone. This zonal assignment was based on the co-occurrence of *P. doliolus* and *N. reinholdii* stratigraphically above the last occurrence of *R. praebergonii.* The last occurrence of this species was placed in Samples 138-846B-7H-2, 75 cm, -846C-7H-CC, and -846D-6H-CC, which allowed us to assign these samples to Subzone A of the *N. reinholdii* Zone. The base of this subzone, defined by the first occurrence of *P. doliolus,* was placed in Samples 138-846B-7H-CC, -854C-7H-CC, and -846D-6H-CC.

Samples 138-846B-8H-2, 90 cm, through -12H-4, 90 cm, 138-846C-8H-CC through -10H-CC, and 138-846D-7H-CC through -11H-CC, were assigned to the *R. praebergonii* Zone. Samples 138-846B-8H-2, 90 cm, and -8H-4, 20 cm, were assigned to Subzone C of this zone, based on the occurrence of *R. praebergonii* stratigraphically below the first occurrence of *P. doliolus* (Sample 138-846B-7H-CC) and stratigraphically above the last occurrence of *T. convexa* (Sample 138-846B-8H-CC). Samples 138-846B-9H-CC and -10H-CC were assigned to Subzone B of this zone, based on the co-occurrence of *T. convexa* and *R. praebergonii* without *N. jouseae*. Samples 138-846B-11H-3, 90 cm, through 12H-4, 90 cm, were assigned to Subzone A on the basis of the co-occurrence of *N. jouseae, T. convexa,* and *R. praebergonii.*

Cores 138-846B-12H through -19H, -846C-11H through -18H, and -846D-11H through -19H were assigned to the *N. jouseae* Zone, based on the occurrence of this species in these samples stratigraphically below the first occurrence of *R. praebergonii.* Diatoms are generally abundant and well preserved throughout this interval.

Samples 138-846B-20H-CC through -25X-4, 70 cm, -846C-19H and -20H-CC, and -846D-20H-CC through -24H-CC, were placed in the *T. convexa* Zone. Samples 138-846B-20H-CC and -21X-CC were assigned to Subzone C of this zone, which consisted of the interval between the last *T. miocenica* and the first *N. jouseae*. Sample 138-846-23H-CC is assigned to Subzone B. The occurrence of *T. praeconvexa, N. miocenica, T. miocenica, T. convexa,* and *N. miocenica* var. *elongata* allows Samples 138-846B-24X-CC through -25X-4, 70 cm, to be assigned to Subzone A of the *T. convexa* Zone. Samples 138-846B-26X-CC through -27X-4, 70 cm, and 138-846D-25X-CC, and -26X-CC, are assigned to the *N. miocenica* Zone based on the occurrence of *N. miocenica* without *T. convexa*. This interval was not cored in Hole 846C. The interval from Samples 138-846B-27X-5, 75 cm, through -30X-1, 30 cm, is assigned to the *Nitzschia porteri* Zone.

Preservation of diatoms in the interval equivalent to, and stratigraphically below the *T. yabei* zone (Cores 138-846B-30X through -38X) is generally poor to moderate. As a result, the stratigraphic constraints in this interval are dependent on stratigraphic markers that are robust and easily identified. Although other more finely silicified species are occasionally present, their occurrence is sporadic. Useful events in this interval include the last occurrence of *T. yabei,* the last occurrence of *D. hustedtii,* the last occurrence of *C. coscinodiscus,* and the last occurrence of *C. lewisianus.*

The last occurrence of the *T. yabei* in Sample 130-846B-30X-2, 30 cm, marks the top of the *T. yabei* Zone. Placement of this zonal boundary was supported by the first occurrence of *Nitzschia cylindrica* in Sample 130-846B-30X-1, 30 cm. The base of the *T. yabei* Zone approximates Sample 138-846B-32X-2, 60 cm, although the marker species, *Actinocyclus moronensis,* is not present. This sample contains abundant specimens of *D. hustedtii,* suggesting that the last occurrence of *D. hustedtii* approximates the interval from this sample to the top of the core. Elsewhere in the equatorial Pacific Ocean, the last occurrence of *D. hustedtii* approximates the last occurrence of *A. moronensis* (Barron, 1985). The last occurrence of *C. coscinodiscus* defines the *A. moronensis/C. coscinodiscus* zonal boundary. This event was placed in Sample 138-846B-34X-CC, allowing us to place Samples 138-846B-34X-CC through -36X-5, 103 cm, in the *C. coscinodiscus* Zone.

The occurrence of rare specimens of *Thalassiosira temperi* var. *delicata* in Sample 138-846B-36X-5, 103 cm, suggests that this sample is equivalent to the lowermost portion of the *C. coscinodiscus* zone and may approximate the *C. coscinodiscus/Coscinodiscus gigas* var. *diorama* zonal boundary. Such a stratigraphic placement is supported by the occurrence of *N. porteri* in this sample.

Samples 138-846B-36X-CC through -38X-1, 90 cm are assigned to the *C. gigas* var. *diorama* Zone. This zonal assignment is based on secondary evidence that includes the occurrence of *Cestodiscus pulchellus, Coscinodiscus gigas* var. *diorama,* and *Actinocyclus ingens* (throughout this interval).

The last occurrence of *Coscinodiscus lewisianus* is placed in Sample 138-846B-38H-5, 41 cm, indicating that this sample is equivalent to the *C. lewisianus* Zone. Diatoms were not observed in samples examined below Core 846B-38X-CC.

PALEOMAGNETISM

At Site 846, the magnetic signal was weak, and the natural remanent magnetization (NRM) was dominated by a steep upward overprint. AF demagnetization to 15 mT was successful in removing much of the overprint, but the residual signal was extremely weak (in the range of 10^{-4} A/m, about the same as an empty core liner); thus, it was impossible to isolate a direction reliably. For this reason, we limited remanence measurements to the 22 APC cores of Hole 846B (the NRM was measured for two sections per core and the remaining sections were measured after AF demagnetization at 15 mT). Similar efforts to measure discrete samples were unsuccessful because the noise level of the Molspin magnetometer was reached after AF demagnetization to 10 mT. Thus, the highly scattered directions do not show defined reversed and normal polarities and any interpretation of the results in terms of geomagnetic field would be highly speculative.

Shore-based studies of specific rock magnetic parameters may help to explain the origin and downcore evolution of the very weak and "soft" remanence observed at Site 846. Figure 19 shows that there is no correlation between susceptibility data and the magnetization intensity. Surprisingly good correlation of the susceptibility features is observed between Holes 846B and 846C (Fig. 20), especially when considering the low measured signal; however, at some levels the amplitude of the variations differs significantly between the two holes (for reasons which we do not understand at present). Detailed investigations of the magnetic mineralogy are necessary to understand the origin of the downhole variations at Site 846.

SEDIMENTATION RATES

A sedimentary section more than 400 m thick covering the time interval from the late Pleistocene to the early Miocene was recovered at Site 846. Biostratigraphic age control was provided by all four of the chief planktonic microfossil groups.

The composite depth section for Site 846 is given in Table 7. This composite was formed by comparing shipboard measurements of GRAPE, magnetic susceptibility, and percentage of reflectance at adjacent holes. These comparisons then were integrated to form a single composite depth section for that site (a detailed discussion about the construction of composite sections during Leg 138 is presented in Hagelberg et al., this volume).

For the holes and cores listed in Column 1 of Table 7, the ODP sub-bottom depth of the core top and core bottom (in meters below seafloor, or mbsf) is given in Column 2. Note that these depths given in Column 2 correspond to the depth of the bottom of the recovered core. This depth places the core-catchers in their correct position in the composite depth section and is not the same as the standard ODP core-catcher depth. Column 3 shows the length of core recovered. Column 4 gives the composite depth of the core top and core bottom (in meters composite depth, or mcd). Column 5 indicates the amount of offset between the ODP depth and the composite depth. For each core, conversion from ODP sub-bottom depth (mbsf) of any sample to mcd is done by adding the offset listed in Column 5 for that core.

GRAPE density and percent reflectance data both produced records with high amplitudes and variability through Holes A, B, C, and D at Site 846. Although the large-scale (5- to 10-m scale) features in these data sets are similar, smaller scale (order of 1 m) features in the GRAPE and reflectance records are distinctly different, providing independent data sets for a fairly detailed correlation. The magnetic susceptibility record at Site 846 is generally of low amplitude and was not used to correlate between holes. However, when the magnetic susceptibility records from Holes 846B and D are displayed on the composite section, it is evident that the data for the two holes are well correlated (Fig. 21, back pocket) despite the fact that the amplitude of the signal is so low.

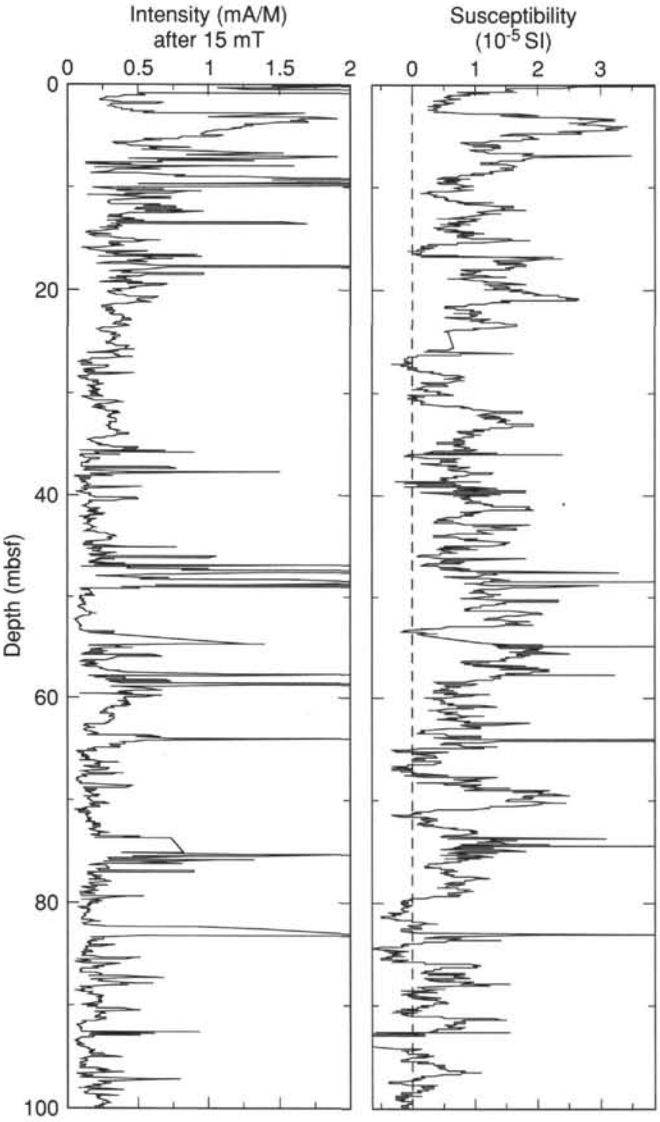

Figure 19. Low-field magnetic susceptibility compared with remanence intensity in Hole 846B.

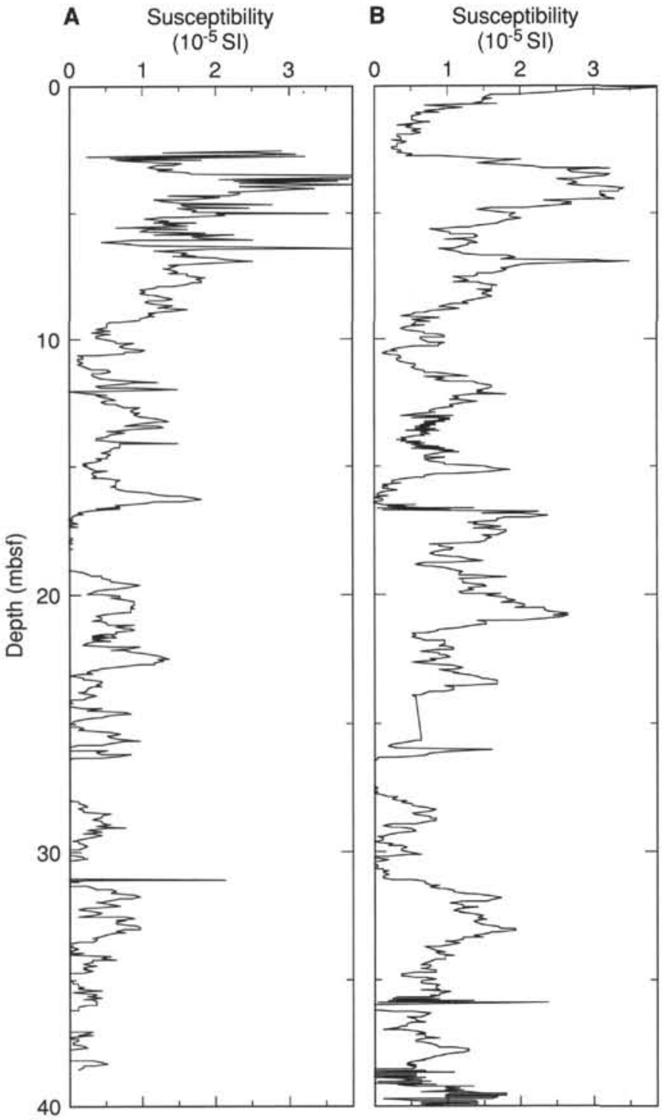

Figure 20. Low-field susceptibility measured from the upper 40 m of sediment recovered from Holes 846B (**A**) and 846C (**B**).

Analysis of the composite depth section shows that the cored intervals in Holes 846A, 846B, 846C, and 846D recovered a continuous section with overlap down to 260 mcd. At this site, for the first time, we attempted detailed correlation among sections recovered with the XCB, as well as those recovered with the APC. The only interval with ambiguity as to the amount of overlap is between Cores 138-846B-23X and -846D-22X. Distortion within a core hindered correlation in many instances, particularly in intervals that have been cored using the XCB. Examples of this distortion can be seen between Cores 138-846B-2H, -846C-2H, and -846D-2H, between Cores 138-846B-17H, -846C-17H, and -846D-17H, and between Cores 138-846B-19H, -846C-19H, and -846D-19X. Although the amount of distortion within cores increased in the XCB-cored sections from Holes 846B and 846D, it was possible to form a composite section based on GRAPE and percentage of reflectance data.

Developing a satisfactory sedimentation rate record for Site 846 was hampered by the absence of a paleomagnetic record. However, all four microfossil groups provided good biostratigraphic information in different parts of the record. Table 8 gives the control points selected to generate the age-depth plot shown in the four panels of Figure 22. On each panel all the first and last appearance datums observed in Hole 846B are plotted with their assigned ages and the depth limits (mcd) within which they were observed.

Control points were selected as follows (in all cases the details may be found in the biostratigraphy section, this chapter). At 2.41 Ma the extinction of *Discoaster surculus* was used. A minor conflict occurs with the diatom data here as the upper limit of *Nitschia jouseae* (2.64 Ma) was observed at about the same level, but much more detailed shore-based work will be needed to resolve such details. At 4.89 Ma, the control provided by the upper limit of *Discoaster quinqueramus* is in good agreement with the controls by the other groups. The next good nannofossil datum is the first appearance of *Discoaster berggreni*. This datum was placed between 7.42 and 7.50 Ma at Site 844, and between 7.51 and 7.52 Ma in Site 845, both with good paleomagnetic control. We have used 7.50 rather than the published age of 8.0 Ma (see Explanatory Notes, this volume). We have also used the calibration provided by the paleomagnetic record of Site 845 for the upper limit of *Coccolithus miopelagicus* at 9.94 Ma. Using these last three datums generates a sharp change in sedimentation rate at 7.52 Ma and a line that is in conflict with all of the diatom datums over the range 7 to 5 Ma. By assuming that the change in sedimentation rate occurred slightly higher in the section than the control point

Table 7. Depths of top and bottom of each core in Site 846 in the composite depth section.

Core	Depth (mbsf)	Length of core (m)	Composite depth (mcd)	Δ (m)
138-846A				
1H	0–7.22	7.22	0–7.22	0.00
138-846B				
2H	7.00–16.89	9.89	7.60–17.49	0.60
3H	16.50–26.17	9.67	18.55–28.22	2.05
4H	26.00–36.06	10.06	29.15–39.21	3.15
5H	35.50–45.54	10.04	40.70–50.74	5.20
6H	45.00–53.94	8.94	51.50–60.44	6.50
7H	54.50–64.26	9.76	62.80–72.56	8.30
8H	64.00–73.96	9.96	73.70–83.66	9.70
9H	73.50–83.07	9.57	83.65–93.22	10.15
10H	83.00–93.23	10.23	95.55–105.78	12.55
11H	92.50–102.26	9.76	106.00–115.76	13.50
12H	102.00–111.80	9.80	116.80–126.60	14.80
13H	111.50–121.65	10.15	127.95–138.10	16.45
14H	121.00–130.78	9.78	138.15–147.93	17.15
15H	130.50–140.62	10.12	150.20–160.32	19.70
16H	140.00–149.82	9.82	160.20–170.02	20.20
17H	149.50–159.65	10.15	170.75–180.90	21.25
18H	159.00–169.17	10.17	180.85–191.02	21.85
19H	168.50–178.65	10.15	192.30–202.45	23.80
20H	178.00–187.85	9.85	203.60–213.45	25.60
21H	187.50–197.68	10.18	214.45–224.63	26.95
22H	197.00–207.10	10.10	227.45–237.55	30.45
23X	206.50–216.26	9.76	240.50–250.26	34.00
24X	216.20–225.78	9.58	251.60–261.18	35.40
25X	225.70–232.12	6.42	260.80–267.22	35.10
26X	235.60–235.61	0.01	270.70–270.71	35.10
27X	245.20–253.56	8.36	280.30–288.66	35.10
28X	254.90–264.87	9.97	290.00–299.97	35.10
29X	264.20–273.74	9.54	299.30–308.84	35.10
30X	273.90–283.75	9.85	309.00–318.85	35.10
31X	283.50–293.34	9.84	318.60–328.44	35.10
32X	293.10–302.38	9.28	328.20–337.48	35.10
33X	302.80–312.68	9.88	337.90–347.78	35.10
34X	312.40–322.29	9.89	347.50–357.39	35.10
35X	322.00–331.72	9.72	357.10–366.82	35.10
36X	331.70–341.53	9.83	366.80–376.63	35.10
37X	341.30–345.01	3.71	376.40–380.11	35.10
38X	351.00–360.20	9.20	386.10–395.30	35.10
39X	360.60–360.60	0.00	395.70–395.70	35.10
40X	370.30–378.19	7.89	405.40–413.29	35.10
41X	379.90–387.11	7.21	415.00–422.21	35.10
42X	389.60–390.96	1.36	424.70–426.06	35.10
43X	399.20–399.41	0.21	434.30–434.51	35.10
44X	408.90–414.14	5.24	444.00–449.24	35.10
45X	418.60–420.21	1.61	453.70–455.31	35.10
138-846C				
1H	2.50–12.20	9.70	2.85–12.55	0.35
2H	12.00–21.84	9.84	11.53–21.37	-0.47
3H	21.50–31.45	9.95	24.50–34.45	3.00
4H	31.00–41.09	10.09	34.20–44.29	3.20
5H	40.50–50.69	10.19	44.55–54.74	4.05
6H	50.00–58.64	8.64	56.95–65.59	6.95
7H	59.50–69.71	10.21	66.40–76.61	6.90
8H	69.00–78.36	9.36	76.60–85.96	7.60
9H	78.50–87.63	9.13	89.75–98.88	11.25
10H	88.00–97.95	9.95	101.65–111.60	13.65
11H	97.50–106.74	9.24	111.60–120.84	14.10
12H	107.00–116.52	9.52	122.55–132.07	15.55
13H	116.50–126.25	9.75	133.00–142.75	16.50
14H	126.00–135.17	9.17	144.40–153.57	18.40
15H	135.50–145.22	9.72	154.00–163.72	18.50
16H	145.00–154.74	9.74	165.70–175.44	20.70
17H	154.50–164.22	9.72	176.00–185.72	21.50
18H	164.00–173.34	9.34	187.20–196.54	23.20
19H	173.50–183.34	9.84	197.20–207.04	23.70
20H	183.00–193.00	10.00	208.30–218.30	25.30
138-846D				
1H	4.00–13.29	9.29	3.00–12.29	-1.00
2H	13.50–21.61	8.11	15.40–23.51	1.90
3H	23.00–32.93	9.93	24.70–34.63	1.70
4H	32.50–42.69	10.19	36.10–46.29	3.60
5H	42.00–52.10	10.10	47.60–57.70	5.60
6H	51.50–61.38	9.88	56.90–66.78	5.40
7H	58.80–68.70	9.90	67.20–77.10	8.40
8H	68.30–78.28	9.98	77.70–87.68	9.40
9H	77.80–88.02	10.22	88.20–98.42	10.40
10H	87.30–97.40	10.10	98.60–108.70	11.30
11H	96.80–106.26	9.46	109.20–118.66	12.40
12H	106.30–115.91	9.61	119.80–129.41	13.50
13H	115.80–125.89	10.09	130.40–140.49	14.60
14H	125.30–134.31	9.01	142.10–151.11	16.80
15H	134.80–144.90	10.10	152.80–162.90	18.00
16H	144.30–154.31	10.01	164.30–174.31	20.00
17H	153.80–163.61	9.81	174.60–184.41	20.80
18X	163.30–167.95	4.65	185.40–190.05	22.10
19X	172.80–182.44	9.64	195.70–205.34	22.90
20X	181.80–191.59	9.79	207.10–216.89	25.30
21X	191.40–201.21	9.81	221.95–231.76	30.55
22X	201.10–210.74	9.64	231.45–241.09	30.35
23X	210.70–220.16	9.46	244.55–254.01	33.85
24X	220.40–230.06	9.66	253.75–263.41	33.35
25X	230.10–239.86	9.76	263.90–273.66	33.80
26X	239.80–249.45	9.65	273.60–283.25	33.80

Table 8. Control points for accumulation rates.

Composite depth (m)	Sedimentation rate (m/m.y.)	Age (Ma)	Comments
0		0	Top of sedimentary section
	40.0		
44.85		1.12	T *Gephyrocapsa* spp > 5.5 µm
	32.8		
59.92		1.58	B *Gephyrocapsa oceanica*
	46.4		
98.40		2.41	T *Discoaster surculus*
	44.13		
149.37		3.56	T *Reticulofenestra pseudoumbilicus*
	49.9		
220.2		4.98	T *Discoaster quinqueramus*
	39.3		
299.5		7.00	extension of rate below (see text)
	14.6		
306.65		7.49	B *Discoaster berggreni* (age estimated in Sites 844 and 845 near the base of magnetochron C5N)
	15.1		
343.75		9.94	T *Coccolithus miopelagicus* (age estimated in Site 845 within the lower part of magnetochron C5N1)
	15.8		
400.1		13.50	T *Sphenolithus heteromorphus*
	10.4		
426.06		16.00	T *Helicosphaera ampliaperta*

Note: T = top; B = bottom.

provided by the first appearance of *D. berggreni,* it is easy to remove this conflict. We therefore extrapolated the low sedimentation rate for the section between 337 and 302 mcd upward to 295 mcd at 7 Ma. The addition of a control point at this age and position provides excellent agreement with the succession of diatom datums and the only conflict is with the first observed specimens of *Amaurolithus primus*; this is not of concern in view of the very poor carbonate preservation in that part of the section, which has probably masked the true evolutionary appearance of the species. In the section below the change in rate, the last observed specimens of *Discoaster hamatus* at about 330 mcd are not regarded as providing a reliable age estimate (see Biostratigraphy section, this chapter); apart from these exceptions, agreement with the nannofossil and diatom datums is very good. Although a number of radiolarian datums appear to be in conflict, this reflects the fact that many of these are based on very rare species and should not be regarded as useful datums for the purpose of age calibration.

Sedimentation rates vs. age (Fig. 23) and vs. composite depth (Fig. 24) show relatively constant high rates of 40–50 m/m.y. in the upper part of the section and relatively constant lower rates of around 15 m/m.y. below that. Using the literature age of 16.0 Ma for the upper limit of *Helicosphaera ampliaperta* implies a lower rate of about 10 m/m.y. between 13.5 and 16 Ma, which if extrapolated would put the basement age at almost 19 Ma. The nannofossils data constrain the basement age at younger than 18.4 Ma (since the lowest sample, just above basement, is still within zone CN3). We have not attempted to estimate sedimentation rates on this basis because, although the figures that we are using would require that the sedimentation rate was higher in the bottom 30 m of the section, only very small and somewhat likely adjustments to the control ages would permit a uniform sedimentation rate to basement. For example, were the true age of the *H. ampliapertura* extinction 15.5 Ma, then an extrapolation using the new sedimentation rate of around 13 m/m.y. should predict a basement age of about 17.5 Ma, well within the nannofossil constraint.

INORGANIC GEOCHEMISTRY

Eighteen interstitial-water samples were collected at Site 846, three from Hole 846A at depths ranging from 3.0 to 7.5 mbsf and fifteen from Hole 846B at depths ranging from 51.0 mbsf to just above basement at 419.6 mbsf (Table 9). Results from these two holes are considered to constitute a single depth profile in this report. Three interstitial water samples were taken from the solitary core making

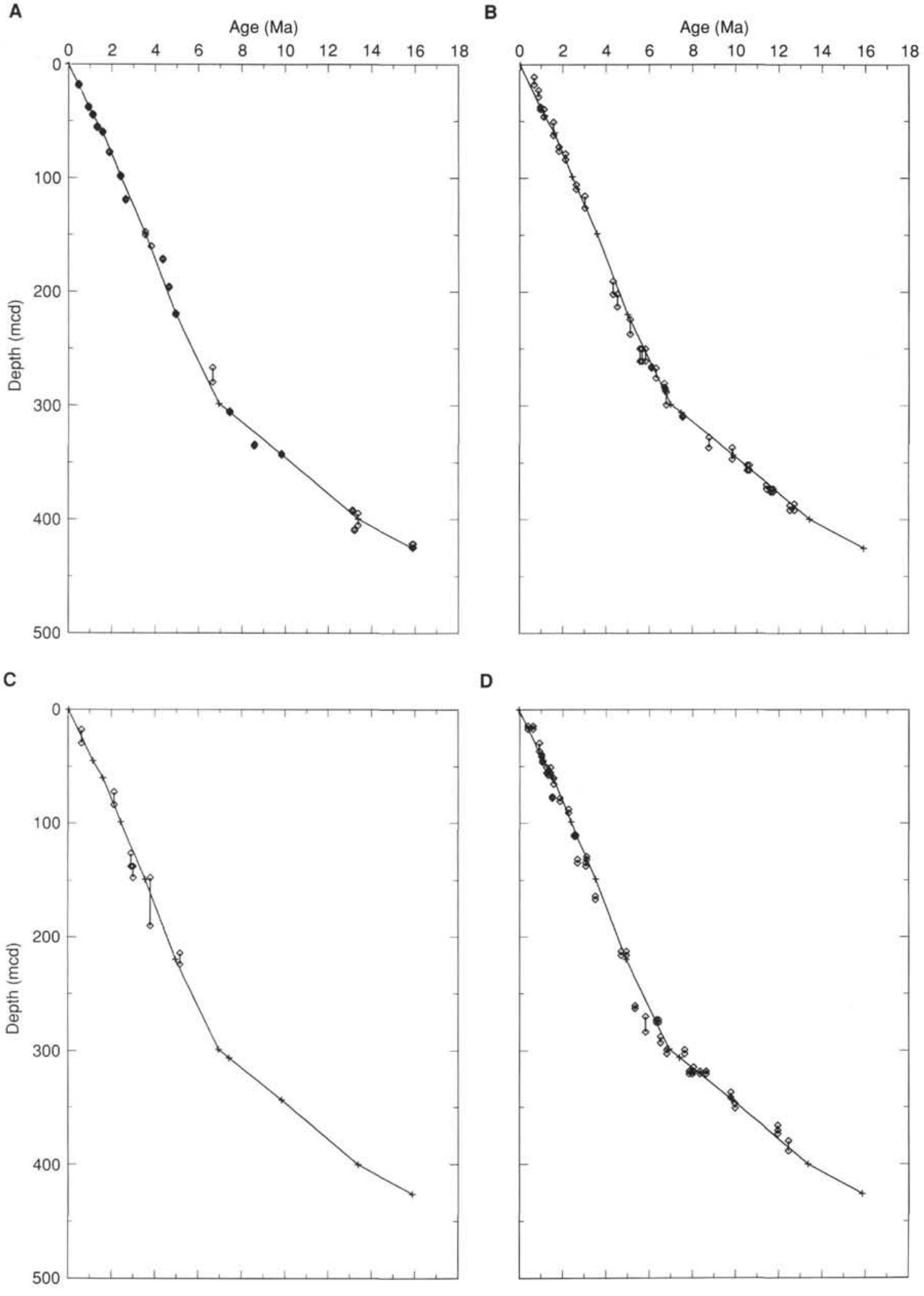

Figure 22. Plot of age vs. depth for Site 846, based on the calibration points (solid line) in Table 8, together with biostratigraphic datums. **A.** Nannofossils. **B.** Diatoms. **C.** Foraminifers. **D.** Radiolarians. Depth range in which each datum was recognized has been indicated by two symbols joined by a line; if the line is not visible, the datums were determined to within the size of the symbols.

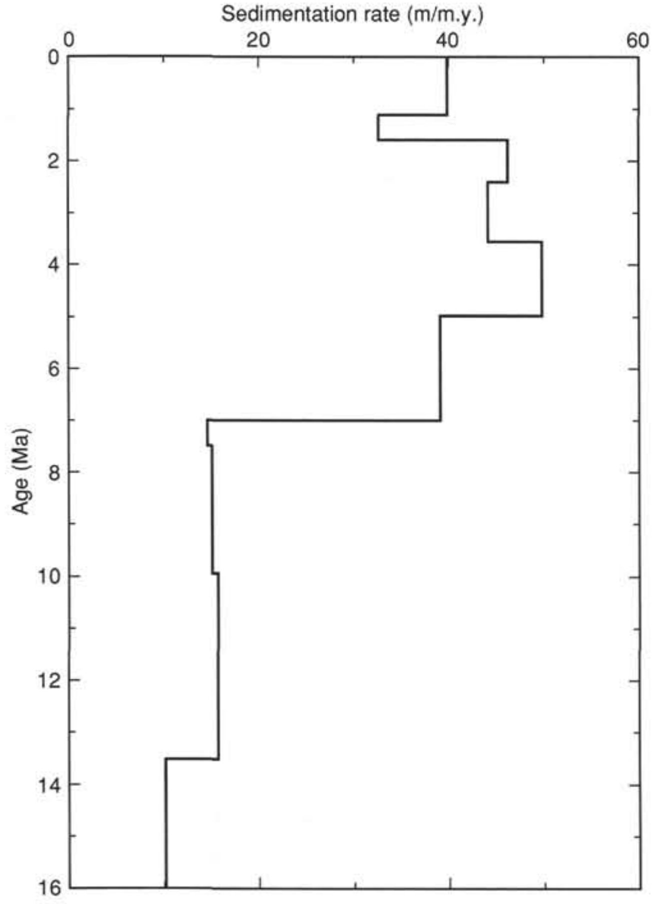

Figure 23. Linear sedimentation rate vs. age, based on data in Table 8.

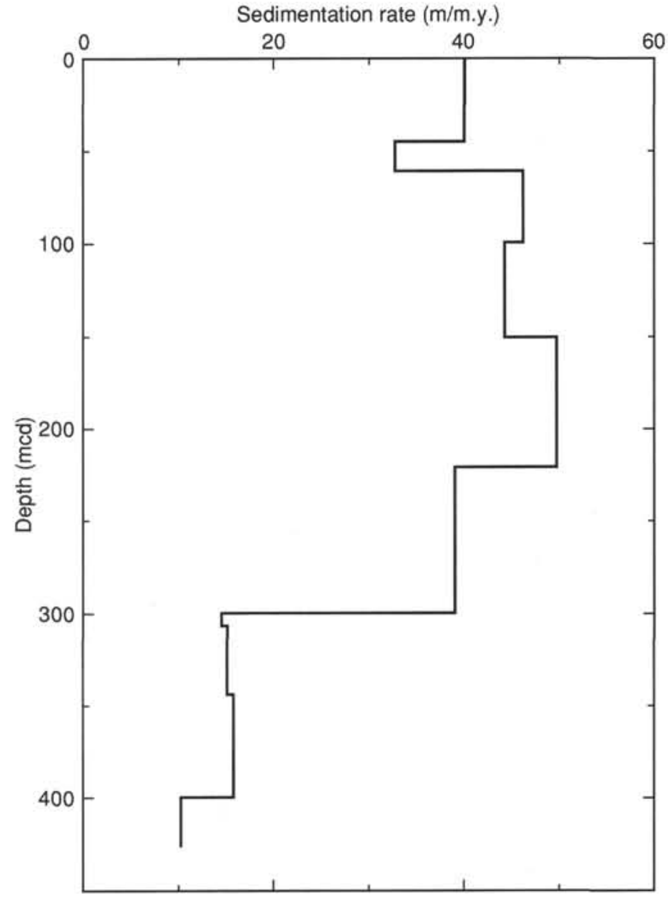

Figure 24. Linear sedimentation rate vs. composite depth, based on data in Table 8.

up Hole 846A. Sediments in this hole consisted of nannofossil foraminifer diatom ooze (see "Lithostratigraphy" section, this chapter). Interstitial-water sampling in Hole 846B began with a sample from the sixth core (Sample 138-846B-6H-4), where the sediment consisted of nannofossil ooze with diatoms. It is worth noting that Sample 138-846B-40X-4 was taken from a core (370.3–379.9 mbsf) that contained several chert and carbonate nodules. The next two samples (138-846B-41X-4 and -846B-44X-3) were recovered from a light greenish gray clayey foraminifer nannofossil chalk. The deepest interstitial water sample from this site (138-846B-45X-1) was squeezed from metalliferous sediment (nannofossil-rich) recovered from the last core taken from this hole, Core 138-846B-45X, which also contained basalt breccia. The catcher associated with this core (138-846B-45X-CC) was filled with altered basalt hosting veins of secondary calcite.

Chemical gradients at this site (Table 9) are governed by diagenesis, crystallization, and the diffusive influence of basalt alteration reactions in basement rocks. Several parameters measured in the interstitial waters from this site tell us that these sediments are more reducing than those sampled at the two previous sites on this leg. This general conclusion is consistent with the presence of free H_2S in these sediments.

The smell of H_2S became noticeable in Core 138-846B-3H and was persistent at about the same level down to Core 138-846B-15H. The H_2S smell diminished below this depth, becoming faint by Core 138-846B-23H and unnoticeable by Core 138-846B-27H.

Sodium (Fig. 25A), as calculated by charge balance, displays only small fluctuations with depth except near basement. Likewise, if one ignores the two bottom samples (Samples 138-846B-44X-3 and -45X-1), chloride at this site (Fig. 25B) does not vary (± 2 mM) within our ability to make this measurement (0.4%). Sodium and chloride decrease within the clayey foraminifer nannofossil chalk that characterizes the bottom of Hole 846B. There are two possible explanations for the trends in sodium and chloride near basement. Either these elements are taken up during alteration of basal sediments and basement rocks, or these concentration minima are superimposed onto the sediment column by advection.

The alkalinities at Site 846 (Fig. 25C) are higher than those found at the two previous sites. These relatively high alkalinities suggest that the interstitial waters from this site are more reducing and corrosive. This inference is supported by lower pH values (Table 9) and is consistent with the generally higher organic carbon contents of these sediments (see Organic Geochemistry section, this chapter) when compared to Sites 844 and 845. The interstitial waters from Site 846, however, are not reductive in the extreme. Alkalinities in truly reducing sediments (i.e., 0 sulfate) can reach concentrations that are 10-fold higher than the levels found at this site; such as those sampled by Harrison et al. (1982) at Sites 496 and 497 on the Middle America Trench slope during DSDP Leg 67.

The profile of sulfate with depth (Fig. 25D) is essentially the mirror-image of alkalinity and also suggestive of mild anoxia. While the lowest sulfate was measured in Sample 138-846B-24X-5 collected from 223.7 mbsf, the steepest gradient in sulfate occurs much higher in the sediment column, between Cores 138-846A-1H (3 mbsf) and -846B-6H (51.0 mbsf). This observation implies that most reduction at this site occurs above 50 mbsf, with less activity between 50 and 200 mbsf. Below this depth, the sulfate profile is linear down to about 375 mbsf, suggesting diffusion-control. The distribution of reductive activity inferred from the profiles of alkalinity (Fig. 25C) and sulfate (Fig. 25D) are supported by the odorous record of H_2S downhole.

Table 9. Interstitial-water geochemical data for Holes 846A and 846C.

Core, section, interval (cm)	Depth (mbsf)	pH	Salinity	Chloride (mM)	Sodium (mM)	Alkalinity (mM)	Sulfate (mM)	Magnesium (mM)	Calcium (mM)	Potassium (mM)	Strontium (μM)	Lithium (μM)	Silica (μM)	Ammonia (μM)
138-846A														
1H-2, 0–5	3.0	7.41	35.5	552	481	3.201	28.08	53.34	10.33	11.1	89	28.5	892	59
1H-3,145–150	4.5	7.32	34.5	552	481	3.554	27.90	53.10	10.17	11.6	91	28.8	908	138
1H-5, 0–5	7.5	7.39	35.0	552	480	3.599	27.04	53.25	9.94	11.3	93	28.8	910	165
138-846B														
6H-4, 145–150	51.0	7.69	35.8	556	481	6.857	22.85	52.55	7.91	11.2	172	27.7	902	572
9H-4, 145–150	79.5	7.53	35.0	556	480	6.950	21.78	52.34	7.64	10.9	196	25.9	900	677
12H-4, 145–150	108.0	7.18	35.5	559	483	7.061	21.36	51.44	7.81	10.8	227	23.7	938	675
15H-4, 145–150	136.5	7.23	35.5	557	481	6.971	21.04	50.62	8.23	10.6	263	21.1	979	653
18H-4, 145–150	165.0	7.09	34.5	556	481	6.873	20.61	49.81	8.16	10.6	273	19.2	1010	641
21H-4, 145–150	193.5	7.11	35.2	556	481	6.840	20.04	49.18	8.63	10.4	287	17.8	1090	617
24X-5, 145–150	223.7	7.39	34.3	556	481	6.553	20.01	48.40	9.09	10.1	289	17.4	1220	598
27X-4, 140–150	251.2	7.35	34.5	556	481	5.804	20.36	48.46	9.26	9.9	273	17.0	1140	544
30X-4, 140–150	279.9	7.19	34.5	556	483	5.295	21.86	48.45	9.75	9.7	263	18.9	1230	506
33X-5, 140–150	310.3	7.39	35.0	556	483	4.273	22.17	48.32	10.13	9.7	229	19.6	1360	454
36X-6, 140–150	340.7	7.40	34.5	555	483	3.492	22.80	48.19	10.50	9.7	210	20.0	1290	385
40X-4, 140–150	376.3	7.27	34.2	554	480	2.256	22.80	48.42	11.40	8.1	186	21.1	648	252
41X-4, 140–150	385.9	7.19	34.5	555	482	2.630	23.42	47.91	11.83	7.9	172	22.2	349	281
44X-3, 080–092	412.5	7.34	34.5	550	474	2.335	25.70	49.70	14.14	7.5	164	25.2	398	160
45X-1, 10–15	419.6	7.43	34.5	544	469	**	25.91	49.23	14.53	7.6	162	24.0	458	156

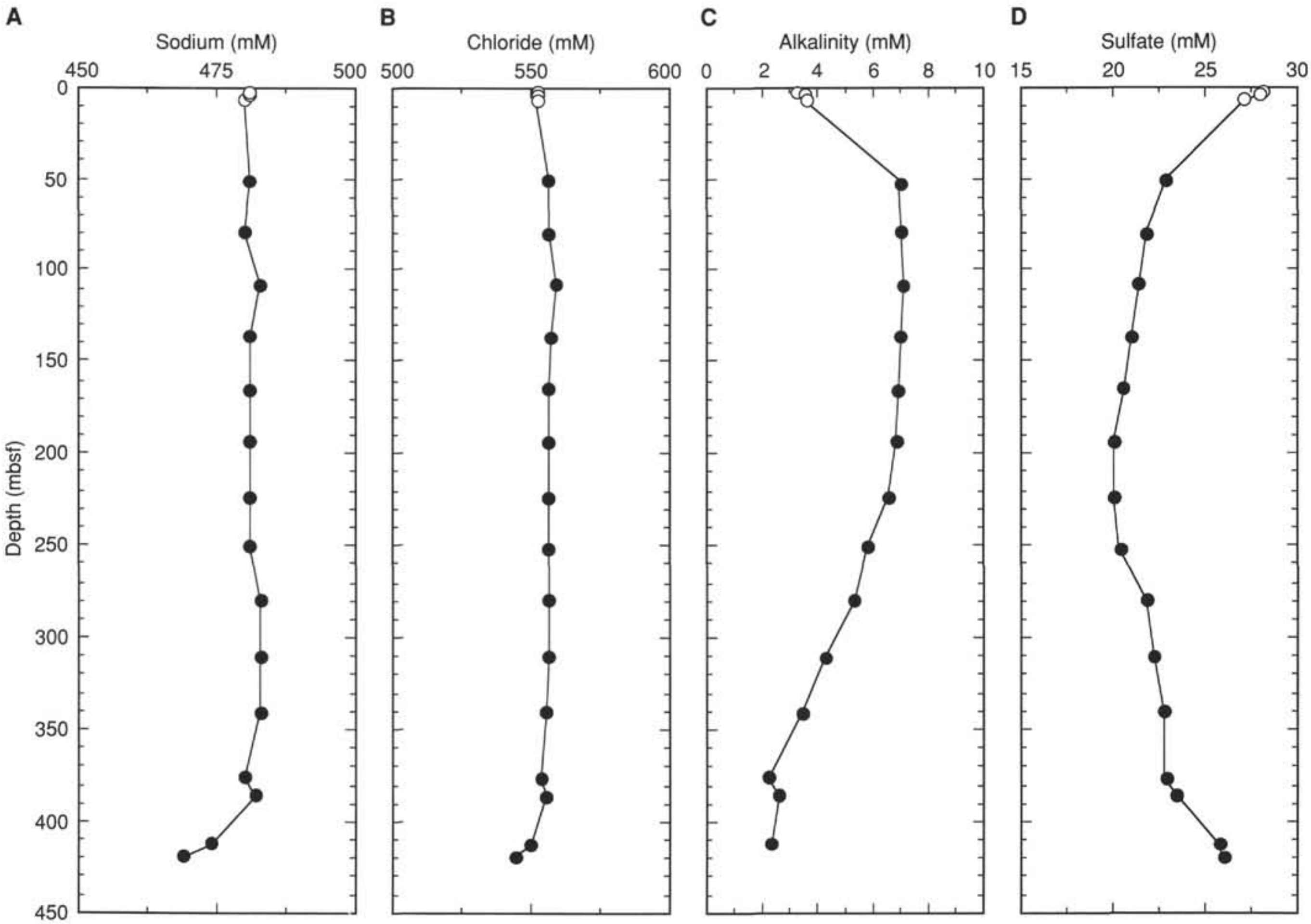

Figure 25. Interstitial-water geochemical data vs. depths (mbsf) for Holes 846A (open circles) and 846C (solid circles). **A.** Sodium. **B.** Chloride. **C.** Alkalinity. **D.** Sulfate.

The occurrence of ammonia at this site (Fig. 26C) is consistent with the record of diagenesis that is reflected in profiles of alkalinity and sulfate. Ammonia levels are highest between 50 and 100 mbsf, coinciding with the highest alkalinities and steepest gradient in sulfate.

One interesting result from this site is the profile of methane with depth (Organic Geochemistry section, this chapter), which is similar to alkalinity and ammonia. Given the observation that methane is produced in these sediments, one might expect high levels of ammonia, as thermodynamics predict ammonia generation by nitrogen fixation after the onset of methane production during metabolic reduction, as outlined out by Claypool and Kaplan (1974).

Magnesium (Fig. 27A) and potassium (Fig. 27C) decrease downhole at this site. Above 400 mbsf, the overall change is 10% in the case of magnesium and 27% for potassium, well outside the precision of these measurements. Overall, these profiles suggest that reaction deep in the sediment column or in basement is acting as a sink for these elements. The potassium profile shows a definite inflection at the top of the chalks that characterize the bottom of this hole (see Lithostratigraphy section, this chapter). The remainder of the potassium profile displays a monotonous decrease with depth, indicating diffusive control. The magnesium profile downhole is distinctly different, having a broad minimum in deeper sections, which might result from incorporation into calcite.

The calcium profile (Fig. 27B) does not show the deep, broad concentration maximum that characterized this profile at the two previous sites. Instead calcium decreases sharply in the top 50 mbsf then increases steadily downcore, with another sharp break near basement. This profile is consistent with the suggestion that basalt alteration can act as a source of calcium to deep-sea sediments (McDuff, 1981).

The interstitial silica profile at this site (Fig. 27D) displays relatively high concentrations in shallow sections with an increasing trend downcore but culminating in a dramatic decrease near basement. There is microscopic evidence for recrystallization at this site (see Biostratigraphy section, this chapter) and this process may explain the gradual increase in dissolved silica downcore (Gieskes, 1974). The sharp decrease below 340 mbsf is associated with the first appearance of chert nodules in Core 138-846B-40X. Similar precipitous gradients in interstitial silica have been recorded above chert layers in other holes, notably by Harrison et al. (1982) at Site 495 during DSDP Leg 67.

Concentrations of interstitial strontium are known to increase during the recrystallization of calcite (Elderfield and Gieskes, 1982). Strontium (Fig. 26B) attains a higher level here than at the previous two sites, apparently in response to the greater abundance of calcium carbonate (see "Organic Geochemistry" section, this chapter) and

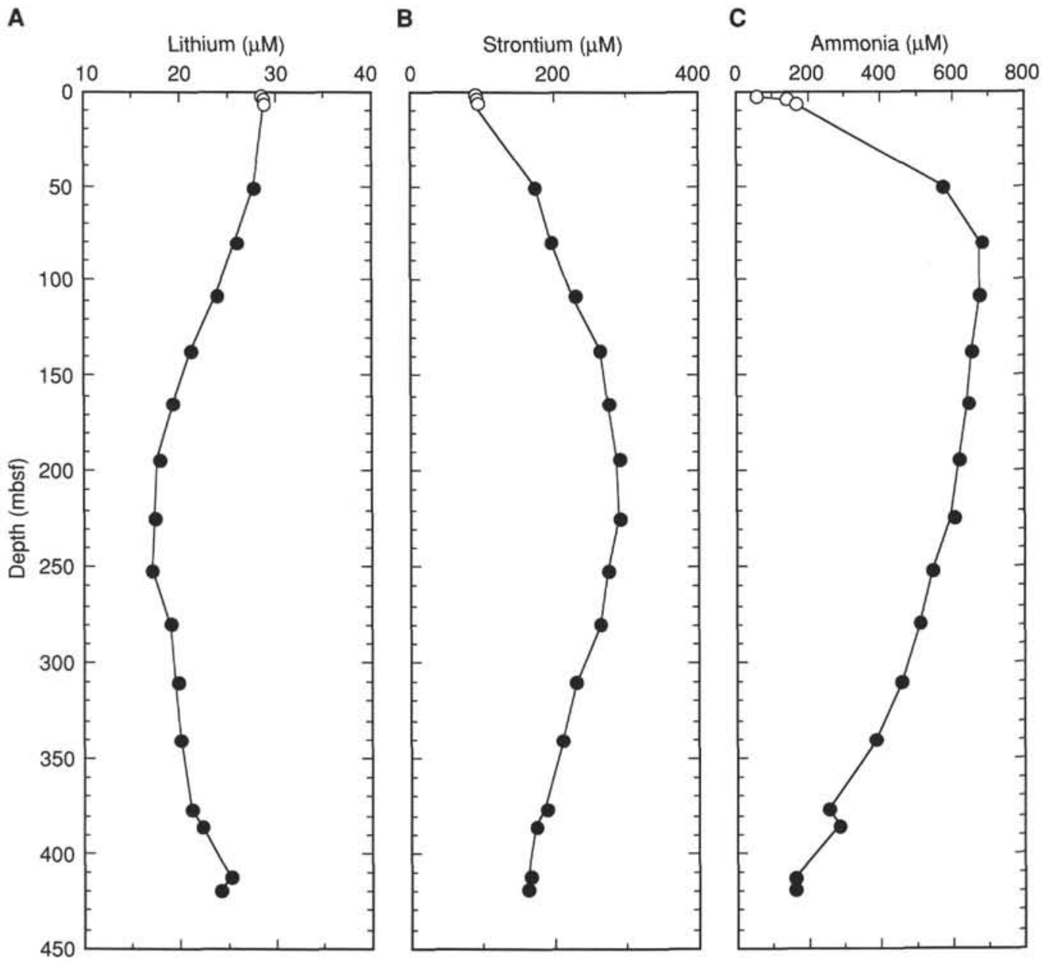

Figure 26. Interstitial-water geochemical data vs. depths (mbsf) for Holes 846A (open circles) and 846C (solid circles). **A.** Lithium. **B.** Strontium. **C.** Ammonia.

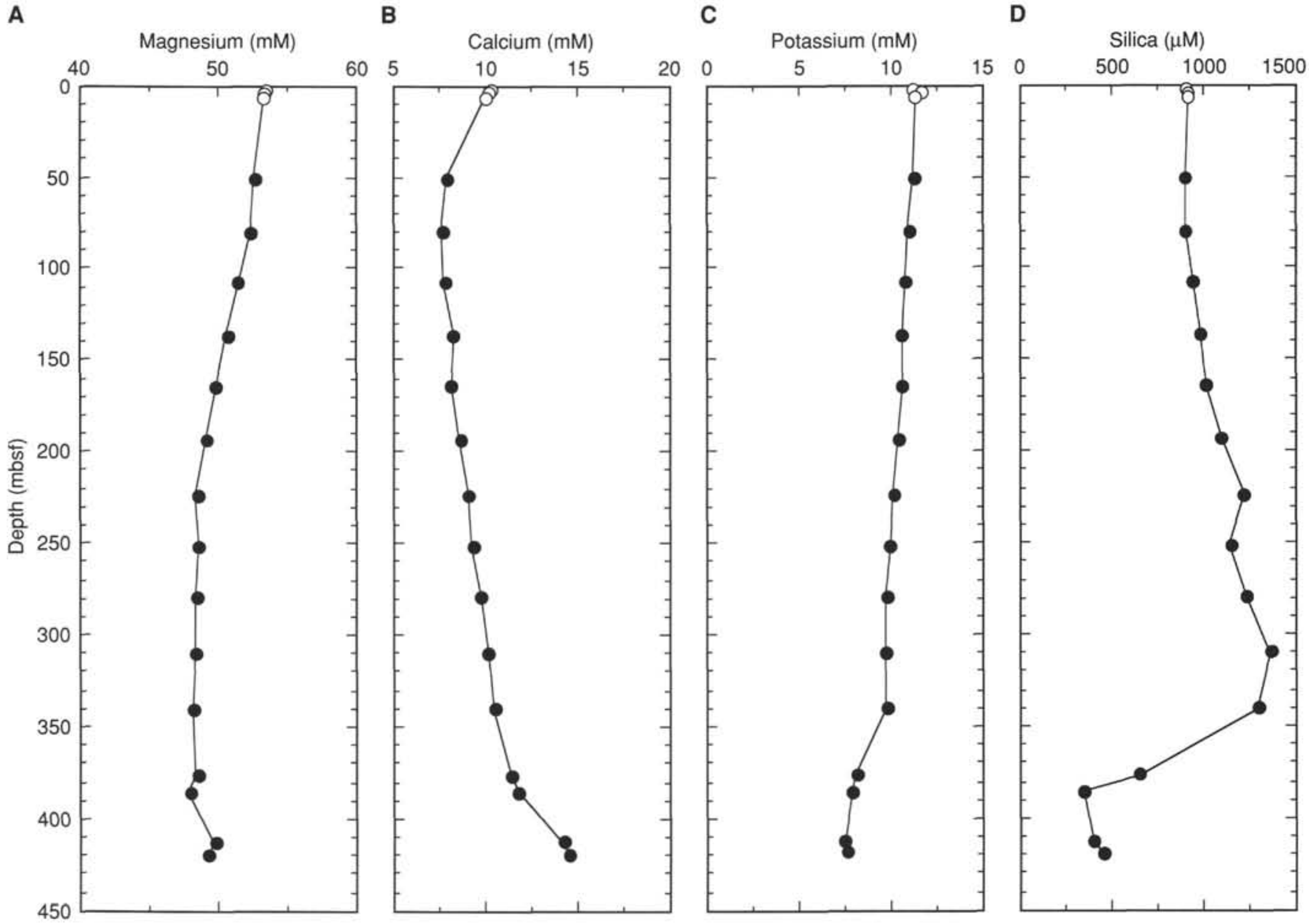

Figure 27. Interstitial-water geochemical data vs. depths (mbsf) for Holes 846A (open circles) and 846C (solid circles). **A.** Magnesium. **B.** Calcium. **C.** Potassium. **D.** Silica.

more extensive recrystallization (see "Biostratigraphy" section, this chapter). Vigorous recrystallization may be driven by the more corrosive nature of the interstitial waters here, but also by higher temperatures (Land, 1980) in the deeper sections of this hole (see "Downhole Measurements" section, this chapter).

Lithium (Fig. 26A) displays a trend opposite to that for strontium, suggesting uptake during the recrystallization process. Lithium returns to a seawater concentration at the bottom of this hole, indicating a possible source near basement.

In summary, diagenesis, recrystallization, and basalt alteration influence the interstitial water chemistry at Site 846. A mildly reducing environment in these sediments is indicated by profiles of alkalinity (Fig. 25C), sulfate (Fig. 25D), ammonia (Fig. 26C), and the smell of H_2S during the recovery of these cores. Calcium (Fig. 27B), silica (Fig. 27D), and strontium (Fig. 26B) indicate ongoing recrystallization at this site, at least in the Miocene sections. Alteration of basement rocks are influencing the profiles of magnesium, calcium, potassium, silica, lithium and strontium, to varying degrees. Interstitial silica decreases dramatically at the first appearance of chert.

ORGANIC GEOCHEMISTRY

Carbonate and Organic Carbon

Concentrations of inorganic carbon, total carbon, and total nitrogen were measured in samples from Hole 846B. From these measurements, we calculated the weight percentages of calcium carbonate (%$CaCO_3$) and organic carbon (%C_{org}). The analytical methods are outlined in the "Explanatory Notes" chapter (this volume). The analytical results for each chemical index in each sample (reported as means of several measurements, where applicable) are listed in Table 10 (CD-ROM, back pocket) with respect to both ODP depth (mbsf) and to composite depth (mcd; see "Sedimentation Rates" section, this chapter). Duplicate %$CaCO_3$ analyses of aliquots from the same sample show that, on average, the values are reproducible to within 0.8% (Table 11). Figure 28 depicts %$CaCO_3$ and %C_{org} in Hole 846B vs. ODP depth. Figure 29 uses composite depth and age assignments (see "Sedimentation Rates" section, this chapter) to show the temporal variability of %$CaCO_3$ and %C_{org}.

The lithologic sequence recovered at Site 846 was subdivided into two lithologic units (see "Lithostratigraphy" section, this chapter). Unit I (Cores 138-846B-lH to -34X-4, 110 cm) is composed of nannofossil ooze and siliceous-microfossil-rich sediments and is subdivided into two subunits. The average %$CaCO_3$ in Subunit IA (Cores 138-846B-IH to -28X-6, 30 cm) is 59.1% and ranges from 14.4% to 85.8%. Organic carbon concentrations average 0.5% and range from zero to 2.0%. Figure 28 clearly shows the gradual increase in C_{org} in the upper Pliocene to Pleistocene sediments of Subunit IA, from values below 0.5% to values around 1%.

In Subunit IB (Cores 138-846B-28X-6, 30 cm, to -34X-4, 110 cm) %$CaCO_3$ decreases downhole and is highly variable, with a range from 0% to 79.5%. The distinctly low %$CaCO_3$ values below 290 mbsf coincide with a marked increase in siliceous (radiolarian and diatom)

Table 11. Duplicate analyses of percentage of $CaCO_3$ in samples from Site 846.

Core, section, interval (cm)	ODP depth (mbsf)	Composite depth (mcd)	First run $CaCO_3$ (%)	Second run $CaCO_3$ (%)	Third run $CaCO_3$ (%)	Absolute value of $CaCO_3$ (difference)
138-846B						
1H-1, 104–106	1.05	1.05	61.67	59.75		1.92
1H-3, 104–106	4.05	4.05	29.50	29.50		0.00
1H-4, 145–150	5.98	5.98	57.09	57.34		0.25
2H-4, 145–150	12.98	13.58	77.01	77.17		0.17
3H-4, 145–150	22.48	24.53	59.09	60.00		0.92
4H-3, 103–105	30.04	33.19	78.59	77.51		1.08
4H-4, 145–150	31.98	35.13	60.92	63.51		2.58
6H-4, 140–145	50.93	57.43	42.34	41.75		0.58
7H-4, 145–150	60.48	68.78	21.00	20.84		0.17
8H-4, 145–150	69.98	79.68	37.50	37.42		0.08
9H-4, 140–145	79.43	89.58	59.42	58.34		1.08
10H-2, 53–55	85.04	97.59	20.50	20.42		0.08
10H-2, 114–116	85.65	98.20	58.17	60.09		1.92
10H-5, 147–150	90.49	103.04	40.59	41.00		0.42
11H-4, 100–102	98.01	111.51	33.34	32.75		0.58
11H-4, 145–150	98.48	111.98	61.68	62.00		0.33
12H-4, 140–145	107.93	122.73	48.59	47.75		0.83
13H-4, 145–150	117.48	133.93	46.92	45.75		1.17
14H-4, 145–150	126.98	144.13	71.34	72.84		1.50
15H-2, 124–126	133.25	152.95	34.42	34.42		0.00
15H-3, 102–104	134.53	154.23	59.17	59.42		0.25
15H-4, 145–150	136.48	156.18	23.09	22.25	24.09	1.83
16H-4, 145–150	145.98	166.18	80.26	78.76		1.50
17H-3, 22–24	152.73	173.98	45.50	45.59		0.08
17H-3, 102–104	153.53	174.78	65.92	68.17		2.25
17H-4, 145–150	155.48	176.73	68.84	67.84		1.00
17H-5, 104–106	156.55	177.80	44.00	44.42		0.42
18H-4, 145–150	164.98	186.83	79.76	79.67		0.08
19H-4, 140–145	174.43	198.23	76.42	77.17		0.75
20H-4, 145–150	183.98	209.58	37.75	36.00	36.75	1.75
21H-4, 140–145	193.43	220.38	70.51	71.01		0.50
22H-4, 145–150	202.98	233.43	72.76	73.01		0.25
23X-4, 145–150	212.48	246.48	74.67	74.76		0.08
24X-4, 145–150	222.18	257.58	68.51	67.17		1.33
27X-4, 140–145	251.13	286.23	69.26	68.76		0.50
28X-4, 145–150	260.88	295.98	65.92	65.09		0.83
28X-5, 103–105	261.94	297.04	83.09	81.92		1.17
28X-6, 103–105	263.44	298.54	29.59	27.84		1.75
29X-4, 145–150	270.18	305.28	21.67	21.75		0.08
29X-6, 63–65	272.34	307.44	77.67	77.92		0.25
30X-2, 135–137	276.76	311.86	17.33	17.67		0.33
30X-4, 135–140	279.78	314.88	38.34	37.34		1.00
30X-5, 29–31	280.20	315.30	16.83	18.42		1.58
31X-4, 145–150	289.48	324.58	32.84	32.59		0.25
32X-4, 145–150	299.08	334.18	9.33	9.33		0.00
32X-6, 29–31	300.90	336.00	1.75	1.50		0.25
33X-2, 33–35	304.64	339.74	0.08	0.00		0.08
33X-4, 145–150	308.78	343.88	27.00	28.00		1.00
33X-6, 32–34	310.63	345.73	44.34	43.67		0.67
34X-4, 145–150	318.38	353.48	50.00	50.09		0.08
35X-4, 145–150	327.98	363.08	62.59	62.25		0.33
36X-4, 145–150	337.68	372.78	76.26	75.59		0.67
37X-2, 145–150	344.28	379.38	77.51	76.34		1.17
38X-4, 145–150	356.98	392.08	79.26	77.51		1.75
40X-4, 135–140	376.18	411.28	76.84	75.67		1.17
41X-1, 1024–104	380.93	416.03	90.92	90.34		0.58
41X-3, 115–117	384.06	419.16	88.59	87.67		0.92
41X-4, 135–140	385.78	420.88	87.34	86.67		0.67
42X-1, 113–118	390.76	425.86	82.51	82.26		0.25
44X-1, 120–125	410.13	445.23	63.17	61.92		1.25
45X-1, 15–16	418.76	453.86	67.42	67.17		0.25
Average						0.76

oozes. Organic carbon concentrations were determined in the low $\%CaCO_3$ interval near 300 mbsf and average 0.4% with a high of 1.1%, values similar to those found in Subunit IA.

Lithologic Unit II (Cores 138-846B-34X-4, 110 cm, through 45X-1, 63 cm) is primarily composed of nannofossil oozes and chalks. Percent $CaCO_3$ in the two subunits in Unit II averages 67% and 75.5%, respectively. In this carbonate-rich interval, C_{org} could not be measured with confidence by shipboard techniques. As such, $\%C_{org}$ data from this unit are excluded from Table 10.

Accumulation Rates and Comparison with Sites 844 and 845

Following the methodology outlined in the Explanatory Notes (this volume), we calculated the average values of several sedimentary parameters ($\%CaCO_3$, $\%C_{org}$, LSR, DBD) in the 10 time intervals delimited by the chronostratigraphic levels discussed in the Sedimentation Rates section, this chapter. The average values of $\%CaCO_3$, $\%C_{org}$, linear sedimentation rate (LSR), dry-bulk density (DBD), bulk-sediment mass accumulation rate (bulk MAR), $CaCO_3$ MAR, and C_{org} MAR for the 10 time intervals between 0 and 16 Ma are listed in Table 12. The mean values are presented in Figures 30 and 31. Superimposed on the mean values are estimates of the instantaneous MAR calculated for each sample. Mean bulk sediment MAR at Site 846 have a distinctly different pattern from those at Sites 844 and 845. At Site 846, bulk-sediment accumulation rates in the middle Miocene are three to four times lower than the rates at Site 844 and 845. A second difference is that the $CaCO_3$, non-$CaCO_3$, and bulk sediment MAR's increase from the Miocene to the Pliocene at Site 846 while the opposite is true at Sites 844 and 845. Not all MAR records differ among the two regions. The C_{org} MAR at Sites 844 through 846 increases over the interval from 9 Ma to the present. While a dramatic decrease in $CaCO_3$ was observed near 10 Ma at these sites, the amplitude and the timing of the response differs significantly.

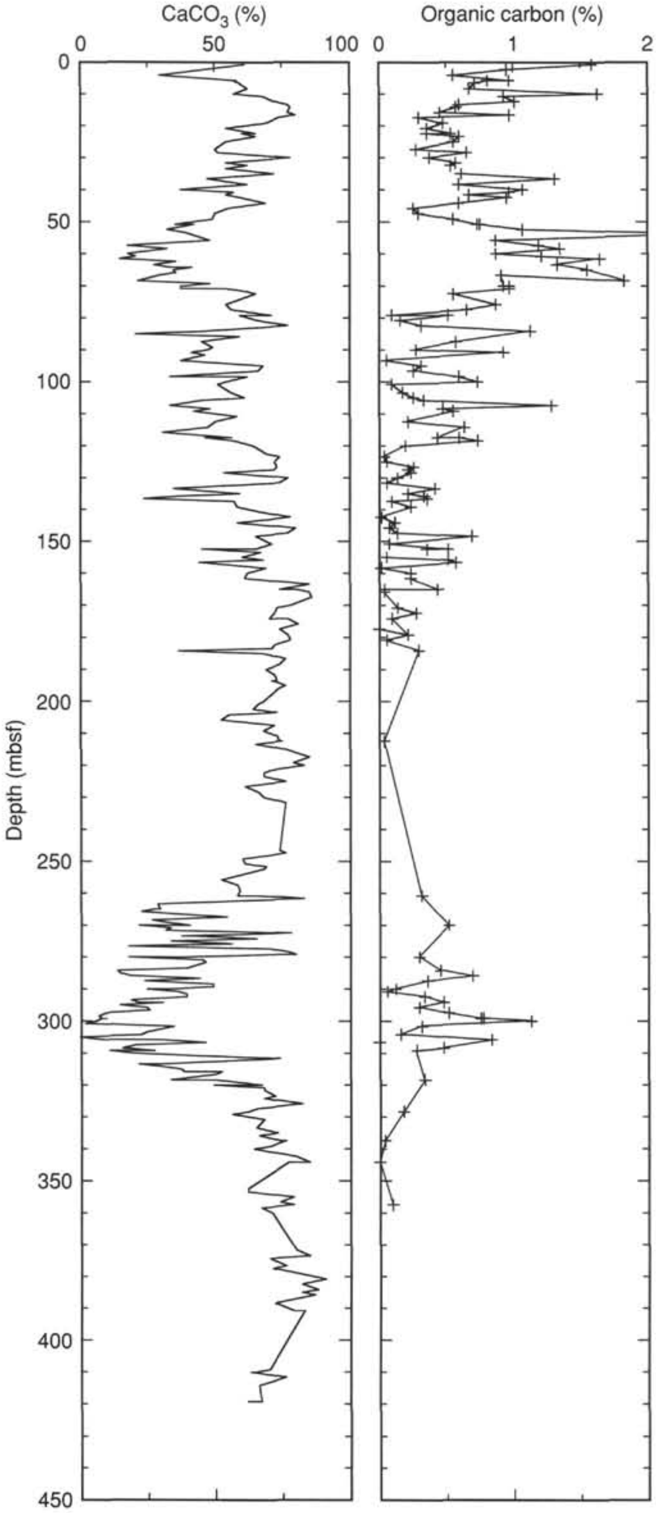

Figure 28. Downhole records of percentages of $CaCO_3$ and C_{org} vs. ODP depth (mbsf). Data from Hole 846B.

Gas Geochemistry

Samples for gas analysis were taken from each core of Hole 846B. Gas was released from a plug of sediment (about 5 cm^3) by thermal desorption (see "Explanatory Notes" chapter, this volume). The concentrations of hydrocarbons in the headspace volume, measured vs. known standards (in ppm), were converted to µL/L of sediment and are reported in Table 13 (CD-ROM, back pocket) and shown graphically in Figure 32. The first occurrence of methane is noted at 10 mbsf. Concentrations rise until they reach a maximum of 130 µL/L at 150 to 200 mbsf, after which they decline to 10 µL/L at the bottom of Hole 846B. Ethane or other hydrocarbon gases are either absent or below detection limits.

While the concentration of methane is relatively low, never exceeding 140 µL/L, its variation throughout Hole 846B is geochemically important. Methane first appears with the onset of sulfate reduction (Fig. 32), as indicated by a decrease in interstitial sulfate and a concomitant increase in alkalinity and ammonia (see "Inorganic Geochemistry" section, this chapter). Furthermore, sediments between 10 and 200 mbsf are characterized by a distinct smell of hydrogen sulfide. At 200 mbsf, sulfate concentrations in the pore waters begin to increase again to attain values almost as high as those in seawater. Coincident with the downhole increase in sulfate, methane concentration declines. The observed correspondence between the behavior of methane and other parameters characterizing biogeochemical diagenesis in the sediments implies that the methane encountered at Site 846 is of microbial origin.

In Figure 32, concentrations of methane are compared to concentrations of C_{org} measured in the sediment split used for gas determination. The lack of correlation between the amounts of desorbed gas and the amount of C_{org} suggests that concentration of C_{org} is not necessarily a limiting factor for microbial methane production under the conditions encountered at Site 846 and that the contribution of methane originating from thermal rupture of C-C bonds (catagenic methane) by the method employed here is negligible.

The formation of methane by microbial activity along with sulfate reduction at Site 846 contrasts with the general belief that methane formation during diagenesis starts only after interstitial sulfate concentrations have been almost exhausted (e.g., Claypool and Kaplan, 1974). In other studies, methane found in sediments within the zone of sulfate reduction has been attributed to methane leaking or migrating from underlying, more reducing strata. Clearly, this is not the case at Site 846, where sulfate reduction decreases downhole and interstitial sulfate levels increase below the interval of methane occurrence.

Paleotemperature Reconstructions at Site 846 Based on the $U^{K'}_{37}$ Index

Accumulation rates reconstructed for the late Pliocene to Pleistocene age interval at Site 846 are generally higher and more variable than those at Sites 844 and 845. While the latter sites may have recorded an increase in organic carbon accumulation toward the present that is consistent with plate movement underneath the equatorial high-productivity zones, the accumulation rates at Site 846 may indicate changes in paleoceanographic conditions. To narrow down the choices, among which may be the variable influence of the Peru Current and the equatorial divergence, we investigated the ratio of two biomarkers in lipid extract from sediments of Site 846. For the analytical procedures, see the "Explanatory Notes" chapter (this volume).

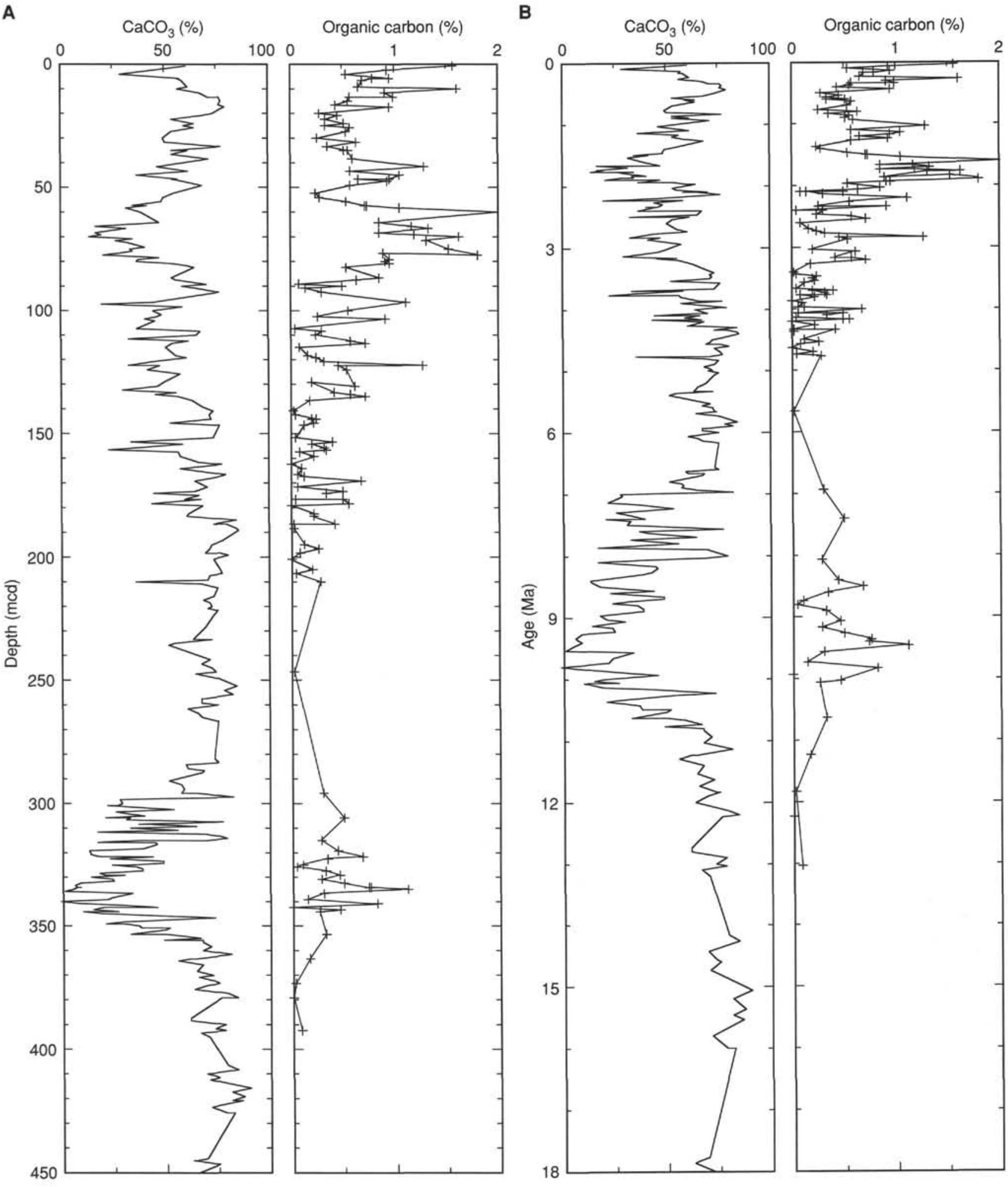

Figure 29. Plots of percentages of $CaCO_3$ and C_{org} vs. composite depth (**A**) and age (**B**). Data from Hole 846B.

The ratio of the tri- and di-unsaturated long-chain ketones ("alkenones") has emerged in recent years as a promising tool for reconstructing sea-surface temperatures. The ketones with 37 carbon atoms are thought to be exclusive products of prymnesiophyte algae and are produced in variable ratios to ensure cell membrane fluidity at variable ambient water temperatures. The ratio of the di- to the tri-unsaturated ketone has been defined as the $U_{37}^{K'}$ index (Brassell et al., 1986) and has been calibrated to ambient temperature in growth experiments with high accuracy (Prahl et al., 1988). Furthermore, the ketone signal appears to be resistant to diagenetic overprinting (e.g., Prahl et al., 1989). An extensive listing of available literature is given in Marlowe et al. (1990).

Table 12. Average value of sedimentary parameters calculated over time intervals defined by chronostratigraphic levels.

Composite depth (mcd)	Age (Ma)	Mean $CaCO_3$ (%)	Mean C_{org} (%)	Mean sed. rate (m/m.y.)	Mean DBD (g/cm^3)	Mean Bulk MAR (g/cm^2/k.y.)	Mean CaCO3 MAR (g/cm^2/k.y.)	Mean non-CaCO3 MAR (g/gm^2/k.y.)	Mean Corg MAR (mg/gm^2/k.y.)
0	0.00								
		60.91	0.71	40.04	0.51	2.06	1.26	0.81	14.70
44.85	1.12								
		50.37	0.68	32.76	0.47	1.55	0.78	0.77	10.48
59.92	1.58								
		42.94	0.89	58.95	0.42	2.50	1.07	1.43	22.12
108.85	2.41								
		55.79	0.38	32.96	0.56	1.85	1.03	0.82	7.06
146.75	3.56								
		66.98	0.22	51.73	0.71	3.68	2.47	1.22	8.12
220.20	4.98								
		67.80	0.17	39.26	0.71	2.80	1.90	0.90	4.89
299.50	7.00								
		32.56	0.50	14.59	0.50	0.73	0.24	0.49	3.66
306.65	7.49								
		32.49	0.44	14.53	0.47	0.68	0.22	0.46	2.98
342.25	9.94								
		56.89	0.20	16.25	0.63	1.03	0.59	0.44	2.06
400.10	13.50								
		79.74		10.38	1.03	1.07	0.85	0.22	
426.06	16.00								

Note: After this table was constructed on board the ship, depths of the age control points were changed (see "Sedimentation Rates" section, this chapter, for final selection of age control points). These changes in depth were often minor (less than 5 m). None were incorporated in this table, nor in the accompanying Figures 29 through 31.

DBD = dry bulk density; MAR = mass accumulation rate.

A prominent species known to produce the ketones is the ubiquitous *Emiliania huxleyi,* which appeared in the fossil record at around 0.28 Ma and which is the species used in laboratory calibration experiments of the $U^{K'}_{37}$ index. There has been some disagreement over the significance of the $U^{K'}_{37}$ index in sediments predating the FAD of *E. huxleyi*, and the question is as yet unresolved. We decided to take a leap of faith in tentatively translating the $U^{K'}_{37}$ index of sediment extracts older than 0.28 Ma to sea-surface temperatures based on calibration with *E. huxleyi* on the basis that the components may be restricted to a single family of prymneiophyte algae and that they most certainly had the same physiologic function in the ancestral phylogenetic lineage (Marlowe et al., 1990). One challenge of post-cruise research of Leg 138 will be to compare different approaches to paleotemperature reconstructions and to assess the validity of the ketone methods in older sediments.

Table 14 (CD-ROM, back pocket) lists all results of the ketone analyses, %Corg, $\%CaCO^3$, age estimates for individual samples, based on composite depth and linear interpolation between chronostratigraphic levels and the calculated values of the $U^{K'}_{37}$ index and corresponding estimates of sea-surface temperature (SST). Concentrations of the dominant di-unsaturated alkenone (i.e., heptatriaconta-15E,22E-dien-2-one) range between 100 and 2900 ng/g dry weight. The tri-unsaturated alkenone (i.e., heptatriacontae-15E-22E-trien-2-one) ranges from 9 to 1000 ng/g dry weight. Neither compound shows any relationship to either %Corg or $\%CaCO^3$. The $U^{K'}_{37}$ (Fig. 33) index ranges from 0.75 to 0.93, which corresponds to SST estimates of 20.9° and 26.2°C, respectively. The range of these values is significantly above the estimated error from duplicate analyses (standard deviation of 0.4°C, $n = 9$; see Table 14, CD-ROM, back pocket) and falls well within the range of present-day SST observations. At about 0.3 Ma (Fig. 33), the range of the ratio is between 0.74 and 0.93, which translates to temperatures between 21° and 26°C, based on the calibration of Prahl et al. (1988). At about the 0.3 Ma interval, we observed a sharp decrease in the index that indicates significantly lower SSTs at a time corresponding to the well-known mid-Brunhes Event, which in our record marks the upper (and coldest) end point of a long-term cooling trend that began around 0.65 Ma. The temperature decreases from approximately 25°C at about 0.65 Ma to 21°C at 0.3 Ma, with little variability in our widely spaced record. From about 0.65 to about 0.95 Ma, the $U^{K'}_{37}$ values decreased steadily to an inferred SST of about 22°C. Between 0.9 and 1.2 Ma, another significant change occurs in the record; $U^{K'}_{37}$ values increase sharply by approximately 3°C.

PHYSICAL PROPERTIES

Introduction

A complete suite of physical property measurements was performed on cores from Site 846. For whole-round sections, GRAPE-density, compressional-wave velocity (using the multisensor track, MST), and thermal conductivity were measured. On split cores, wet-bulk density, dry-bulk density, grain density, porosity, wet- and dry-water contents, and void ratio were measured. Vane shear strength and compressional-wave velocity measurements were also made on split cores. The digital sonic velocimeter (DSV) was employed for discrete velocity measurements on split cores.

Physical properties were measured in every section of cores recovered from Hole 846B, except for core catchers and some short sections. Velocity and index properties were measured twice per section, and shear strength was measured once per section in Hole 846B. In Hole 846C, velocity and index properties were measured once per section, and shear strength and thermal conductivity were not measured. Index property samples were always taken at the same depth interval as the velocity measurements. Thermal conductivity was routinely measured for Sections 2 and 5 of each core in Hole 846B. Results of the physical properties at Site 846 are listed in Tables 15 to 18 (CD-ROM, back pocket) and shown graphically in Figures 34 through 40.

Index Properties

Wet-bulk density generally increases with depth (Fig. 34; Table 15, CD ROM, back pocket). Although two prominent lows occur at 60 and 300 mbsf, the overall trend reflects the results of simple mechanical compaction and diagenesis. The profile, however, correlates fairly well with that of the percentage calcium carbonate profile (see "Organic Geochemistry" section, this chapter). In some cases, even high-frequency variations coincide. Dry-water content generally decreases with depth, but two significant increases were recorded at 60 and 300 mbsf (Fig. 35; Table 15, CD ROM). Grain density varies between 2.04 and 2.79 g/cm^3, with most values ranging between 2.30 and 2.70 g/cm^3 (Fig. 36; Table 15, CD ROM). Two intervals, one centered at 50 to 70 mbsf and another at 250 to 320 mbsf, have

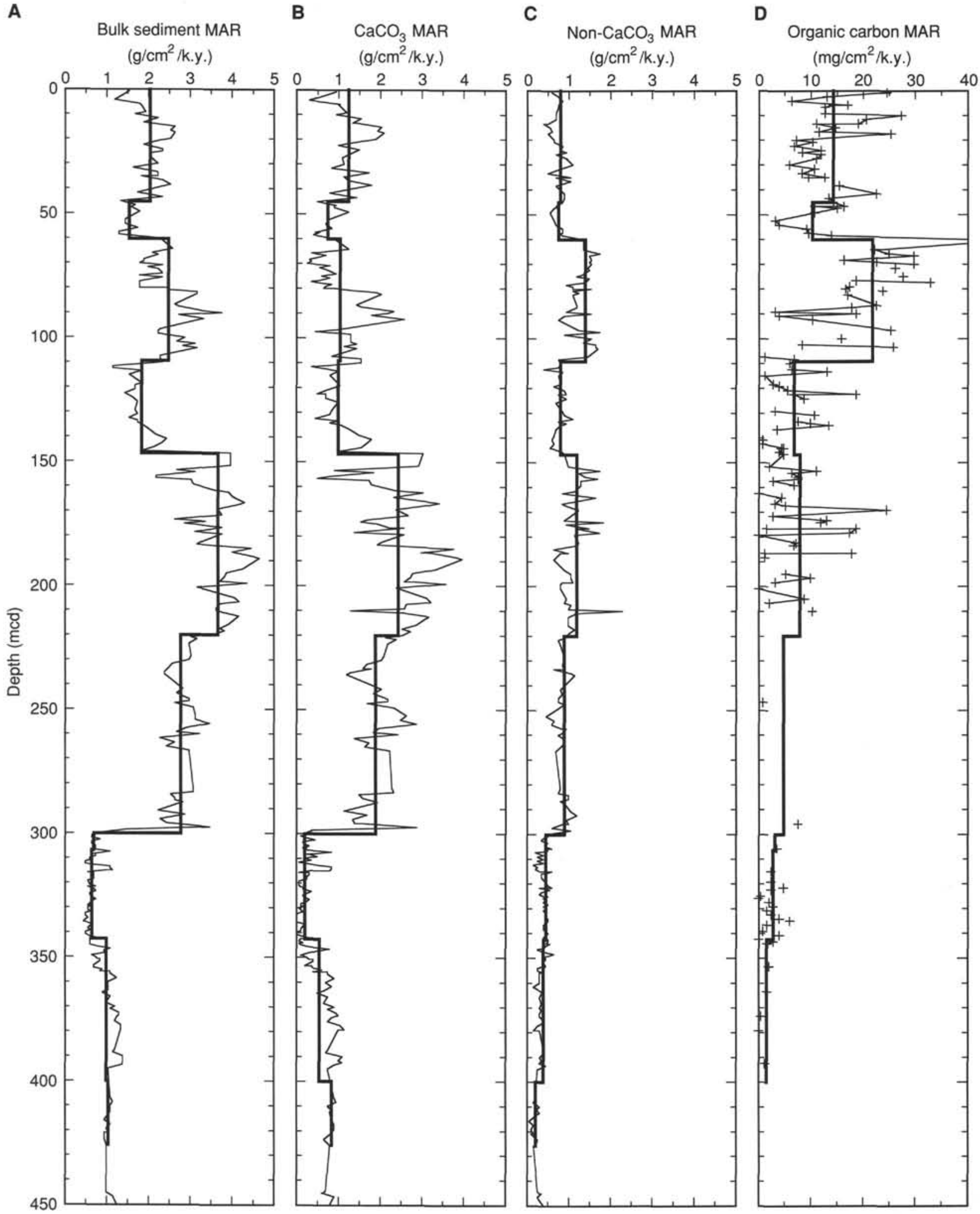

Figure 30. Mass accumulation rates of bulk sediment (**A**), $CaCO_3$ (**B**), non-$CaCO_3$ (**C**), and C_{org} (**D**) sedimentary components vs. composite depth at Site 846. Note different units for C_{org}. Thick line is the mean value between each stratigraphic datum plane; thin line shows discrete accumulation rates calculated for each sample.

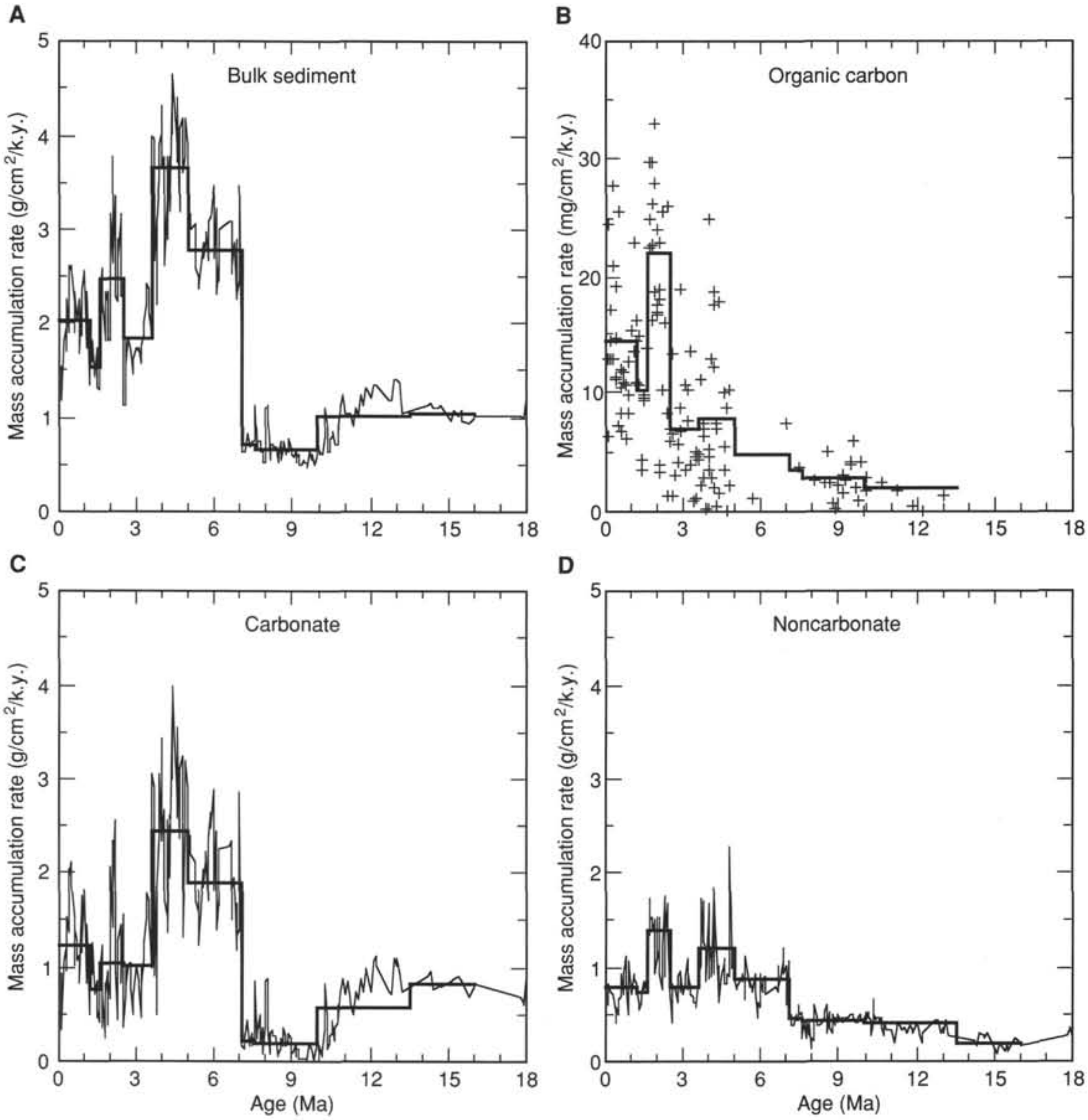

Figure 31. Accumulation rates vs. age in sediments from Site 846. **A.** Bulk sediment. **B.** C_{org}. **C.** $CaCO_3$. **D.** Non-$CaCO_3$. Thick line is the mean value between each stratigraphic datum plane; thin line shows discrete accumulation rates calculated for each sample (In Fig. 31B, the thin line has been omitted for clarity).

distinctly lower grain densities. Porosity generally decreases with depth (Fig. 37; Table 15, CD ROM), but two significant increases are centered at 50 and 300 mbsf.

Compressional-Wave Velocity

Compressional-wave velocity was measured parallel to the core axis on split cores from Holes 846B and 846C (Fig. 38; Table 16, CD ROM, back pocket). Velocity generally increases with depth from 1490 to 1520 m/s. Distinct offsets (increases) in velocity, however, occur around 60 and 280 mbsf, the same depth intervals where anomalous trends are seen in the downhole profiles of all the index properties. Below 370 mbsf velocity increases rapidly with depth toward the basement, corresponding to the lithologic transition from ooze to chalk.

Shear Strength

The profile of undrained shear strength for Hole 846B is presented in Figure 39 (Table 17, CD ROM, back pocket). The values range between 6.8 and 156.9 kPa and generally increase with depth. Prominent peak strength values occur at 203–207 mbsf, 272–283 mbsf, and 312–322 mbsf. The peak values correspond to intervals with high diatom concentrations (40%–60%) (see "Biostratigraphy" section, this chapter). The interlocking structure of the siliceous tests results in higher shear strength values than found in carbonate oozes.

Thermal Conductivity

Thermal conductivity (Fig. 40; Table 18, CD ROM, back pocket) varies from 0.78 to 1.25 W/(m • K) and generally increases down-

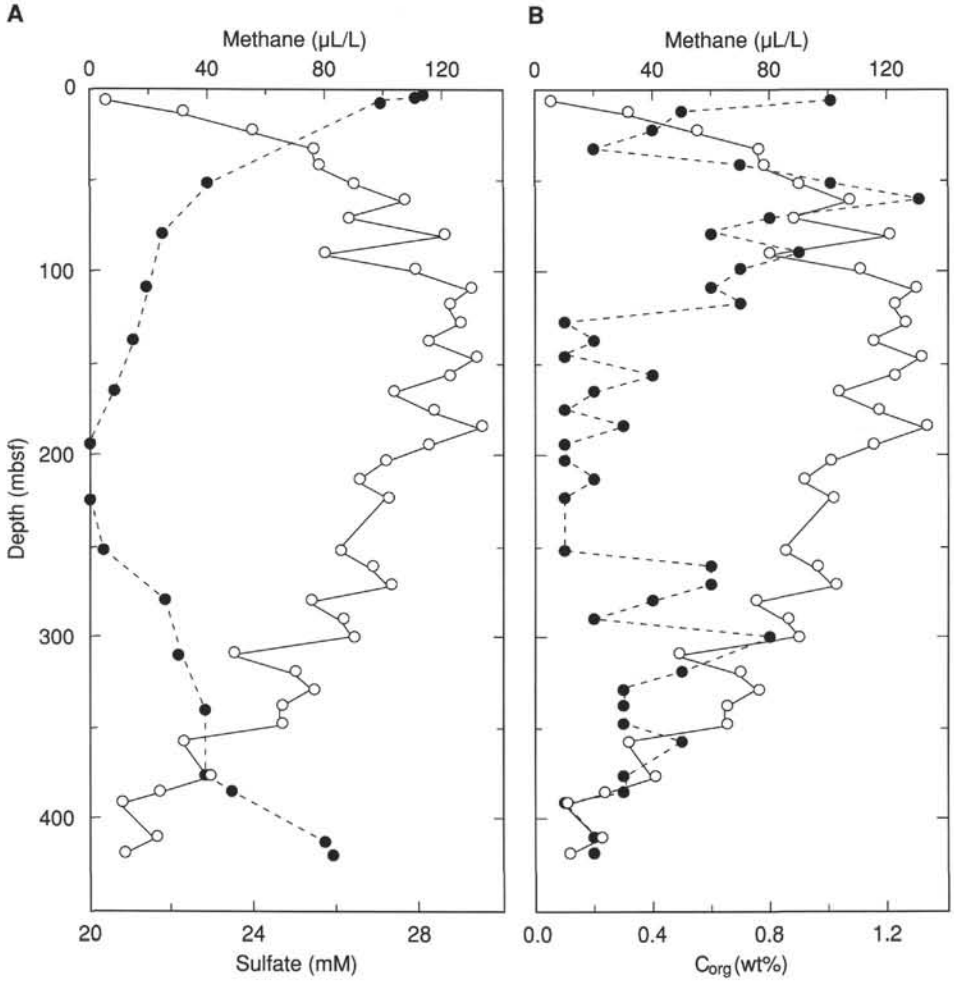

Figure 32. **A.** Variation of methane concentration (open circles) and sulfate concentrations in pore waters (black dots) vs. depth in Hole 846B. **B.** Concentrations of methane (open circles) and C_{org} (black dots) in the headspace samples from Hole 846B.

hole, corresponding to decreasing porosity. Thermal conductivity is mainly determined by water content (Bullard, 1963), and thus comparable profiles can be seen in the index properties such as wet-bulk density, porosity, and dry-water content.

Relationships of Physical Properties to Lithology

In general, wet-bulk density, compressional-wave velocity, thermal conductivity and shear strength increase downhole, while porosity and water content decrease. These downhole profiles in the physical property data generally reflect the effects of simple mechanical compaction and diagenesis. Superimposed on this downhole trend is the effect of varying lithology. The lower values in grain density and wet-bulk density (and concomitant increases in porosity and water content) centered at 60 and 280 mbsf reflect intervals highly enriched in siliceous microfossils. The interlocking nature of these siliceous tests supports a higher porosity at depth as compared to carbonate oozes. This interlocking structure is also reflected in higher shear strength values at these depths. Most of the higher frequency (decimeter to meter-scale) variability in the downhole profiles results from alternations between more calcareous-rich and more siliceous-rich sediments.

DOWNHOLE MEASUREMENTS

Quality of Data

Table 19 lists the usable log intervals recorded in Hole 846B. The data collected are of high quality for the entire hole. We were unable to identify any bad data intervals for bulk density, and only two bad intervals in the sonic log: from 278.2–278.7 mbsf and 281–281.5 mbsf. For the most part, the quality of FMS data is good below 125 mbsf. Above this depth, the hole widens beyond the pad extension of the FMS. Only two of the four pads were in contact with the borehole wall over this interval. In addition, poor FMS pad contact was found every 9.5 m between 180 and 230 mbsf, where the borehole had been damaged by coring. Figure 41 shows the hole width from the two FMS calipers over this interval and illustrates where the calipers periodically reach their maximum extension of about 15.2 in.

Logging Units

We divided the sediment section at Site 846 into three log stratigraphic units on the basis of the physical and geochemical logs. These units primarily represent lithologic features, as can be discerned by comparison with the lithologic units (see "Lithostratigraphy" section,

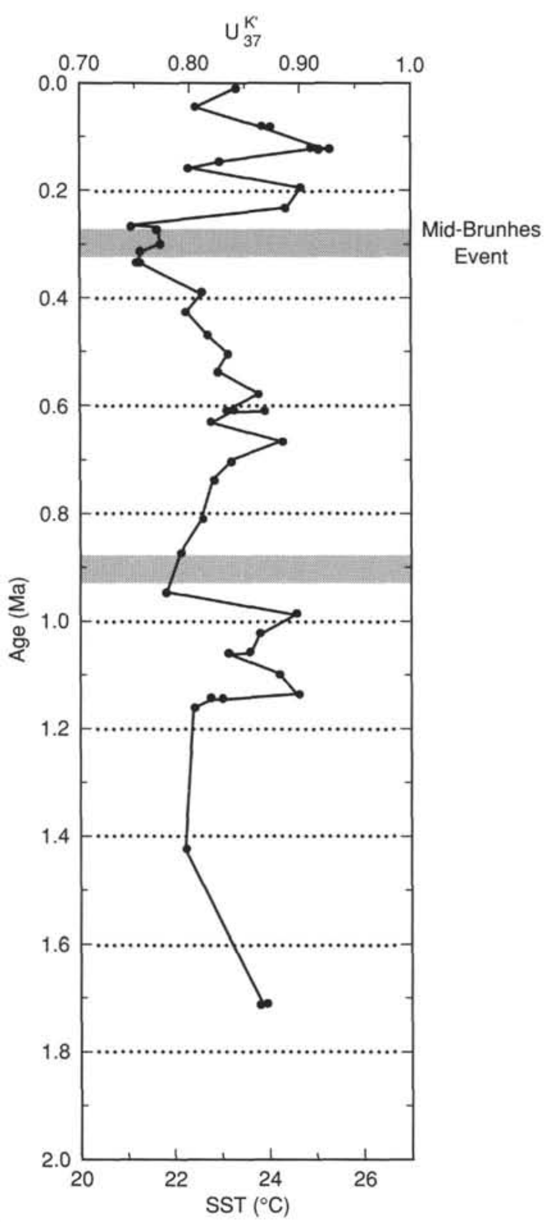

Figure 33. Variations in $U_{37}^{K'}$ index and calculated sea-surface temperatures vs. age, based on samples from Site 846.

this chapter). The division between Subunits A and B in log stratigraphic Units 1 and 3 is diagenetic in nature and is included because of its effects upon the physical properties of the sediments.

Log Stratigraphic Unit 1 (0–262 mbsf; 0–7 Ma)

This unit is marked by flat profiles of density, resistivity, and velocity relative to the rest of the hole (Fig. 42), and it has been divided into two subunits at 206 mbsf to reflect a substantial increase of sonic velocity below this depth. The subunit boundary also coincides with the depth of refusal for APC-coring and the beginning of XCB-drilling. The velocity change primarily marks a lithification event associated with diagenesis and is not a change in sediment type. All indications from the chemical logs (Fig. 43) indicate that the sediment composition is the same across the subunit boundary.

Log Stratigraphic Unit 2 (262–320 mbsf; 7.0–10.5 Ma)

Log stratigraphic Unit 2 is marked by low density, low velocity, and low resistivity values (Fig. 42). The chemical logs show that the interval has high Si and low Ca yields; it is also enriched in aluminosilicate-associated elements, such as iron (Fig. 43), aluminum, and potassium. The lithologic description (see "Lithostratigraphy" section, this chapter) indicates that this interval is diatom-rich. The low density, velocity, and high porosity (low resistivity) values are typical of diatom-rich sediments, and the chemical logs indicate that log stratigraphic Unit 2 is an opal- and clay-rich interval.

Log Stratigraphic Unit 3 (320 mbsf–base of hole; 10.5 Ma–about 17 Ma)

Log stratigraphic Unit 3 is marked by increases of all the physical properties and by high Ca yields in the geochemical logs. We have subdivided the unit into two subunits at 360 mbsf, where cherts appear, and where chalks are found below. The subunit division, as in log stratigraphic Unit 1, marks a diagenetic change in the sediments. The diagenesis is somewhat different between the two units, however. In log stratigraphic Unit 1, there appears to be only minor cementation and lithification, sufficient only to affect the velocity logs. In log stratigraphic Unit 3, the diagenetic change is marked by steps in resistivity, velocity, and density (Fig. 42). Extensive dissolution and reprecipitation are needed to cause such changes. Included in Logging Unit 3 are the basal Fe-rich hydrothermal precipitates, shown by the ramp-like increase in Fe content (Fig. 43).

Comparison of Laboratory-Measured Density with Logging Data

We observe a general agreement between the discrete gravimetric bulk density measurements and those from the downhole logging but note a slight offset between the two data sets (Fig. 44). To compare the two different data sets, we used the inverse signal-correlation program CORPAC (Martinson et al., 1982) to get a mapped depth scale between log and core depths via the GRAPE data files. The discrete shipboard measurements were then assigned to log-equivalent depths using this map.

The amount of difference between measurements at equivalent depths is lithology-dependent. Figure 44 shows the difference between log and lab density compared to the Ca-yield profile, which mimics the calcite profile in the hole. The data are not shown below 350 mbsf because poor core recovery made it difficult to match laboratory samples to the logs. It is apparent that large differences between log and lab measurements mark low-Ca intervals. Thus, the opal- or clay-rich sections of the core have expanded more during decompression than calcite-rich sediments.

When the spliced shipboard GRAPE density profile, on the composite depth scale, is mapped to mbsf values via the logs, we see, as in the other sites, that the continuous sediment section developed from splicing is consistently longer than the *in-situ* section (Fig. 45). In the APC section, from 0 to 206 mbsf, the Site 846 composite section is stretched by 12%, slightly more than the 10% stretch at Site 844. The stretch is relatively uniform over the depth interval, however. Below 206 mbsf the core splicing ended and all additional depths were only adjusted by ODP core advancement depths. We continue to see changes in displacement in the composite vs log depths, however, which probably indicate the greater difficulty in assigning proper depths to intervals cored with the XCB.

Cherts in Site 846

Site 846 is the first drill site on Leg 138 in which cherts were cored. It is also the first site where the bottom-hole temperature recorded by

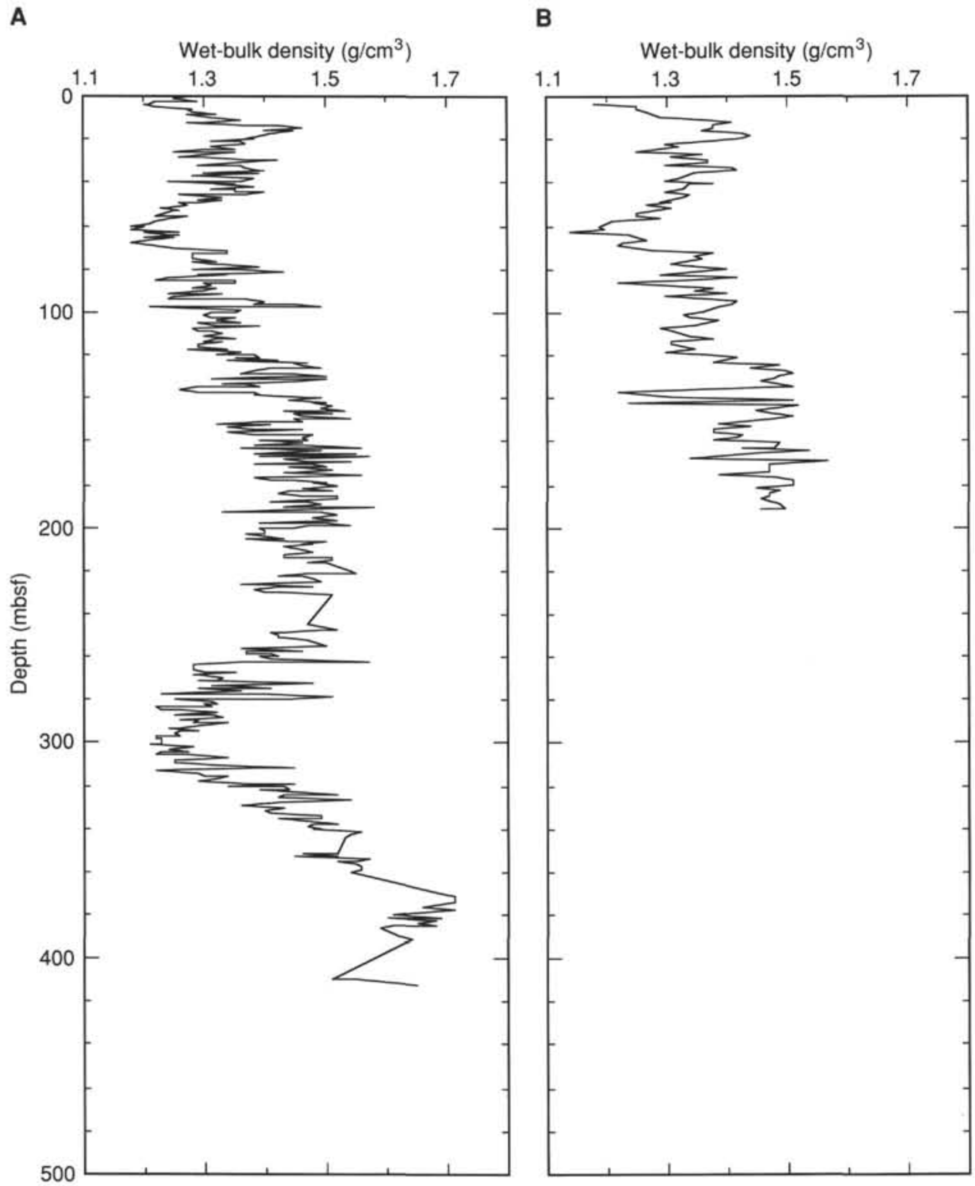

Figure 34. Wet-bulk density vs. depth, Holes 846B (**A**) and 846C (**B**).

the TLT temperature tool exceeded 5°C (15.6°C on the third logging run). More extensive cherts are found at Site 847 and the formation of cherts are discussed in more detail in that site chapter. In Hole 846B, cherts form discontinuous beds and nodules. Figure 46 is an FMS image from 365 to 373 mbsf, equivalent to Core 39X from Hole 846B. The core recovered only a few pieces of chert in the core catcher. The FMS resistivity image of the borehole wall shows the structure of these cherts as they intersect the borehole. The image is presented as if the borehole were unwrapped and flattened, and preserves the orientation of the features found. In the FMS image, cherts appear white (high resistivity). The four pads, oriented at 90° to each other, do not record single beds. Instead, one can see a discontinuous interval of cherts at 365.3 mbsf and multiple discontinuous lenses at about 370 mbsf. Scattered throughout the interval are other nodules of high resistivity material.

Uranium Record and Organic Carbon

The natural gamma-ray activity in the shallow sediments of Hole 846B is distinctly higher than at Sites 844 and 845 (Fig. 47). For example, the gamma-ray activity values of the shallow sediments of Hole 845A are typically between 15 and 20 API units. Hole 846B, in contrast, has a natural gamma-ray activity value of about 40 to 50 API units. Because the natural gamma-ray tool (NGT) can discriminate between potassium, uranium, and thorium sources for natural gamma-ray activity, we determined that the difference was primarily the result of high uranium contents in the surface sediments at Site 846.

Uranium can be enriched in marine deposits when the sedimentary redox conditions are sufficiently reducing. Uranium is sparingly soluble in seawater as U (VI), but is insoluble when reduced to U (IV). Sediment deposits rich in organic matter can collect U from seawater

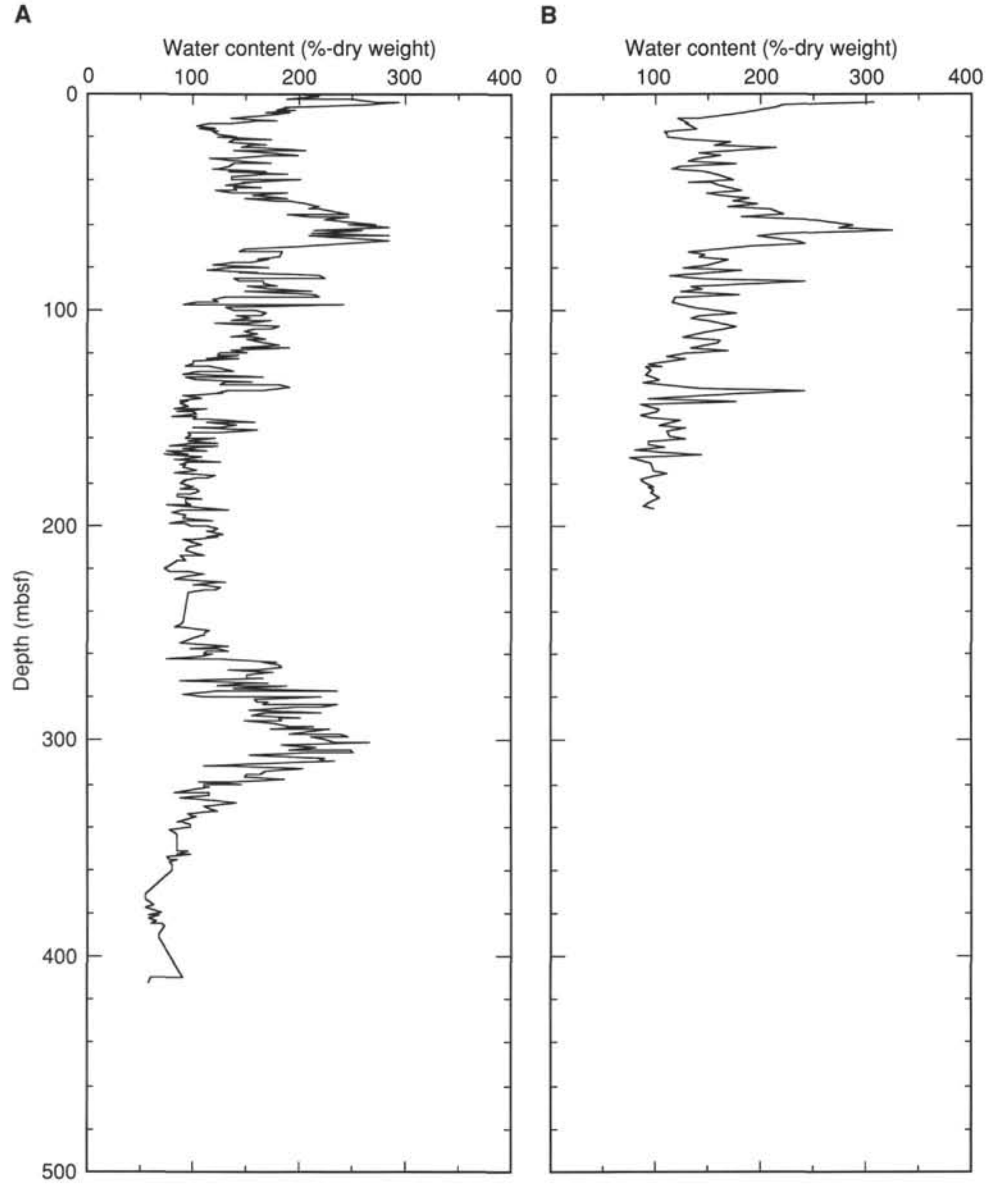

Figure 35. Water content (%-dry weight) vs. depth, Holes 846B (**A**) and 846C (**B**).

and become enriched in this element. Apparently this has happened at Site 846. Comparison of the natural gamma-ray record to measured total organic carbon in the cores (Fig. 48) shows that there is a good correlation between the two. Thus, the high natural gamma activity, above about 15 API units, is an indicator of high organic carbon contents in the sediments. The natural gamma-ray log indicates that no major organic carbon events have been missed by the shipboard sampling. The natural gamma-ray log also shows that the highest organic carbon sediments are confined to the interval above 120 mbsf or younger than about 3.5 Ma.

Comparison of Ca-Yield between Sites 845 and 846

One of the goals of Leg 138 was to reconstruct sedimentation patterns in the eastern tropical Pacific Ocean and to relate these patterns to changes in paleoceanography. We can compare carbonate profiles among the sites deep within the Guatemala Basin (Sites 844 and 845) and those on the southern flank of the Galapagos Spreading Center in the Peru Basin (Site 846). Site 845 (at a water depth of about 3700 m) also should experience more depth-dependent calcite dissolution than Site 846, which is under 3300 m of water.

To make the comparison, we used four biostratigraphic ties between the two cores for correlating roughly between Sites 845 and 846. We then assumed that carbonate varied chronostratigraphically and used CORPAC (Mattison et al., 1982) to map the Ca-yield from Site 845 to equivalent depths in Site 846. This correlation is only poor to fair in the upper 250-m equivalent depth in Site 846, primarily because very little carbonate is found in Site 845 and, hence, almost no signal to correlate. Below this depth, however, the correlation of the carbonate profiles, expressed as Ca-yield, is good (Fig. 49).

An examination of Figure 49 shows that prior to about 10 Ma both sites had high calcite concentrations, and the calcite variations appear to correlate well with each other. Almost precisely at 10 Ma, there was a collapse in carbonate deposition at both sites, approaching zero calcite deposition even at 3300 m water depth (Site 846). Even at these low carbonate levels, however, there seems to be correlation between the two sites. After 7 Ma, sedimentary carbonate burial recovered at Site 846, but not at 845.

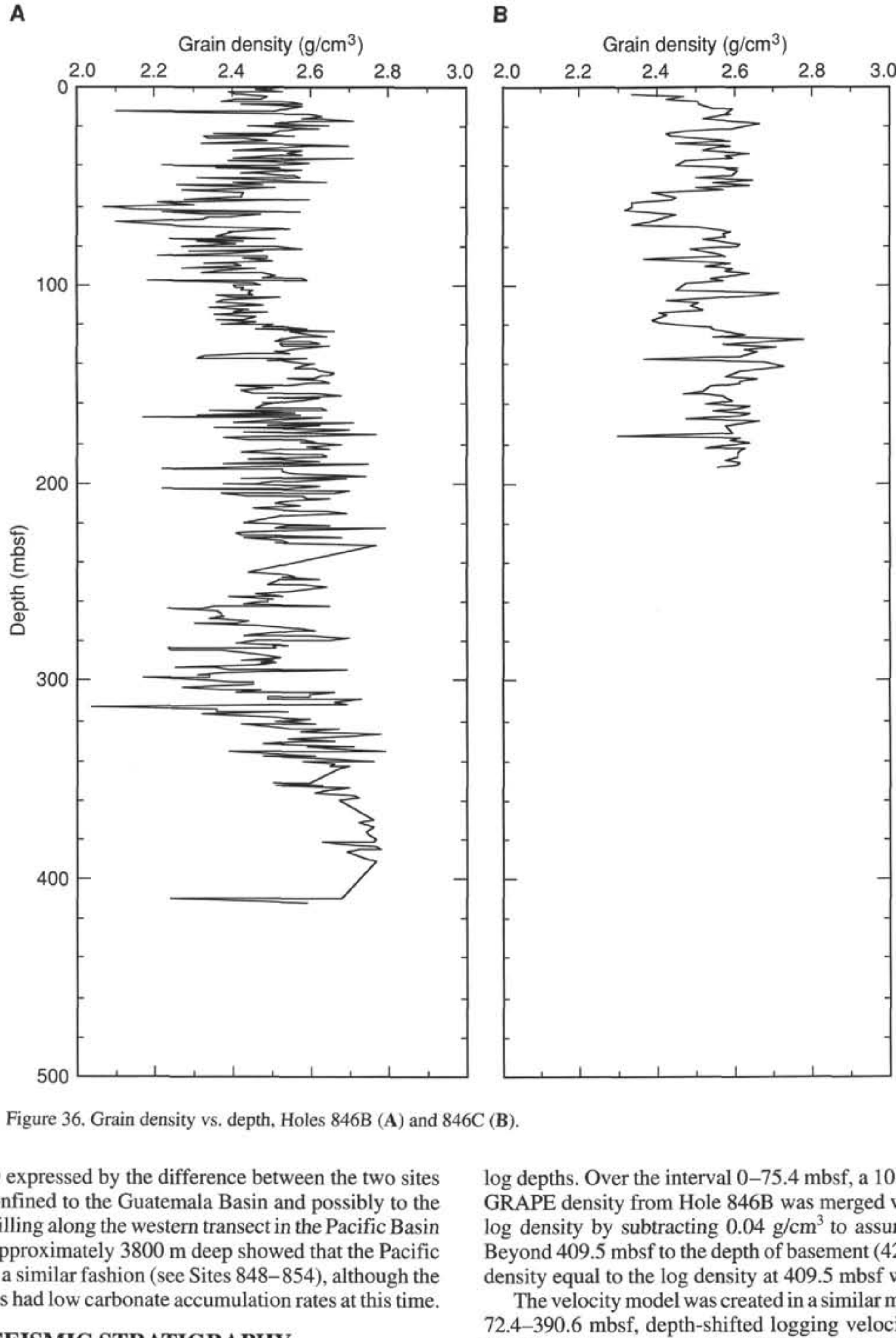

Figure 36. Grain density vs. depth, Holes 846B (**A**) and 846C (**B**).

The high CCD expressed by the difference between the two sites after 7 Ma was confined to the Guatemala Basin and possibly to the Panama Basin. Drilling along the western transect in the Pacific Basin proper in waters approximately 3800 m deep showed that the Pacific did not respond in a similar fashion (see Sites 848–854), although the more northern sites had low carbonate accumulation rates at this time.

SEISMIC STRATIGRAPHY

Modeling Procedure

Synthetic seismograms were generated from velocity and density models for Site 846 to correlate reflectors in the seismic section to stratigraphic changes (Table 20).

The density model was created by merging laboratory density to *in-situ* logging density. Depth-shifted logging density (by correlation with the Hole 846B GRAPE density) was used over the interval 77.4–391.2 m (75.4–390.5 mbsf) (see "Downhole Measurements" section, this chapter). From 390.5 to 409.5 mbsf, the log depth was shifted by −0.7 m, an amount equal to the difference in laboratory and log depths. Over the interval 0–75.4 mbsf, a 10-point boxcar-filtered GRAPE density from Hole 846B was merged with the depth-shifted log density by subtracting 0.04 g/cm^3 to assure a smooth splicing. Beyond 409.5 mbsf to the depth of basement (422.4 mbsf), a constant density equal to the log density at 409.5 mbsf was used.

The velocity model was created in a similar manner as above. From 72.4–390.6 mbsf, depth-shifted logging velocity was employed. To fill the gap in the upper part of the section, laboratory velocity data collected with the DSV were corrected to *in-situ* conditions for changes of sound speed as a function of temperature and pressure, assuming a temperature gradient of 39°C/km and a bottom-water temperature of 1.81°C determined from the temperature log. From 390.6–422.4 mbsf, a constant velocity equal to the final log velocity (1784 m/s) was used.

The accuracy of the traveltime-to-depth conversion can be evaluated by the generation of synthetic seismograms and the subsequent comparison to the seismic record collected over the site. Synthetic seismograms were generated using the above merged velocity and density data. These data were resampled at a 1-ms sample interval

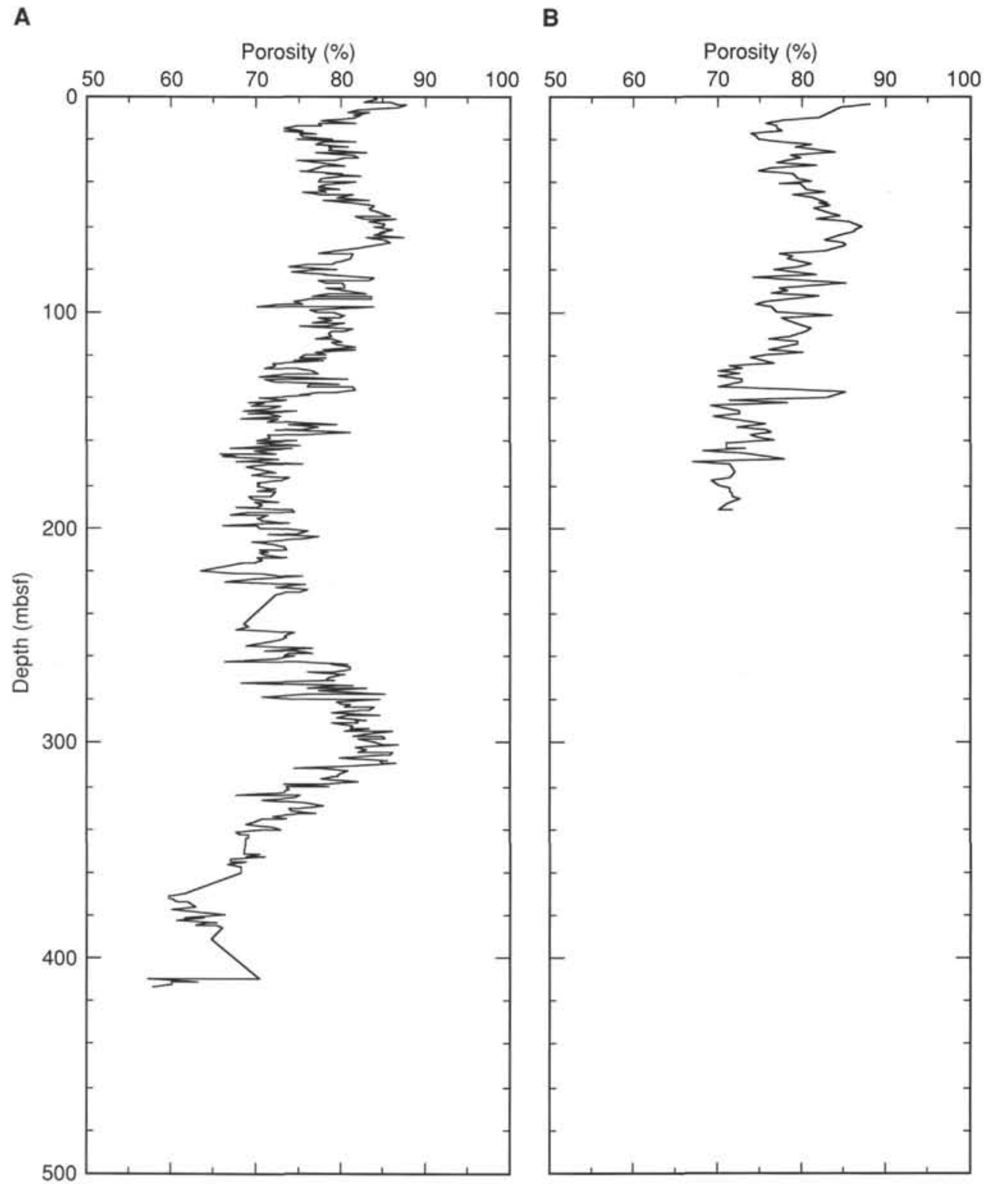

Figure 37. Porosity vs. depth, Holes 846B (**A**) and 846C (**B**).

(approximately 60 cm) and then used to calculate acoustic impedance and reflection coefficients and finally, a synthetic seismogram. Density and velocity values typical of basalt (2.5 g/cm^3 and 3000 m/s, respectively) were added at the basement depth (422.4 mbsf) to generate a basement reflector in the synthetic. The model used to generate the synthetic seismogram assumes plane waves, no multiples, and no signal attenuation; the model is described in Mayer et al. (1985). The final synthetic seismogram was filtered from 70–250 Hz., the same filter parameters as the field record collected on the site-survey cruise aboard the *Thomas Washington.*

Results

A comparison of the synthetic seismogram with the seismic profile collected at Site 846 shows a good match between the two (Fig. 50). There is an excellent correspondence between the major reflectors found in the field record and the synthetic record, with an excellent match at basement. This suggests that the traveltime-to-depth conversion is fairly accurate.

Given an acceptable velocity model, the origin of some of the reflectors at Site 846 can be analyzed. We emphasize that these are preliminary results that will undoubtedly be modified after more careful analysis. Eleven major reflectors or reflector packages were identified. These reflectors were selected on the basis of amplitude and lateral coherency in the seismic record in the immediate area of Site 846. The two-way traveltime on the synthetic seismogram of the top and bottom of each reflector was measured, and by using the assumed velocity model the depth range of each reflector was determined.

With each major reflector, there is an associated change in acoustic impedance. The velocity, density, and acoustic impedance models were compared to the depth ranges calculated from the traveltime to determine the changes in physical properties causing the selected seismic reflectors. It was found that all the reflectors correspond to a significant change density and/or velocity, to within 1 m of each calculated depth range.

In general, a large change in density and/or velocity can be associated with each reflector (Fig. 51). Reflectors for the upper 200 m (reflectors 1–8) are solely related to changes in density. Most

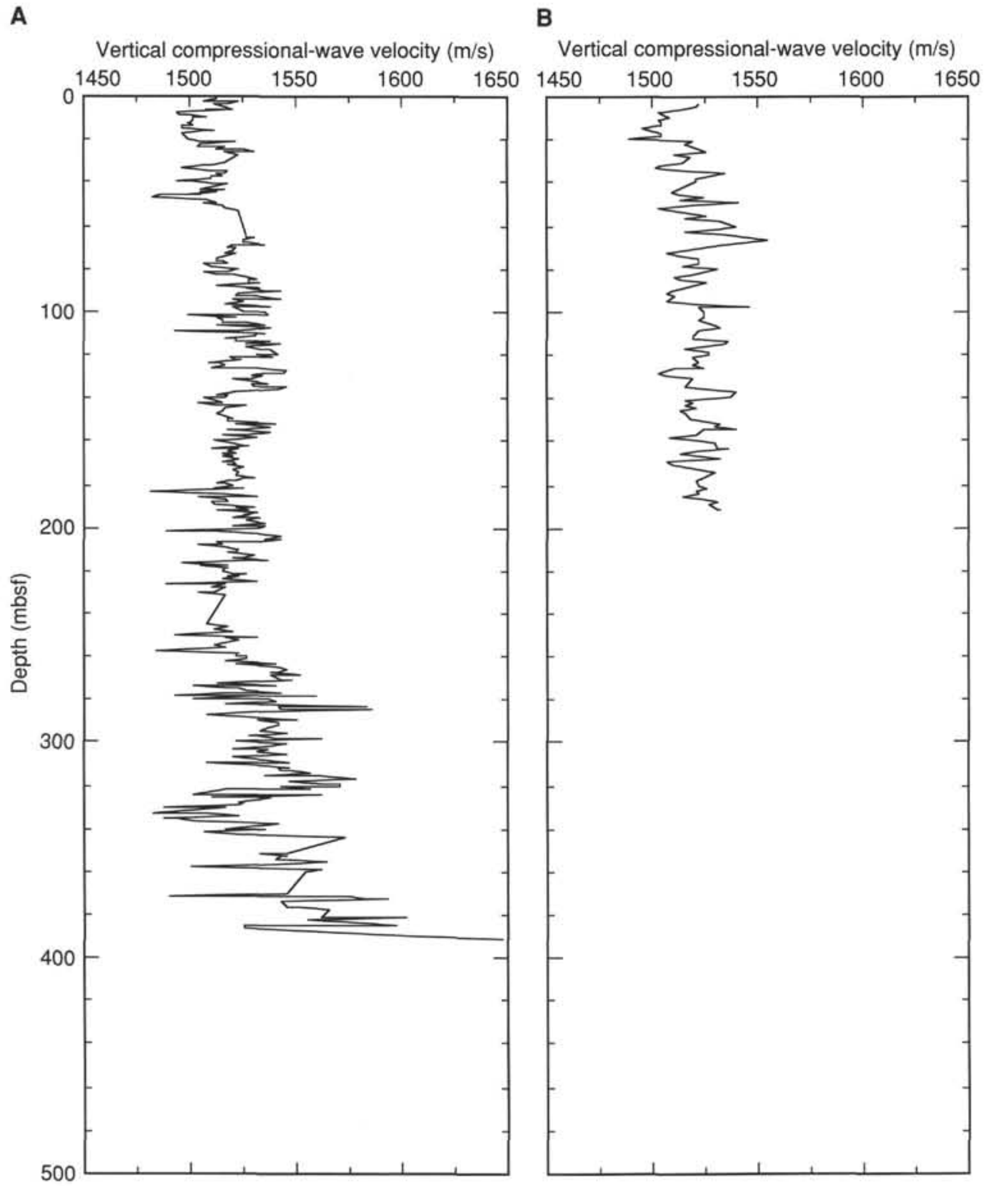

Figure 38. Compressional-wave velocity vs. depth, Holes 846B (**A**) and 846C (**B**).

of these density changes are quite large. However, the velocity changes associated with reflectors 1 and 8 are relatively modest. Beyond 200 m, the reflectors are generally due to synchronous, large fluctuations in velocity and density. The exception to this rule is reflector 16, which represents a very sharp peak in density with no associated rise in velocity. The depths (synthetic, mbsf, and mcd) and ages (based on magnetostratigraphy and biostratigraphy of Site 846; see Sedimentation Rates section, this chapter) of these reflectors are presented in Table 20. A detailed understanding of the lithologic, biostratigraphic, and ultimately, the paleoceanographic significance of these events must await shore-based studies at this time.

SUMMARY AND CONCLUSIONS

Site 846, the southernmost site of Leg 138's eastern transect, is located approximately 300 km due south of the Galapagos Islands, within the region of interaction between the South Equatorial Current (SEC) and the Peru Current. The relatively high sedimentation rates associated with this region have resulted in the accumulation of more than 400 m of sediment representing approximately 16.5 Ma of continuous deposition. Four holes were drilled at Site 846 and the combination of real-time analyses of continuous core logs (GRAPE, susceptibility, and color) with overlapping APC's have assured the complete recovery of the upper 200 m of the section (approximately the last 4 m.y.); the rest of the section was recovered (with only minor gaps) with XCB. During drilling at Site 846 we also used the XCB to sample part of the section we had already recovered with the APC. This experiment showed that while the XCB causes slightly more disturbance than the APC, the quality of XCB material is excellent and well suited for high-resolution paleoceanographic studies.

Site 846, located at approximately 3°S, is on the southern limb of the Carnegie Ridge near the boundary between crust generated at the Galapagos Spreading Center and crust generated at the East Pacific Rise. While it is impossible, given the information at hand, to determine at which spreading center the site was formed, from a paleoceanographic point of view, this is of little concern. In either case, the site formed at approximately 16.5 Ma and its absolute motion has been constrained by the Pacific-Nazca pole of rotation (as determined

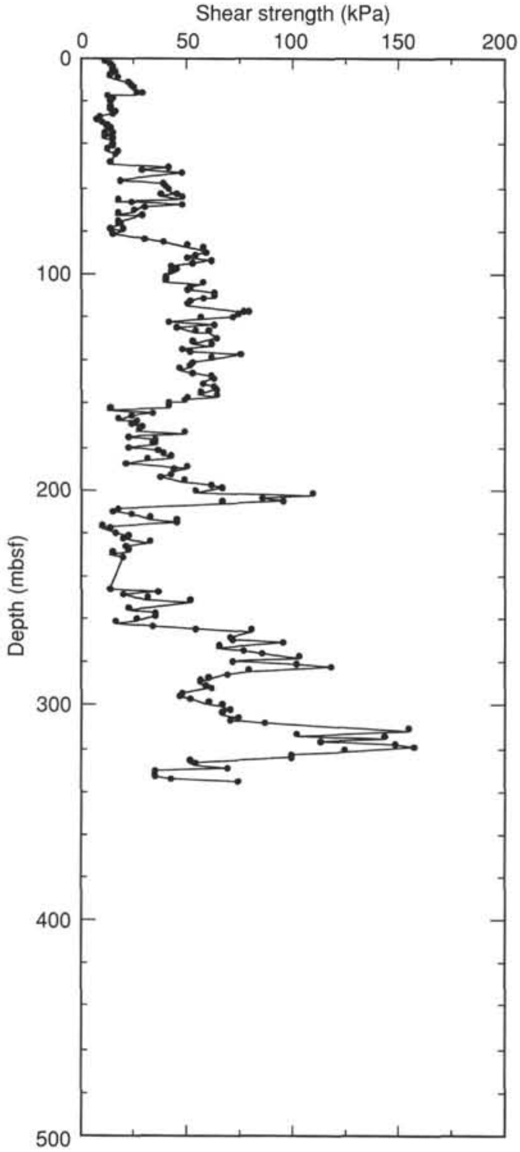

Figure 39. Undrained shear strength vs. depth, Hole 846B.

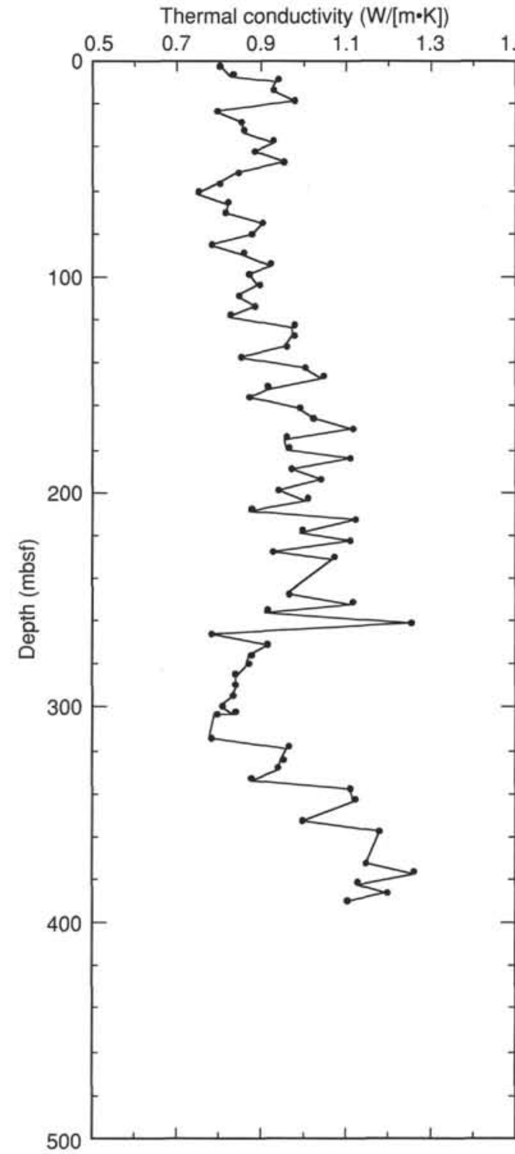

Figure 40. Thermal conductivity vs. depth, Hole 846B.

Table 19. Well logging data from Hole 846B.

Log type	Depth (mbsf)
Resistivity	83.0–419.2
Bulk density	75.1–411.1
Sonic velocity	63.2–400.4
Sonic waveforms	63.2–400.4
Gamma-ray/U-Th-K	00.0–417.2
Aluminum	00.0–405.2
Geochemistry	00.0–416.9
Caliper	66.3–417.2
Formation Microscanner	66.3–417.2
LDGE temperature	00.0–417.2

Note: Assumes seafloor at 3307.5 mbrf and with all logs correlated and depth shifted to the geophysical tool string gamma-ray log (FMS = -2.4 m; Chem = -3.0 m).

from the Hawaiian and Galapagos hot-spot trends). The resulting backtracked path (Table 21) shows that for most of its history, the site has traveled in a generally east-west direction and thus has remained at its present latitude. Paleoceanographically, this makes the site well-suited for studies of the history of equatorial circulation. While there is little conclusive evidence for which spreading center generated the crust on which Site 846 sits, the presence of a north-south oriented bathymetric offset to the west of the site (which may be related to the Galapagos Island Fracture Zone–Hey et al., 1977) leads us to postulate that the site originated at the Galapagos spreading center.

The first sediment to accumulate above the newly formed basalt at Site 846 was a very dark reddish brown metalliferous foraminifer nannofossil ooze. Overlying the metalliferous sediments are approxi-

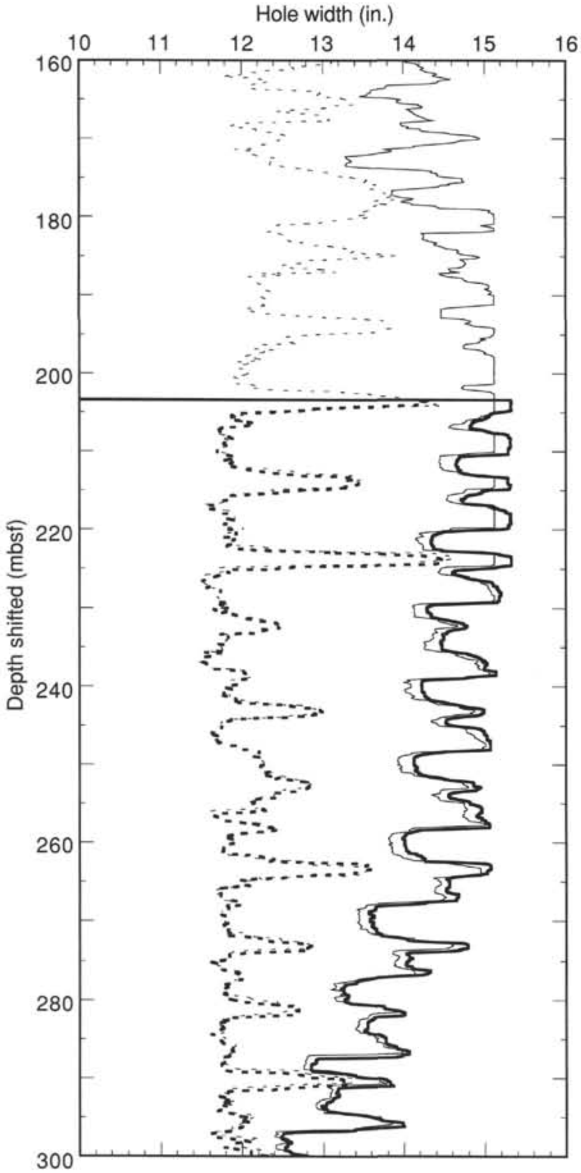

Figure 41. Caliper measurements of hole diameter. Hole 846B. The plot shows measurements for the two calipers on the FMS logging tool at 90° to each other, on two separate runs. Calipers from FMS Run 1 are shown by thick solid and dashed lines, and the run stops at about 204 mbsf. Note that the hole is oval and that, in the wider dimension, the hole is periodically greater than the FMS caliper in the interval between 180 and 230 mbsf. These periodic variations in hole width result from damage to the borehole during coring. FMS Run 2 is shown by thin solid and dashed lines.

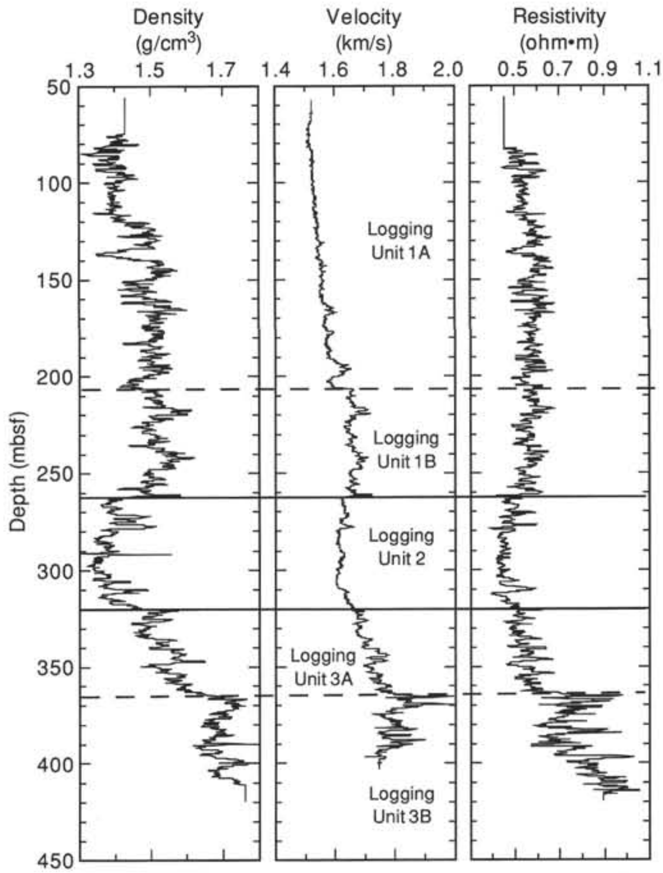

Figure 42. Variations of sonic velocity, wet-bulk density, and resistivity downhole, Hole 846B. Log-derived stratigraphic units also have been marked.

mately 40 m of clayey foraminifer nannofossil chalk with virtually no biogenic silica but with a number of chert layers (small amounts were recovered but the presence of significant amounts is clear in the logs). Interstitial waters also reflect the uptake of silica in the region by chert formation as well as the effects basalt alteration. During the time interval represented by these deposits, sedimentation rates are lowest of the entire section (approx. 10 m/m.y.—Fig. 52A) as are non-carbonate mass accumulation rates (these must be interpreted cautiously because of the presence of chert and chalk in this interval).

In the interval from 14.1 to 10.6 Ma, sedimentation rates picked up to approximately 17 m/m.y. Mass accumulation rates of all components also remain rather moderate. Carbonate contents are quite high in the predominantly nannofossil ooze section. Although this interval is dominated by pelagic carbonate, its magnetic susceptibility signal is stronger than elsewhere in the core (Fig. 52B). We attribute this to the reduced levels of organic carbon in this interval relative to the rest of the section (the susceptibility signal is lost due to dissolution of magnetic components in the presence of organic carbon and sulfate reduction; see Paleomagnetism section). The carbonate content slowly decreases up section as biogenous carbonate is replaced by biogenous silica (though biogenous silica is still only a minor component). This slow decrease in carbonate content is probably related to the gradual deepening of the site as it moves away from the ridge crest.

At approximately 10.6 Ma, a major change occurs in the sedimentary section. The period from 10.6 to about 7 Ma is characterized by a slight reduction in sedimentation and non-carbonate accumulation rates (Figs. 3 and 52) but a large decrease in the carbonate accumulation rate and the percent carbonate. The sediment accumulating at this time is predominantly clayey radiolarian diatom ooze. The effect of the increase in silica is clearly seen in the large drop in reflectance and saturated bulk density (Fig. 52C), and sonic velocity. Also associated with this interval is a small increase in clay content as seen in the smear slides, gamma logs and susceptibility. Given the large decrease in carbonate mass accumulation rate coincident with very little change in the non-carbonate accumulation rate, we interpret this major change in sedimentation to be the result of a dissolution event (or events) related to a major reorganization of Pacific circulation. A similar feature has been noted at all of the previous Leg 138 sites and at a number of other locations throughout the Pacific (Mayer et al., 1986). The detailed nature of this event, including determination of its synchroneity will be the subject of shore-based studies.

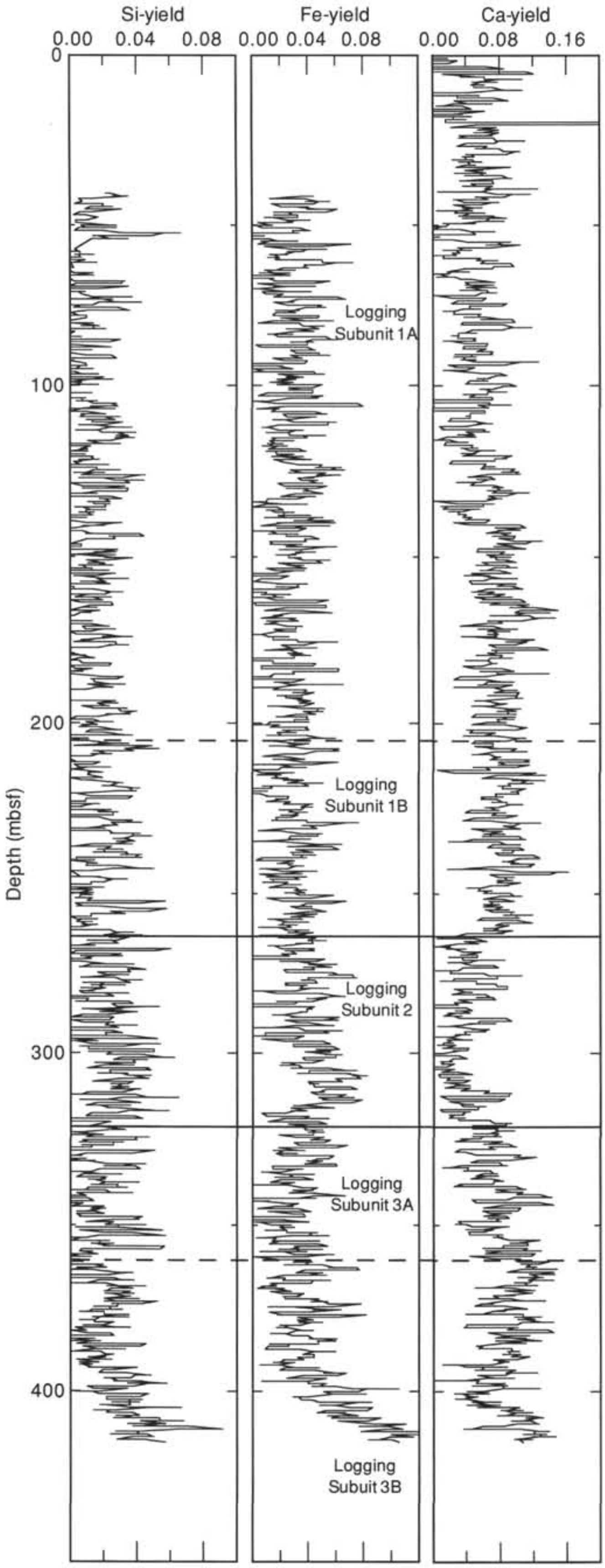

Figure 43. Variation in chemical composition downhole, Hole 846B, as recorded by the GST. Note the high Si, low Ca, and high Fe associated with logging Unit 2 (262–320 mbsf). Note also the high Fe in the basal sediments of the hole.

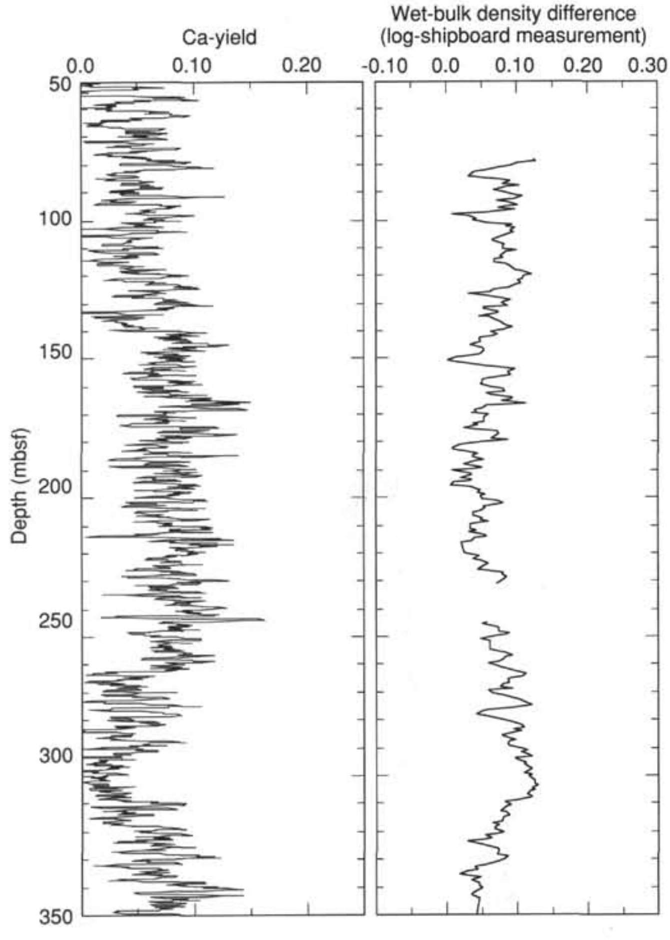

Figure 44. Difference between logging-derived wet-bulk density and that derived from shipboard measurement of discrete samples (right). Logs have been mapped to the same depth as the core with CORPAC (Martinson et al., 1982) using logs and Hole 846B GRAPE data. Data shown have also been smoothed by a five-point moving average. Density differences are compared to Ca-yield from the GST (left) as an indication of lithology. High-density differences between the two measurements generally are confined to low-Ca strata.

At approximately 7 Ma sedimentation and accumulation rates (particularly carbonate accumulation rates) increase greatly (Figs. 31 and 52A). This is in contrast to Sites 844 and 845, whose carbonate sedimentation never recovered from the middle/late Miocene boundary "dissolution event" and may be the result of the shallower depth of Site 846. If this is the case it implies the establishment of a rather steep gradient to the CCD after the middle Miocene–a feature that is still found today (Lyle, this volume).

The late Miocene to the Pleistocene was a time of generally high sedimentation (40–60 m/m.y.) and carbonate accumulation rates but with a large degree of variability in the sedimentary components, which range from nannofossil ooze to diatom ooze (though nannofossil ooze with foraminifers and diatoms is the most abundant). Carbonate contents vary widely (from 15% to 90%) reflecting relatively high-frequency changes in productivity and dissolution. Organic carbon content increases steadily throughout this interval with C_{org} accumulation rates reaching a peak during from 2 to 1 Ma. The presence of significant organic material at Site 846 (the first site to show this) is confirmed by the evidence for sulfate reduction and the distinct odor of H_2S in the upper part of the section as well as the presence of methane of unquestionable biogenic origin. The presence of methane in the midst of the sulfate reduction zone calls into question the general belief that methane forms only after the depletion of sulfate. Additionally, the absence of a susceptibility signal in the entire

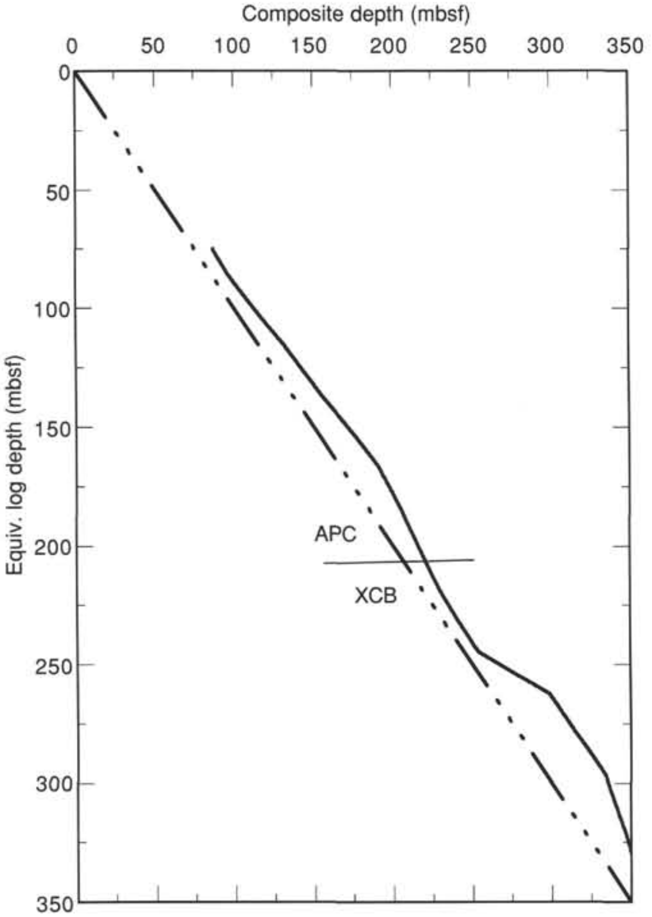

Figure 45. Composite splice depth for Hole 846B vs. log depth for equivalent density events. GRAPE data on the composite depth scale were mapped to log data (mbsf; solid line). Note that a consistent stretch occurs in the APC section, but that the XCB section, where splicing was not attempted, has variable offsets between core and log data. Dashed line = 1:1 ratio.

interval from the late Miocene to the Pleistocene can be attributed to the relatively high C_{org} concentrations and the associated reduction of magnetic minerals.

During the interval from 2 to approximately 1.5 Ma, sedimentation was once again dominated by biogenic silica components. In contrast to the earlier interval of silica dominance (10.5–7 Ma), the younger time period shows a large increase in non-carbonate accumulation rate and a decrease in carbonate accumulation rate. The combination of increased non-carbonate accumulation with decreased carbonate accumulation may indicate that productivity has increased to the point where the increase in alkalinity (associated with the organic matter) overcomes the increased production of carbonate material resulting in a net loss of carbonate. Clearly, since the late Miocene, Site 846 has been subjected to large, high-frequency changes in sediment flux. The relationship of these changes to variations in the Peru Current, to changes in climatic forcing and to fluctuations in deep ocean chemistry will be the subject of shore-based research.

REFERENCES

Barron, J. A., 1985. Late Eocene to Holocene diatom biostratigraphy of the equatorial Pacific Ocean, Deep Sea Drilling Project Leg 85. *In* Mayer, L., Theyer, F., Thomas, E., et al., *Init. Repts. DSDP,* 85: (U.S. Govt. Printing Office), 413–456.

Blow, W. H., 1969. Late middle Eocene to recent planktonic foraminiferal biostratigraphy. *Proc. First Int. Conf. Planktonic Microfossils,* Geneve, 1967. Leiden (E. J. Brill), 199–421.

Brassell, S. C., Eglinton, G., Marlowe, I. T., Pflaumann, U., and Sarnthein, M., 1986. Molecular stratigraphy: a new tool for climatic assessment. *Nature,* 320:129–133.

Bullard, E. C., 1963. The flow of heat through the floor of the ocean. *In* Hill, M. N. (Ed.), *The Sea* (Vol. 3): New York (Wiley), 218–232.

Claypool, G. E., and Kaplan, I. R., 1974. The origin and distribution of methane in marine sediments. *In* Kaplan, I. R. (Ed.), *Natural Gases in Marine Sediments.* Mar. Sci., 3:99–140.

Elderfield, H., and Gieskes J. M., 1982. Sr isotopes in interstitial waters of marine sediments from Deep Sea Drilling Project cores. *Nature,* 333:493–497.

Gieskes, J. M., 1974. Chemistry of interstitial waters of marine sediments. *Annu. Rev. Earth Planet. Sci.,* 3:433–394.

Gieskes, J. M., Elderfield, H., and Palmer, M. R., 1986. Strontium and its isotopic composition in interstitial waters of marine carbonate sediments. *Earth Planet. Sci. Lett.,* 77:229–235.

Harrison, W. E., Hesse, R., and Gieskes, J. M., 1982. Relationship between sedimentary facies and interstitial water chemistry of slope, trench, and Cocos Plate sites from the Middle America Trench transect, active margin off Guatemala, Deep Sea Drilling Project Leg 67. *In* Aubouin, J., von Huene, R., et al., *Init. Repts. DSDP,* 67: Washington (U.S. Govt. Printing Office), 603–613.

Hey, R., 1977. Tectonic evolution of the Cocos-Nazca spreading center. *Geol. Soc. Am. Bull.,* 88:1404–1420.

Hey, R., Johnson, L., and Lowrie, A., 1977. Recent plate motions in the Galapagos area. *Geol. Soc. Am. Bull.,* 88:1385–1403.

Hill, P. R., and Marsters, J. C., 1990. Controls on physical properties of Peru continental margin sediments and their relationship to deformation styles. *In* Suess, E., von Huene, R., et al., *Proc. ODP, Sci. Results,* 112: College Station, TX (Ocean Drilling Program), 623–632.

Land, L., 1980. The isotopic and trace element geochemistry of dolomite: the state of the art. *In* Zenger, D. H., Dunham, J. B., and Ethington, R. L. (Eds.), *Concepts and Models of Dolomitization.* Spec. Publ.—Soc. Econ. Paleontol. Mineral., 28:87–110.

Marlowe, I. T., Brassell, S. C., Eglinton, G., and Green, J. C., 1990. Long-chain alkenones and alkyl alkenoates and the fossil coccolith record of marine sediments. *Chem. Geol.,* 88:349–375.

Marsters, J. C., and Christian, H. A., 1990. Hydraulic conductivity of diatomaceous sediment from the Peru continental margin obtained during ODP Leg 112. *In* Suess, E., von Huene, R., et al., *Proc. ODP, Sci. Results,* 112: College Station, TX (Ocean Drilling Program), 633–638.

Martini, E., 1971. Standard Tertiary and Quaternary calcareous nannoplankton zonation. *In* Farinacci, A. (Ed.), *Proc. 2nd Planktonic Conf. Roma.* Rome (Ed. Tecnosci.), 739–785.

Martinson, D. G., Menke, W., and Stoffa, P., 1982. An inverse approach to signal correlation. *J. Geophys. Res.,* 87:4807–4818.

Mayer, L. A., Shipley, T. H., Theyer, F., Wilkens, R. W., and Winterer, E. L., 1985. Seismic modelling and paleoceanography at DSDP Site 4. *In* Mayer, L. A., Theyer, F., Thomas, E., et al., *Init. Repts. DSDP,* 85: Washington (U.S. Govt. Printing Office), 947–970.

Mayer, L. A., Shipley, T. H., and Winterer, E. L., 1986. Equatorial Pacific seismic reflectors as indicators of global oceanographic events. *Science,* 233:761–764.

McDuff, R. E., 1981. Major cation gradients in DSDP interstitial waters: the role of diffusive exchange between seawater and the upper ocean crust. *Geochim. Cosmochim. Acta,* 45:1705–1713.

Okada, H., and Bukry, D., 1980. Supplementary modification and introduction of code numbers to the low-latitude coccolith biostratigraphic zonation (Bukry, 1973; 1975). *Mar. Micropaleontol.,* 5:321–325.

Prahl, F. G., de Lange, G., Lyle, M., and Sparrow, M. A., 1989. Postdepositional stability of long-chain alkenonea under contrasting redox conditions. *Nature,* 341:434–437.

Prahl, F. G., Muehlhausen, L. A., and Zahnle, D. L., 1988. Further evaluation of long-chain alkenones as indicators of paleoceanographic conditions. *Geochim. Cosmochim. Acta,* 52:2303–2310.

Rio, D., Backman, J., and Raffi, I., in press. Calcareous nannofossil biochronology and the Pliocene-Pleistocene boundary. *In* Van Couvering, J. (Ed.), *Final Repts., IGCP Project,* 41.

Rio, D., Fornaciari, E., and Raffi, I., 1990. Late Oligocene through early Pleistocene calcareous nannofossils from western Equatorial Indian Ocean (Leg 115). *In* Duncan, R. A., Backman, J., Peterson, L. C., *Proc. ODP, Sci. Results,* 115: College Station, TX (Ocean Drilling Program), 175–235.

Ms 138A-111

NOTE: For all sites drilled, core description forms ("barrel sheets") and core photographs have been reproduced on coated paper and can be found in Section 4, beginning on page 397. Forms containing smear-slide data can be found in Section 5, beginning on page 663.

Formation microscanner images for this site are presented on microfiche in the back of Part 2.

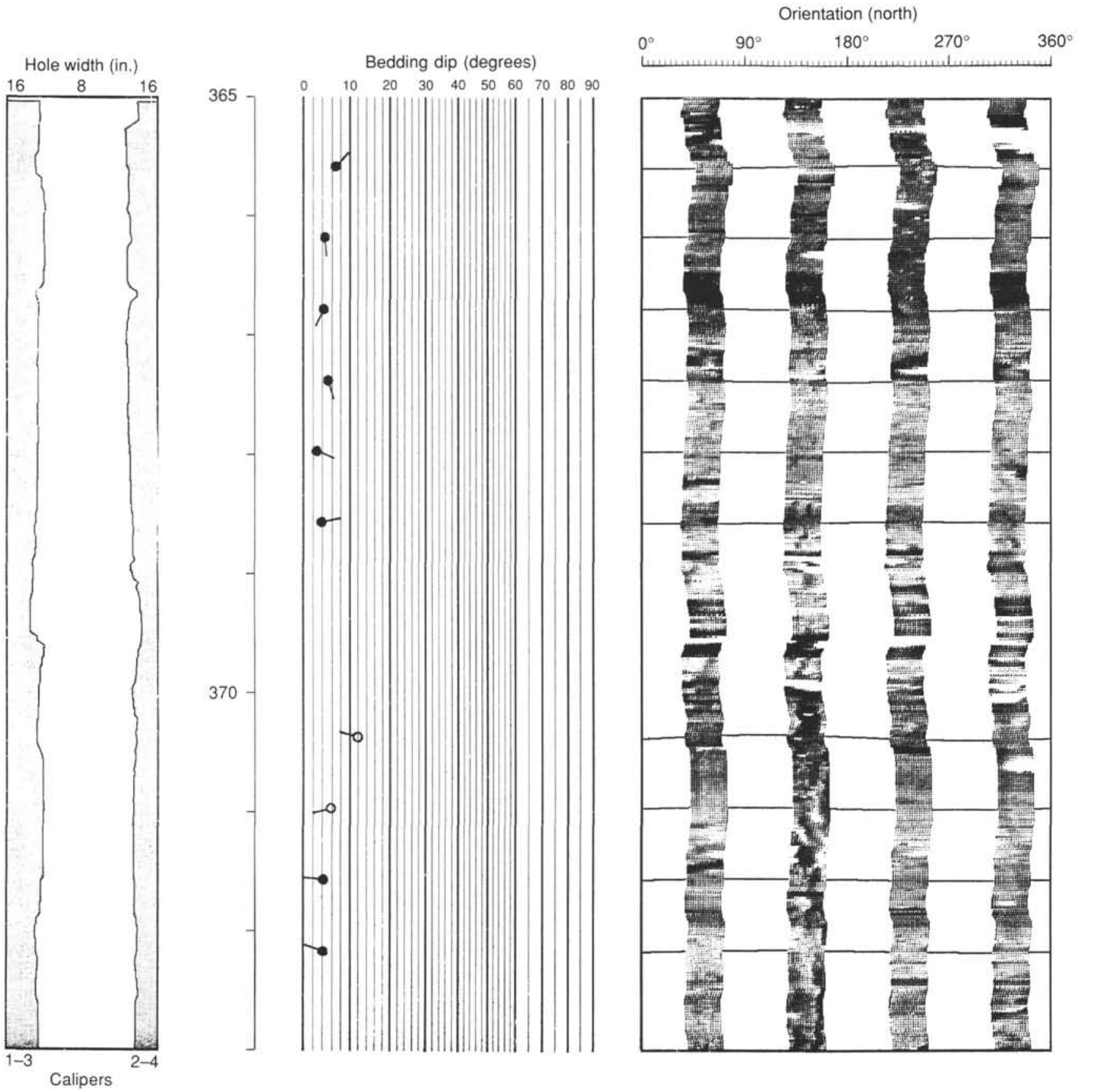

Figure 46. FMS resistivity image of the borehole from 365 to 373 mbsf to show cherts in that interval. Figure shows hole width (left), bedding dip relative to borehole (center), and oriented images from the four pads riding up the borehole wall (right). Because cherts have high resistivity, they appear white in the image. Two main intervals of chert can be identified: (1) at about 365.3 and (2) 370 mbsf. Both of these intervals appear to contain discontinuous lensoid bodies of chert. Scattered throughout the section are other chert nodules.

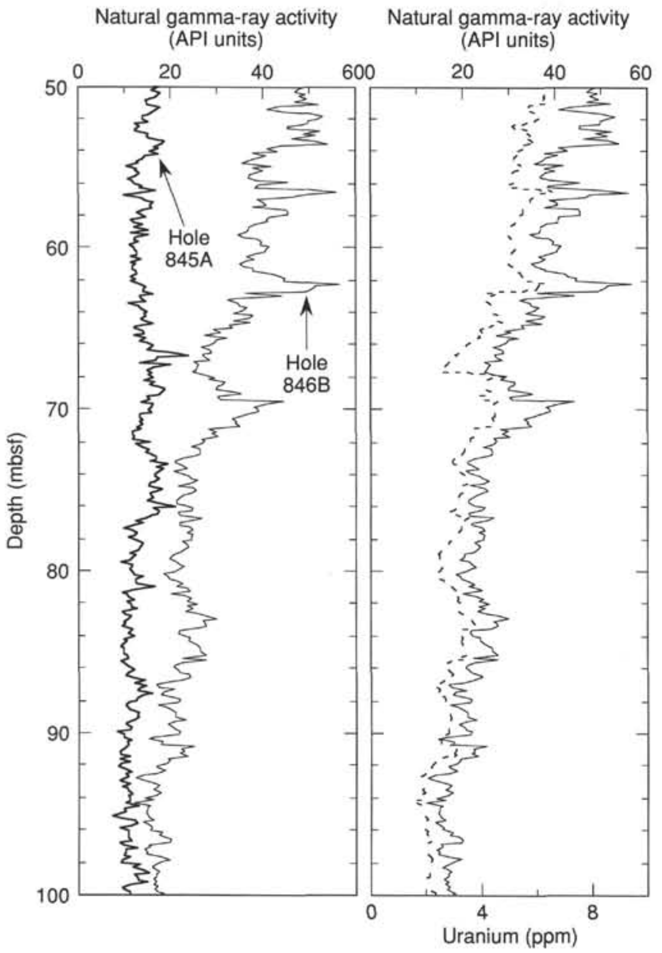

Figure 47. Natural gamma-ray activity at Site 846 is significantly higher than at other Leg 138 sites. Shown on the right is a comparison of Hole 846B (thin solid line) with Hole 845A (thick solid line), which in shallow sediments has about one-third the activity of Hole 846B. On the left is a comparison of the total natural gamma-ray activity (solid line) with that from uranium (dashed line).

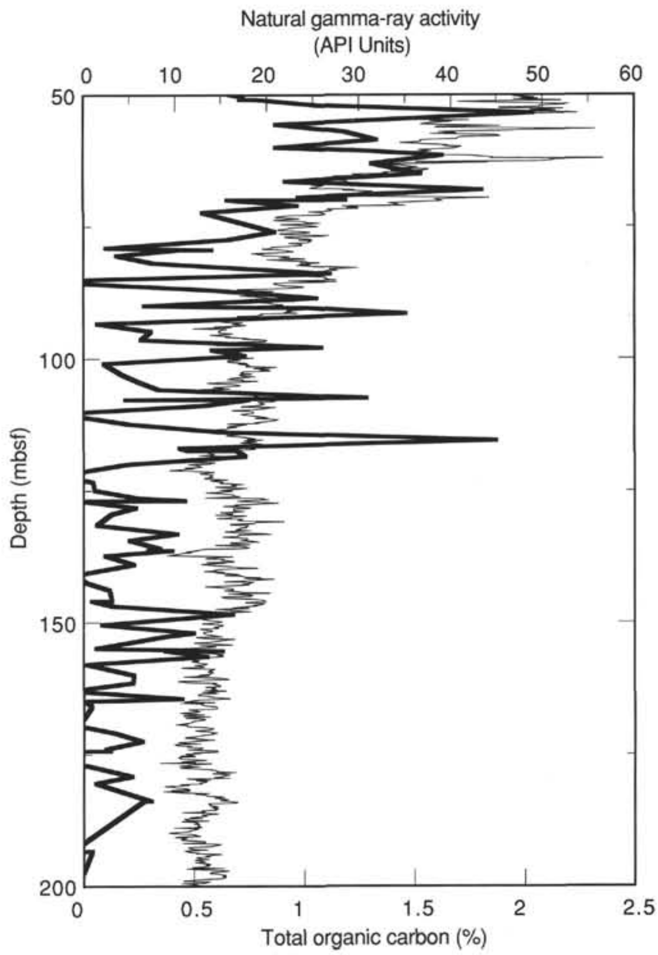

Figure 48. Comparison of natural gamma-ray activity in Hole 846B (thin solid line) to organic carbon content (thick solid line), measured in discrete samples. A good correlation exists between organic carbon content and natural gamma-ray activity in shallow sediments at this site.

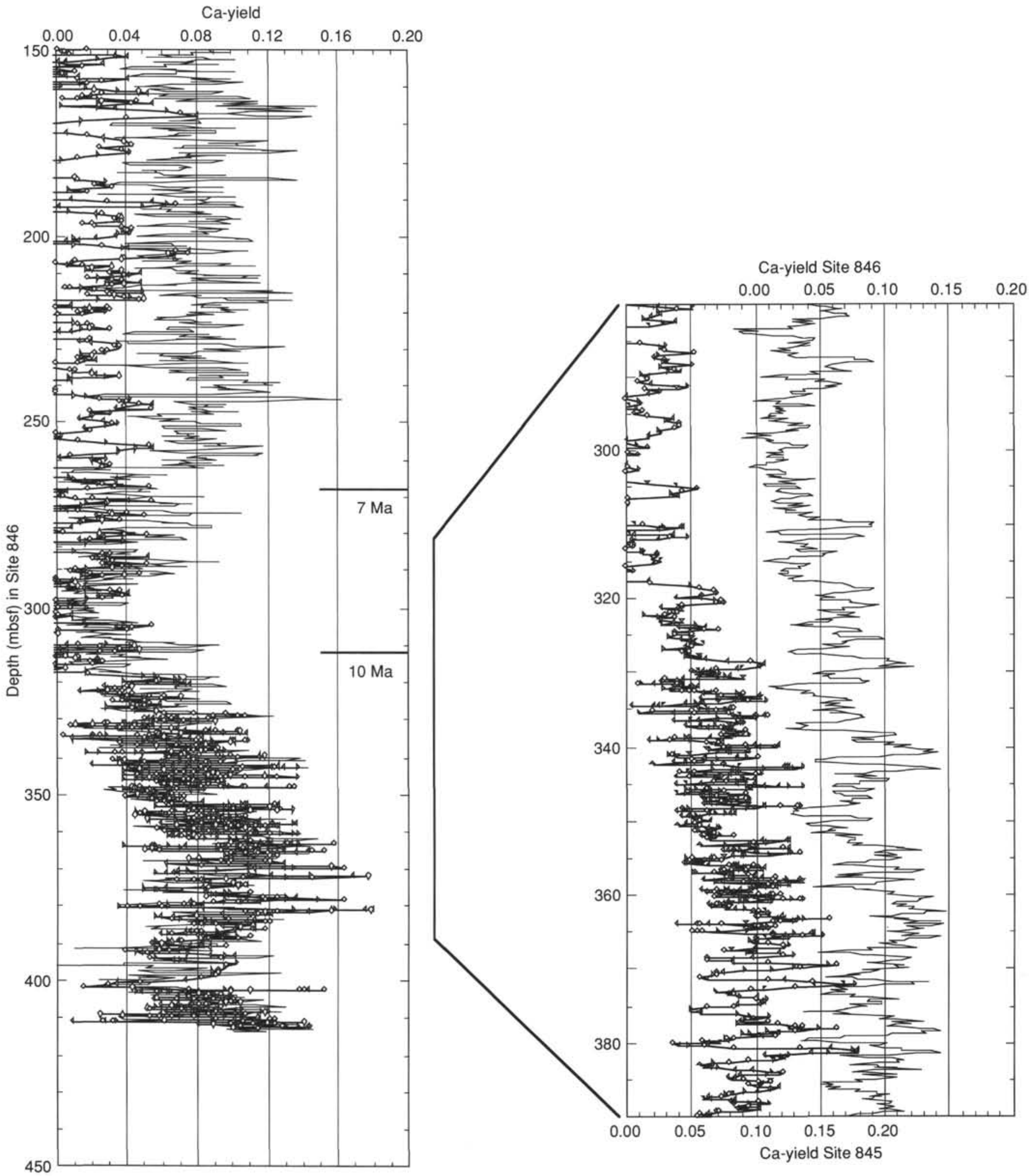

Figure 49. Comparison of Ca logs from the GST of Site 845 (thin line with symbols) with those of Site 846 (thin solid line), mapped to equivalent depths with CORPAC (Martinson et al., 1982). The good coherence between the two records in the lower section (from about 17 to about 7 Ma) indicates that the two sites were bathed by similar bottom waters. After 7 Ma, the deeper Site 845 in the Guatemala Basin remained almost barren of calcite, while Site 846 rebounded to relatively high Ca values. These data show that either the CCD became defined between the two sites at 7 Ma or that the Guatemala Basin (Site 845) developed different bottom waters from those of the northern flank of the Peru Basin (Site 846).

Table 20. Summary of traveltimes, depths, and ages for Site 846 reflectors.

Reflector	Traveltime (s)	Synthetic depth (m)	Depth (mbsf)	Depth (mcd)	Age (Ma)
R1	0.037	27.50	27.00	30.20	0.75
	0.041	30.50	30.50	33.70	0.84
R2	0.063	42.00	47.00	53.50	1.38
	0.068	50.70	49.50	56.00	1.46
R3	0.093	69.60	68.50	78.20	1.97
	0.099	74.20	73.00	82.70	2.07
R6	0.180	135.70	135.50	155.20	3.68
	0.187	141.10	140.00	159.70	3.77
R7	0.192	145.00	144.00	164.20	3.86
	0.205	155.00	155.00	176.30	4.10
R8	0.232	176.00	175.00	198.80	4.55
	0.235	178.30	176.00	199.80	4.57
R10	0.270	206.40	205.00	235.40	5.37
	0.276	210.80	210.00	244.00	5.59
R12	0.297	228.00	227.00	262.10	6.05
	0.301	231.30	230.50	265.60	6.14
R14	0.337	261.30	261.00	296.10	6.91
	0.347	269.50	264.00	299.10	6.99
R16	0.365	283.80	292.00	327.10	8.84
	0.373	291.00	294.00	329.10	8.97
R17	0.407	317.30	318.00	353.10	10.53
	0.410	319.70	322.00	357.00	10.78
R20	0.480	380.60	379.00	414.10	14.85
	0.486	386.00	385.50	420.60	15.47
Basement	0.525	421.50	421.50	456.60	18.76
	0.530				

Table 21. Paleolatitudes for Site 846.

Age (Ma)	Latitude (°S)	Longitude (°W)
0	3.10	90.83
1	3.08	91.52
2	3.06	92.25
3	3.04	92.97
4	3.01	93.70
5	2.98	94.42
6	2.95	95.14
7	2.91	95.87
8	2.87	96.59
9	2.83	97.31
10	2.78	98.03
11	2.74	98.76
12	2.69	99.48
13	2.70	100.25
14	2.71	101.01
15	2.71	101.78
16	2.71	102.55
17	2.71	103.31

Poles of rotation = 0–12 Ma: 71.5°N, 86.8°W and 12–17 Ma: 67.2°N, 102.2°W.
Angular velocity = -0.75°/m.y. and -0.83°/m.y.

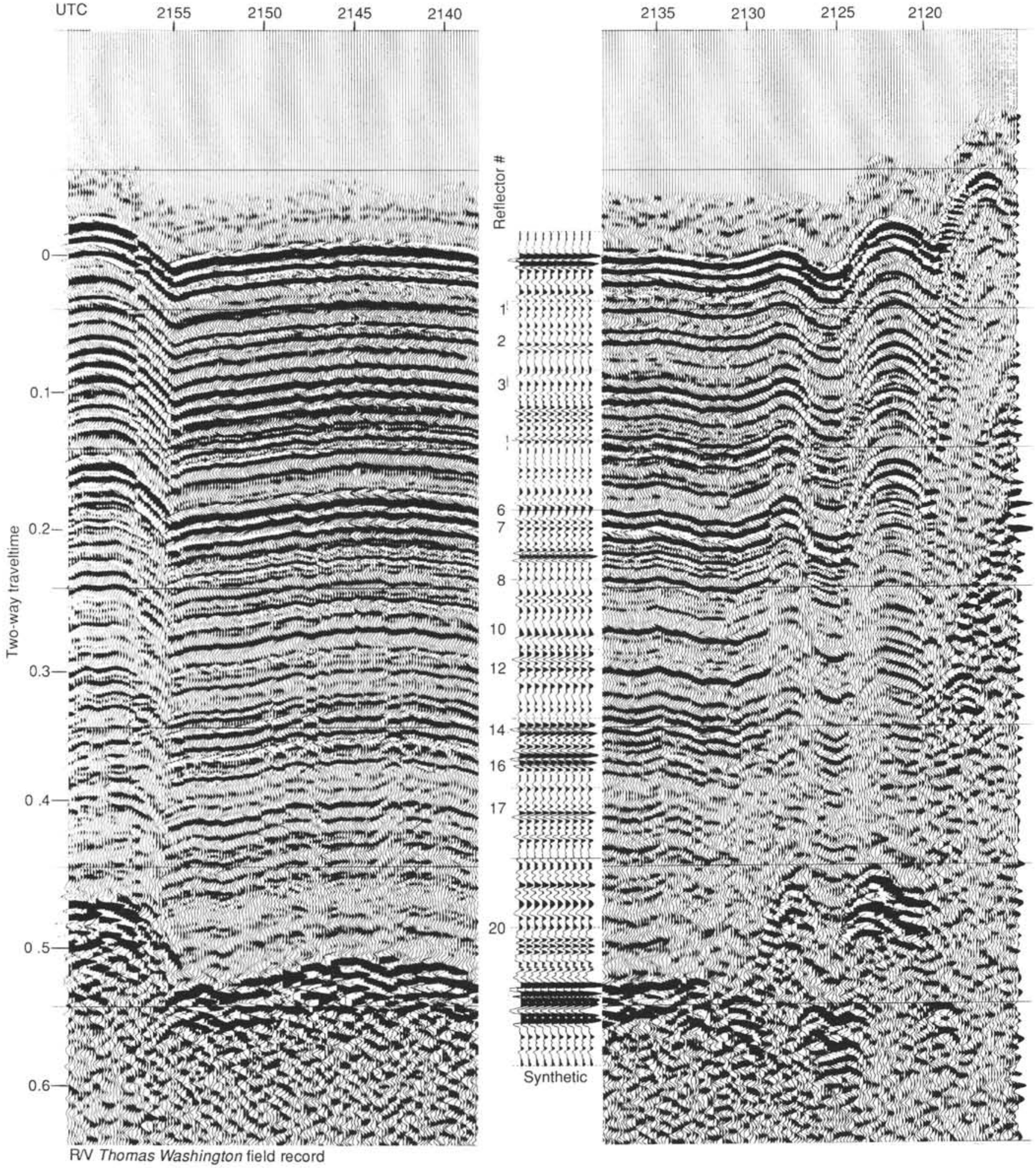

Figure 50. Comparison of synthetic seismogram with field record, Site 846. See text for discussion of origin of reflectors 1 through 20.

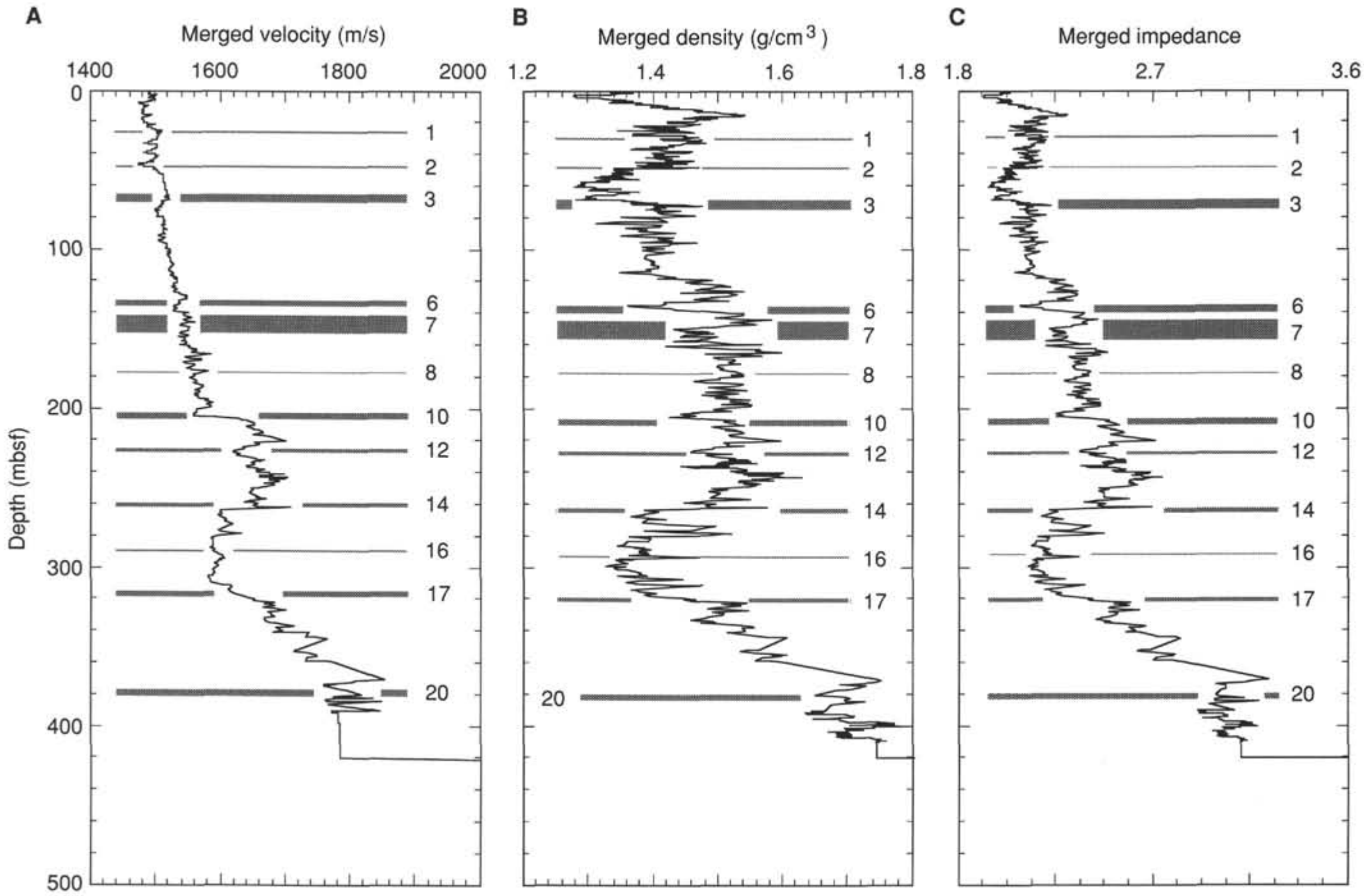

Figure 51. Data used for generating Site 846 synthetic seismograms. **A.** Velocity. **B.** Density. **C.** Acoustic impedance. The 12 reflectors selected from the synthetic seismogram are shown for comparison.

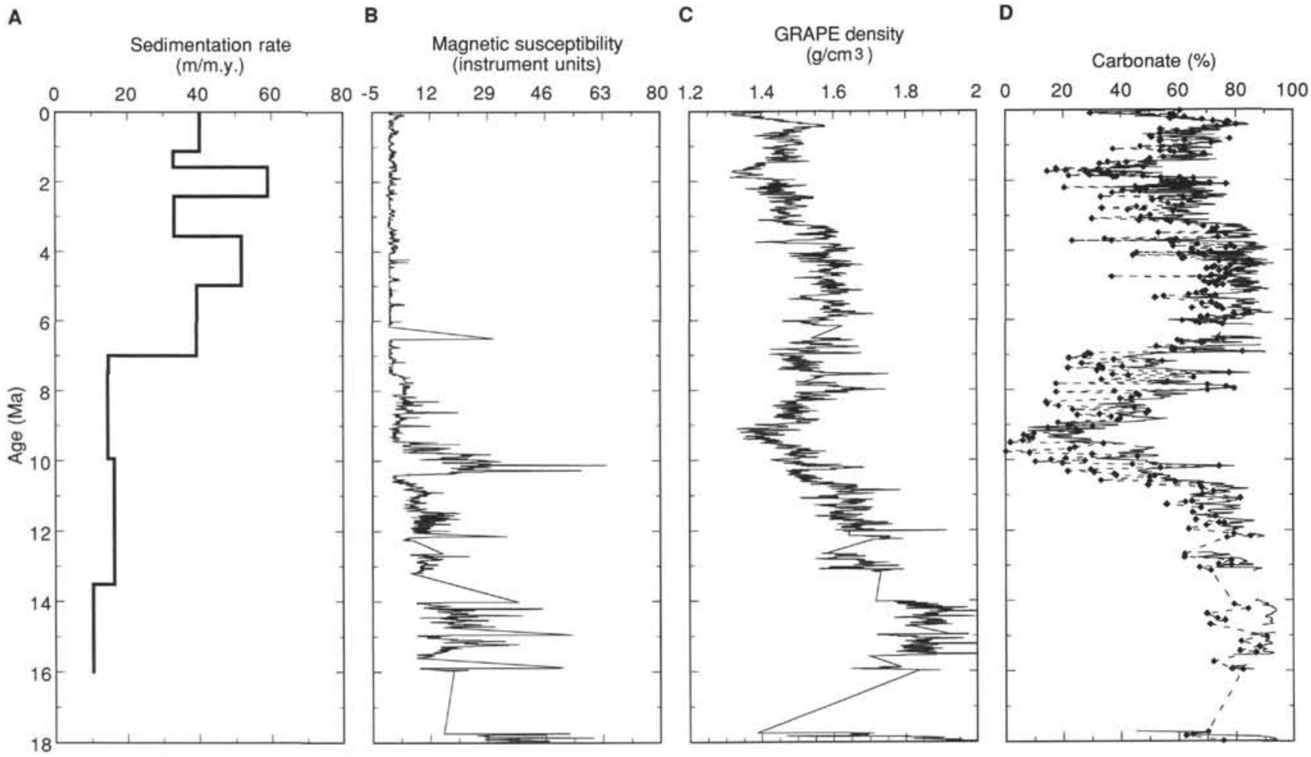

Figure 52. **A.** Sedimentation rate vs. sediment age. **B.** Sediment magnetic susceptibility vs. age. **C.** Sediment density vs. age. **D.** Predicted carbonate (solid line) and discrete shipboard carbonate measurement (dashed line with solid diamonds).

Hole 846B: Resistivity-Sonic-Natural Gamma Ray Log Summary

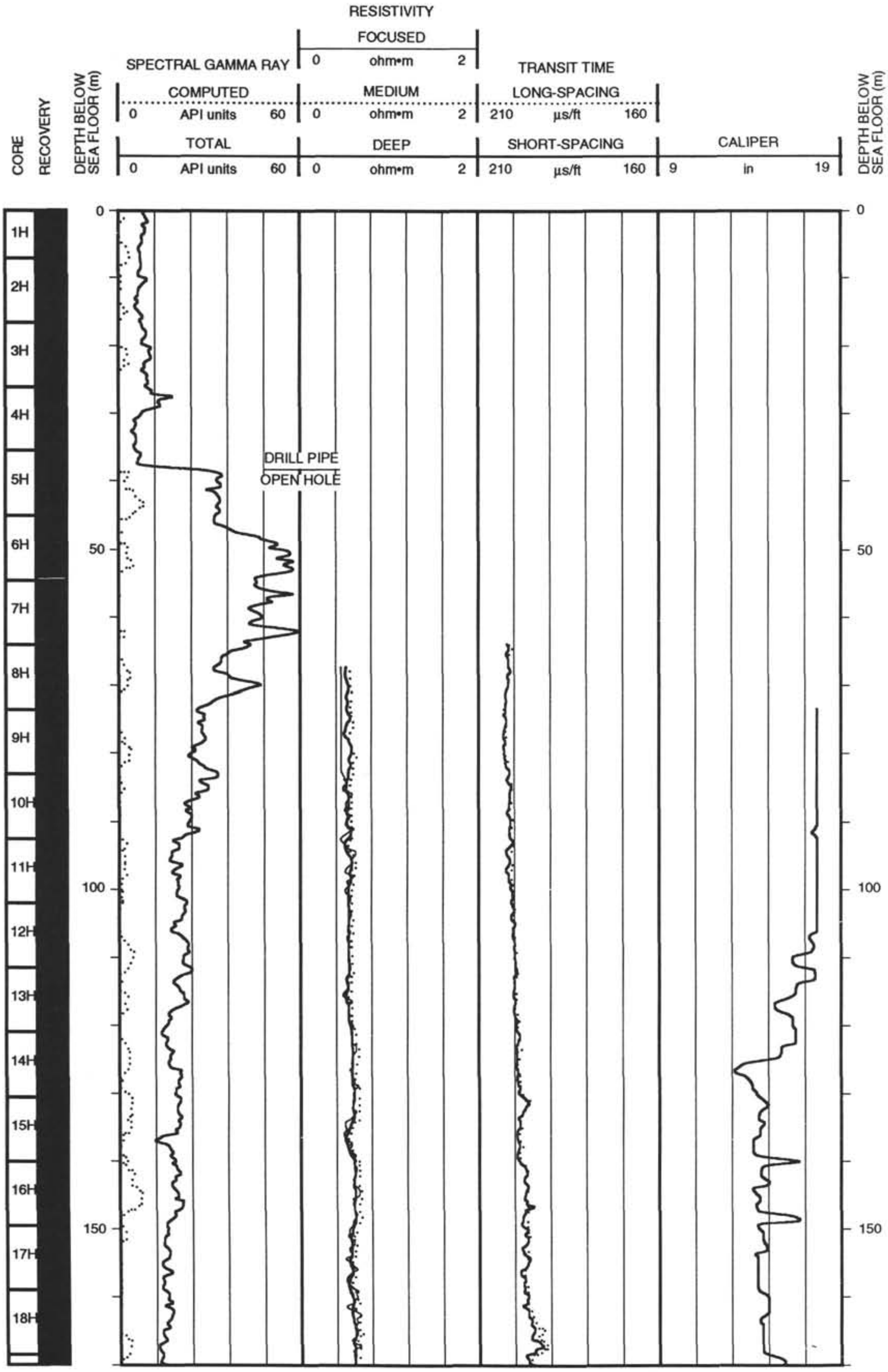

Hole 846B: Resistivity-Sonic-Natural Gamma Ray Log Summary (continued)

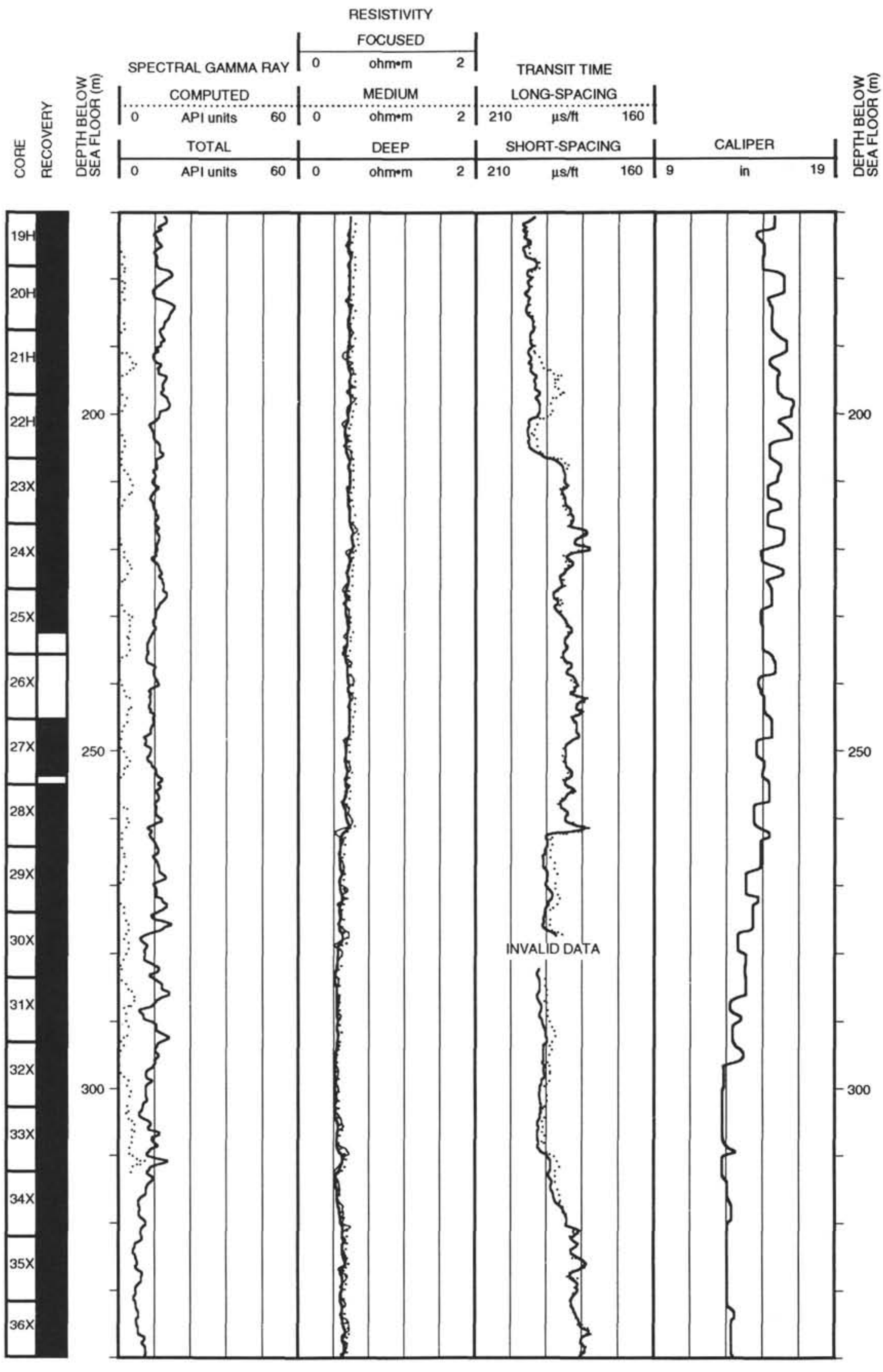

Hole 846B: Resistivity-Sonic-Natural Gamma Ray Log Summary (continued)

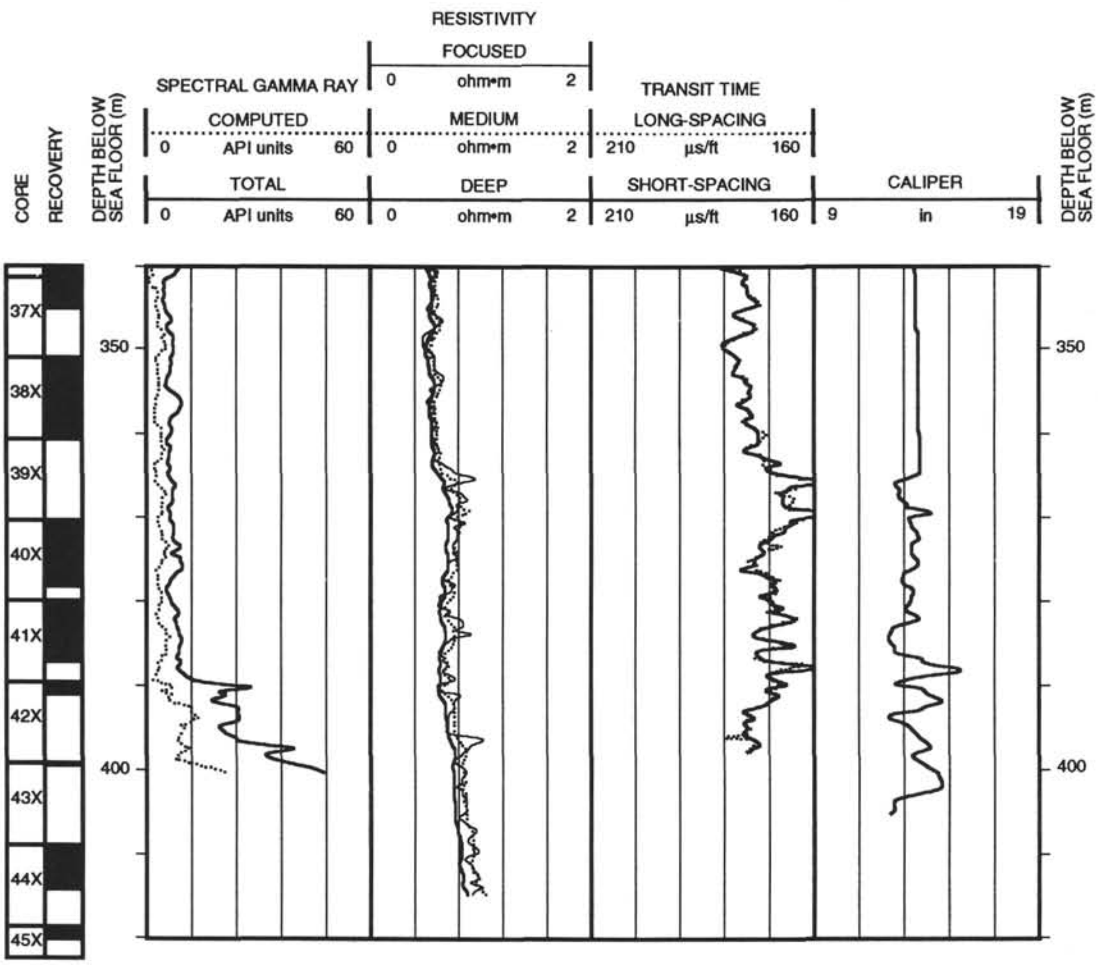

Hole 846B: Density-Natural Gamma Ray Log Summary

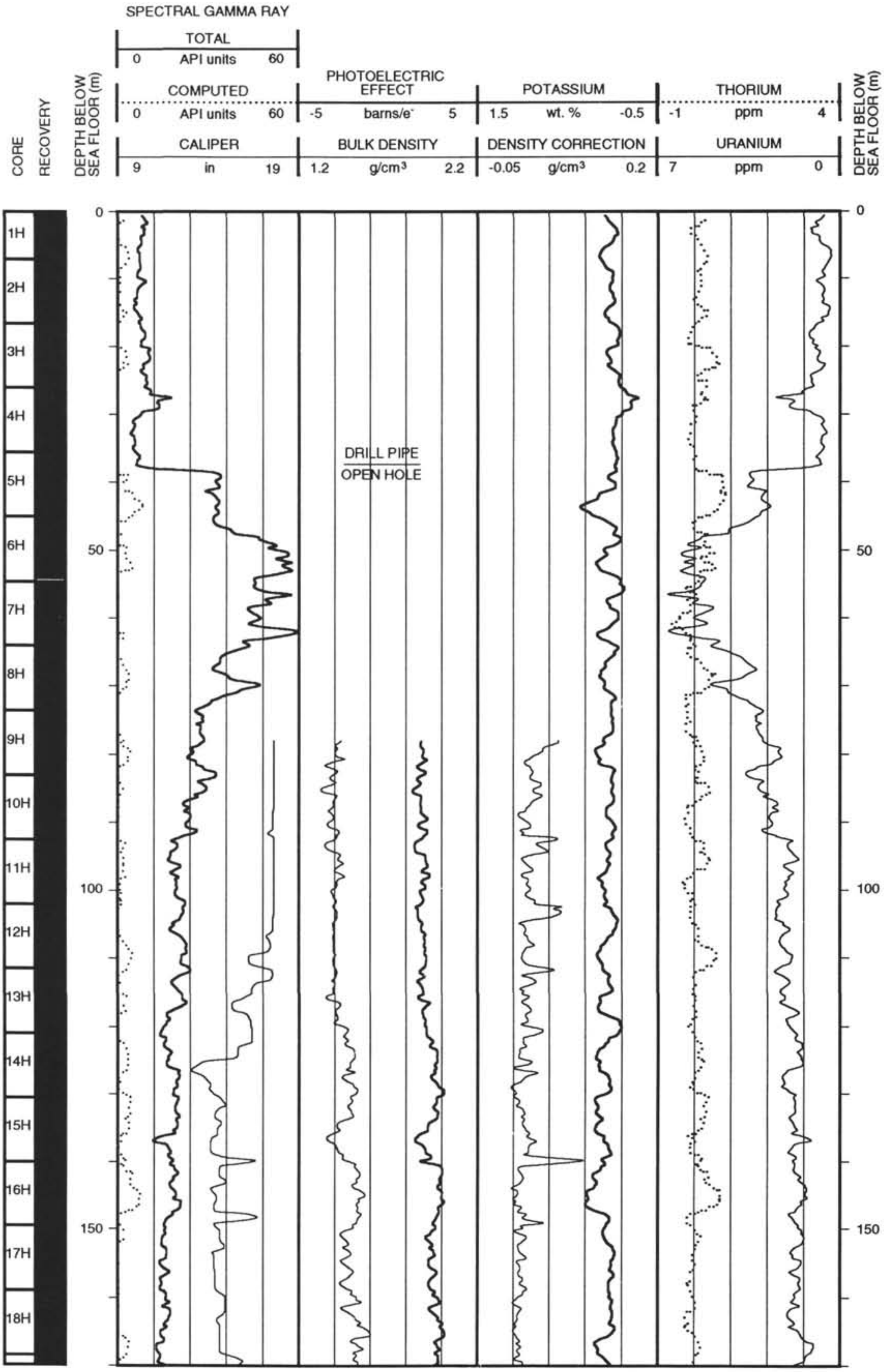

Hole 846B: Density-Natural Gamma Ray Log Summary (continued)

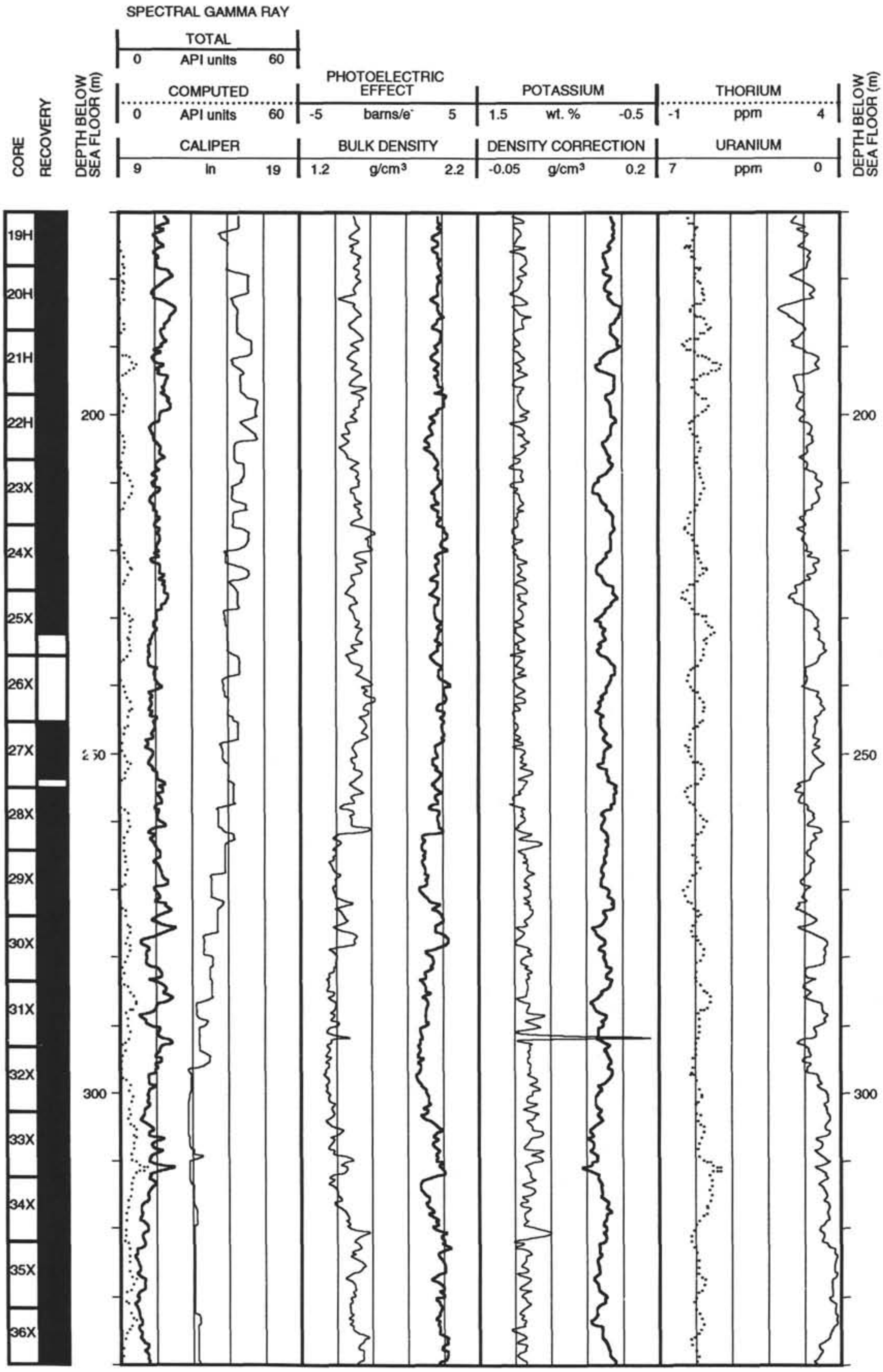

Hole 846B: Density-Natural Gamma Ray Log Summary (continued)

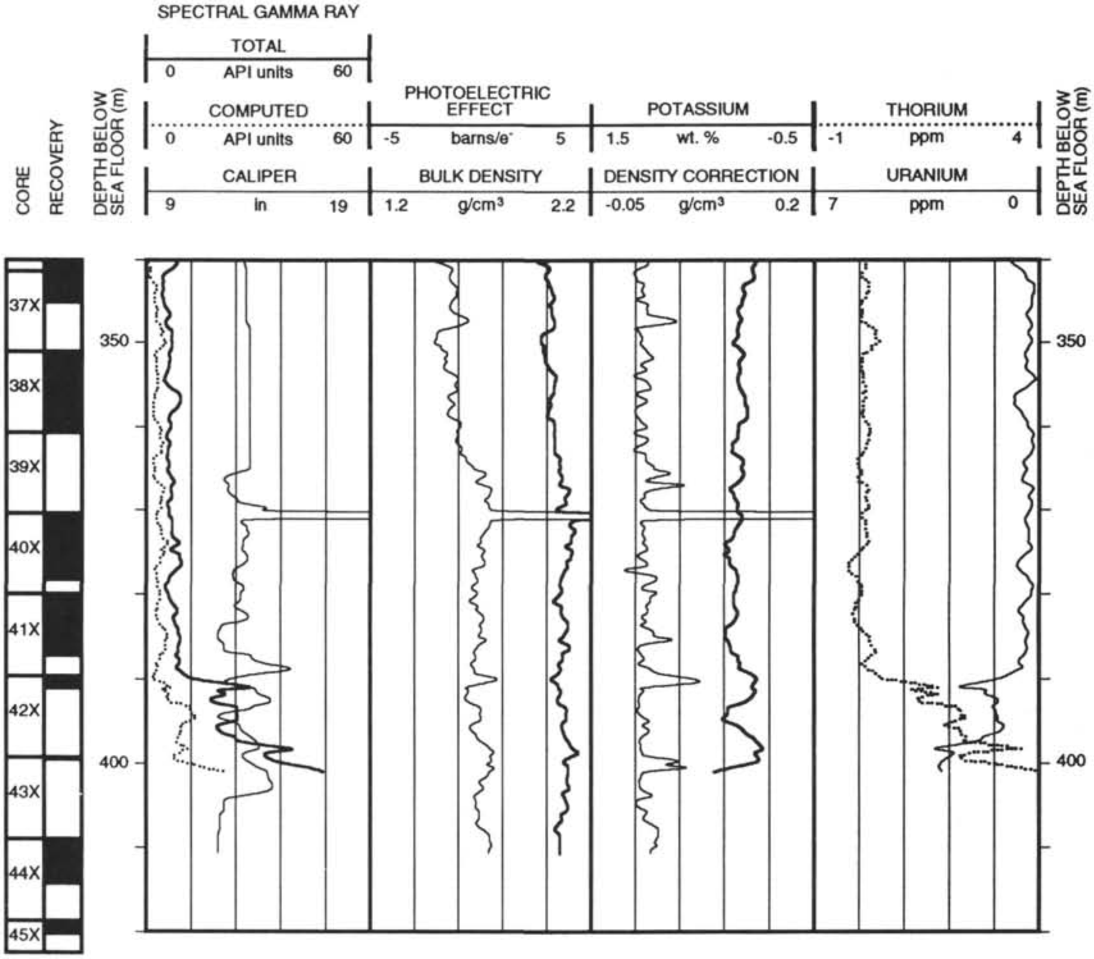

Hole 846B: Geochemical Log Summary

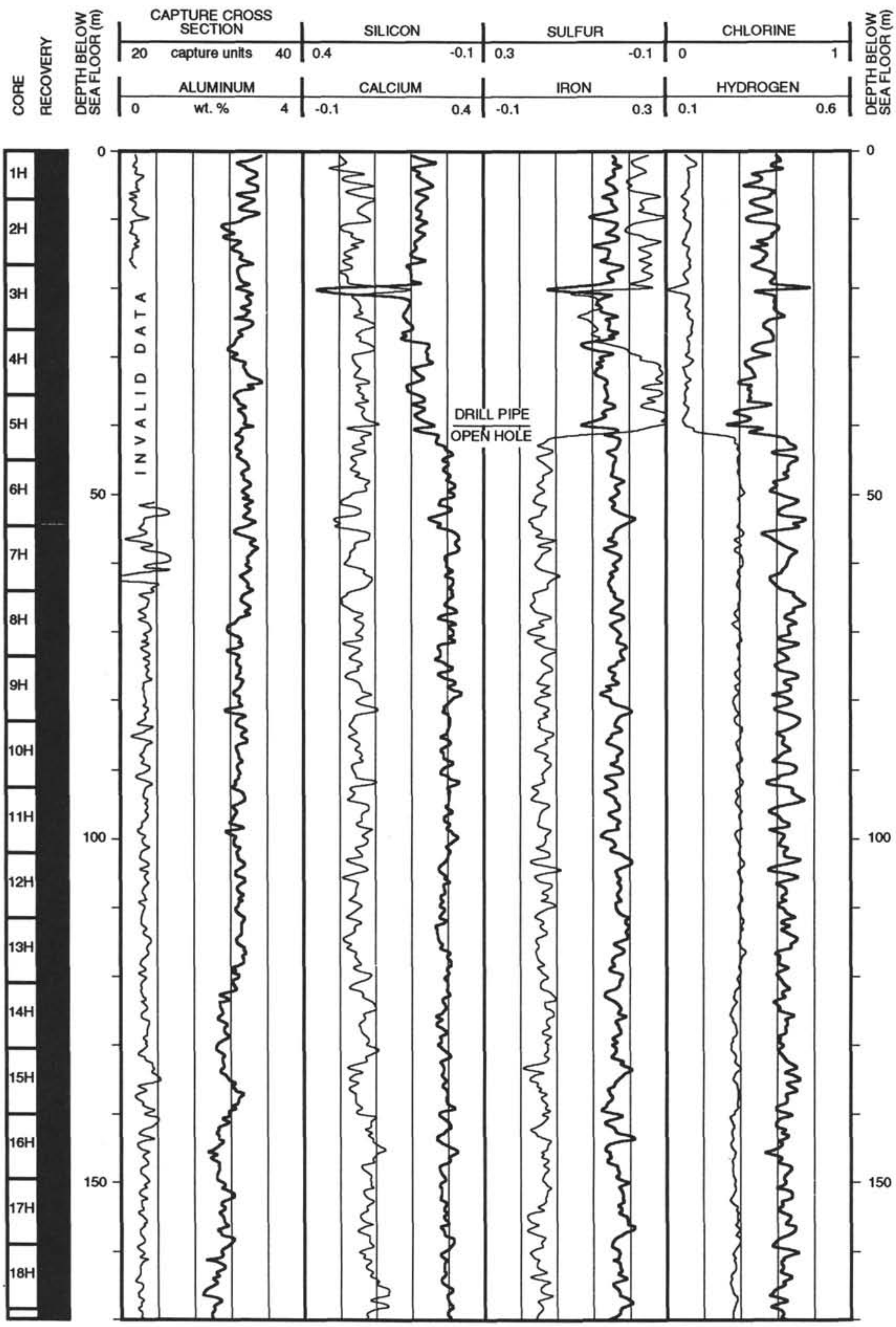

Hole 846B: Geochemical Log Summary (continued)

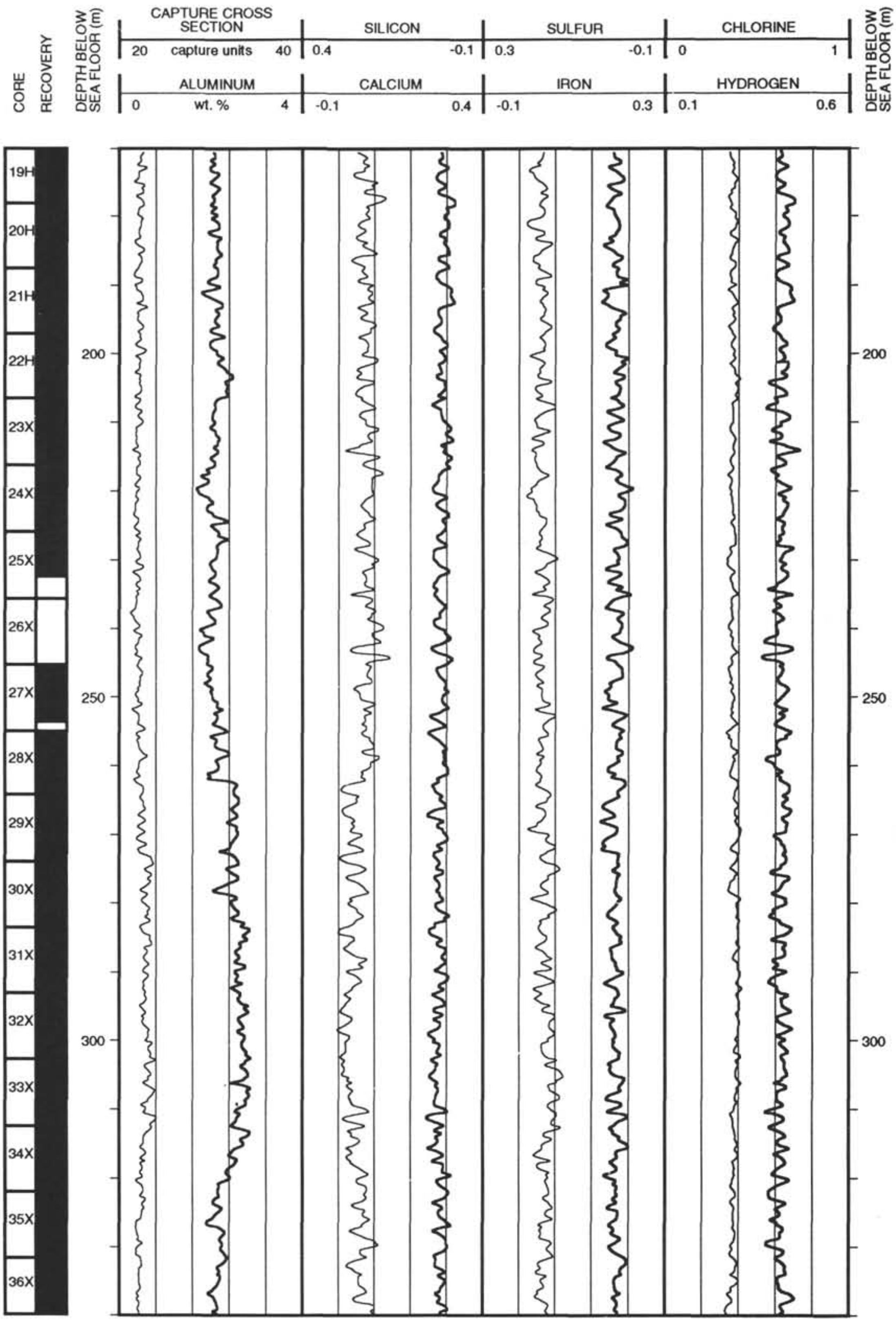

Hole 846B: Geochemical Log Summary (continued)